UNIVERSIDADE FEDERAL DE SÃO CARLOS
CENTRO DE CIÊNCIAS EXATAS E TECNOLOGIA
PROGRAMA DE PÓS-GRADUAÇÃO EM FÍSICA APLICADA

Felipe Soares Covre

Propriedades Ópticas e Magneto-Ópticas de Monocamadas de Dicalcogenetos de Metais de Transição

São Carlos
2022

UNIVERSIDADE FEDERAL DE SÃO CARLOS
CENTRO DE CIÊNCIAS EXATAS E TECNOLOGIA
PROGRAMA DE PÓS-GRADUAÇÃO EM FÍSICA APLICADA

Felipe Soares Covre

Propriedades Ópticas e Magneto-Ópticas de Monocamadas de Dicalcogenetos de Metais de Transição

Tese apresentada ao Programa de Pós-Graduação em Física da Universidade Federal de São Carlos, como como parte dos requisitos para obtenção do título de doutor em física

Orientação: Yara Galvão Gobato

Co-orientação: Christiano José Santiago de Matos

São Carlos

2022

UNIVERSIDADE FEDERAL DE SÃO CARLOS

Centro de Ciências Exatas e de Tecnologia
Programa de Pós-Graduação em Física

Folha de Aprovação

Defesa de Tese de Doutorado do candidato Felipe Soares Covre, realizada em 07/06/2022.

Comissão Julgadora:

Profa. Dra. Yara Galvão Gobato (UFSCar)

Prof. Dr. Christiano José Santiago de Matos (Mackenzie)

Prof. Dr. Ingrid Barcelos (CNPEM)

Prof. Dr. José Pedro Donoso Gonzalez (USP)

Prof. Dr. Marcelo Barbosa de Andrade (IFSC/USP)

Prof. Dr. Helder Vinicius Avanço Galeti (UFSCar)

O Relatório de Defesa assinado pelos membros da Comissão Julgadora encontra-se arquivado junto ao Programa de Pós-Graduação em Física.

Agradecimentos

Gostaria de agradecer a todos que colaboraram para a realização dessa tese, em especial ao Profa. Yara Galvão Gobato pela orientação e toda ajuda ao longo deste doutorado. Agradeço também ao Prof. Christiano José Santiago de Matos pela co-orientação.

Agradeço também a todos os alunos do grupo GOMA que com discussões e conselhos ajudaram muito no trabalho realizado durante esse doutorado, em especial Daniele de Souza e Caique Serati de Brito.

Agradeço a todos os colaboradores dos artigos apresentados nessa tese, especialmente Dra.Vanessa Orsi Gordo, Prof. Dr. Fernando Iikawa, Prof. Dr. Peter Christianen e Dr. Paulo Faria Junior.

Agradeço à minha esposa Julia, que me ajudou em todas as dificuldades encontradas durante o doutorado, permitindo que eu conseguisse superá-las. Sem ela essa tese não teria acontecido.

Por fim, agradeço a CNPq pelo apoio financeiro nesse mestrado.

SUMÁRIO

RESUMO

Materiais bidimensionais (2D) são sistemas de grande interesse tanto do ponto de vista física fundamental como para possíveis aplicações em eletrônica, optoeletrônica e spintrônica. Nesta tese, foram investigadas propriedades óticas de monocamadas de dicalcogenetos de metais de transição (TMD) crescidos por *Chemical Vapor Deposition* (CVD) e esfoliadas. Em particular, realizamos um estudo sistemático das propriedades óticas de monocamadas de dissulfeto de tungstênio (WS_2) de área grande (da ordem de alguns cm), crescidos por de epitaxia de van der Waals em um sistema de CVD. Investigamos as propriedades óticas dessas amostras usando as técnicas de macro-fotoluminescência e micro-fotoluminescência (PL) em baixas temperaturas. Observamos que a emissão ótica destas amostras é bastante instável no tempo e que está instabilidade depende da temperatura e potência do laser. Este efeito foi associado a dopagem fotoinduzida. Esse efeito foi usado para identificar diversos complexos excitônicos. Além disso, observamos picos finos na região de menor energia que são promissores para geração de fótons únicos. De forma geral, os resultados obtidos ajudaram a obter uma maior compreensão sobre os efeitos da dinâmica de fotodopagem por laser nesses sistemas, contribuindo assim para futuras aplicações de dispositivos baseados em TMDs.

Investigamos também efeitos de tensão biaxial em uma monocamadas de disseleneto de molibdênio ($MoSe_2$)/h-BN preparada por esfoliação mecânica e por técnica de transferência seca. A amostra estudada possui uma região com uma bolha da ordem de 15 μm produzindo uma tensão biaxial mecânica de até 1.3% nessa região. Investigamos os efeitos de tensão utilizando diversas técnicas experimentais, como PL, magneto-PL e geração de segundo harmônico (SHG). Os resultados obtidos evidenciaram a presença de uma tensão não-uniforme na amostra, bem como um deslocamento para o vermelho nos picos de PL do éxciton e tríon, quando comparamos com a região sem tensão na amostra. Foi também observado uma variação na energia de ligação do tríon e um aumento do fator-g do tríon e do éxciton, na região da bolha. Os resultados obtidos são coerentes com cálculos de primeiros princípios realizado nesses sistemas. Os resultados obtidos apresentam informações importantes sobre os efeitos de tensão nas propriedades de éxcitons e tríons em monocamada de $MoSe_2$ e são interessantes para o desenvolvimento de dispositivos com tensão mecânica controlada baseados em TMDs.

Palavras-Chave: $MoSe_2$, WS_2, Fotoluminescência, TMDs

ABSTRACT

Bidimensional (2D) materials are systems of great interest both from the fundamental physical point of view and for possible applications in electronics, optoelectronics and spintronics. In this thesis, the optical properties of monolayers of transition metal dicalcogenetes (TMD) grown by *Chemical Vapor Deposition* (CVD) and exfoliated were investigated. In particular, we conducted a systematic study of the optical properties of tungsten disulfide (WS2) of large area (of the order of some cm), grown by van der Waals epitaxy on a CVD system. We investigated the optical properties of these samples using macro-photoluminescence and micro-photoluminescence techniques at low temperatures. We observed that the optical emission of these samples is quite unstable in time and that this optical instability depends on the temperature and power of the laser. This effect was associated with photoinduced doping. In addition, we observed thin peaks in the region of lower energy that are promising candidates for the generation of single photons. In general, the results obtained help to gain a greater understanding of the effects of photo-doping dynamics on these systems, which is important for future applications of TMD-based devices.

We also investigated biaxial stress effects on a monolayer of molybdenum diselenide (MoSe2)/h-BN prepared by mechanical exfoliation and dry transfer technique. The sample studied has a region with a bubble of the order of 15 μm producing a mechanical biaxial tension of up to 1.3% in that region. We investigated the effects of tension using several experimental techniques, such as PL, magneto-PL and second harmonic generation (HGS). The results obtained showed the presence of a non-uniform tension in the sample, as well as a displacement to red in the PL peaks of the exciton and trion, when compared with the region without tension in the sample. A decrease of the trion binding energy and an increase in the g-factor of the trion and exciton in the bubble region were also observed. The results obtained are consistent with calculations of first principles performed in these systems. The results obtained present valuable information on stress effects in the properties of excitons and trions in MoSe2 monolayer and are interesting for the development of devices with controlled mechanical tension based on TMDs.

Keywords: $MoSe_2$, WS_2, Photoluminescence, TMDs

INTRODUÇÃO

1. Materiais 2D

Materiais bidimensionais têm tido um grande foco em pesquisas em anos recentes, do ponto de vista de física fundamental e para aplicações em dispositivos, e esse interesse continua a crescer sendo evidenciado pela quantidade de novos artigos e pesquisas na área. Isso ocorre devido a que, no início do século XXI, conseguiu-se pela primeira vez isolar grafeno a partir do desenvolvimento de novas técnicas de fabricação como a esfoliação mecânica[1]. Essa única camada de carbono pode ser obtida facilmente devido a sua fraca ligação de van der Waals entre camadas de grafite, enquanto a ligação entre os átomos dentro da camada é comparativamente forte. Isso vale também para outros materiais bidimensionais estudados nos últimos anos[2]. Estão representados na figura 1 alguns tipos de materiais com ligação van der Waals.

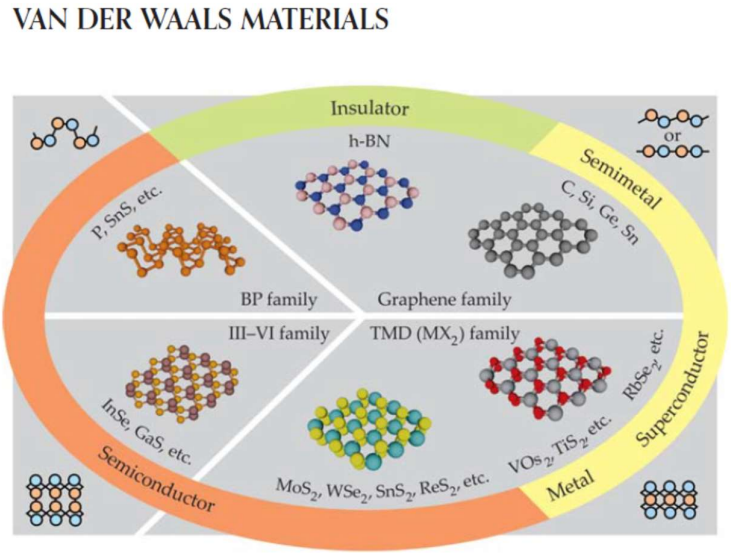

Figura 1 *Tipos de materiais bidimensionais*[3]

O grafeno ganhou destaque por ter várias características interessantes como alta condutividades térmica e elétrica, transparência óptica, além de suas propriedades mecânicas.[4,5] Porém, o grafeno não constitui em um bom material para aplicações optoeletrônicas, levando ao estudo de outros materiais bidimensionais que pudessem cumprir esse papel.[6] Disulfeto de Rênio (ReS_2), Nitreto de Boro Hexagonal (h-BN) e Disseleneto de

Tungstênio (WSe_2) são alguns exemplos desses materiais que atraíram muita atenção nos últimos anos. Os artigos apresentados nessa tese focam em Dissulfeto de Tungstênio (WS_2) e Disseleneto de Molibdênio ($MoSe_2$), que pertencem a classe dos dicalcogenetos de metais de transição (TMDs). Exemplos de TMDs podem ser vistos na figura 1. Esses dicalcogenetos são formados por camadas de um calcogênio e de metais de transição. Cada monocamada possui três camadas, sendo uma de metal entre duas de calcogênio, como pode ser visto no esquema da figura 2.

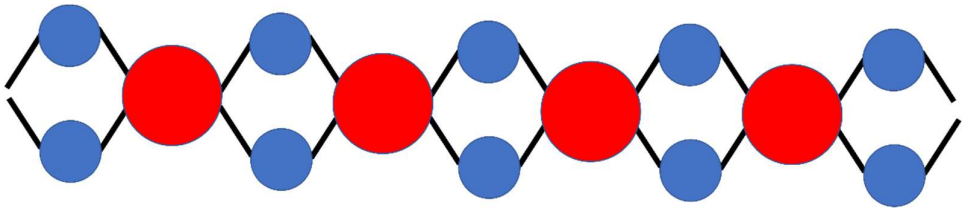

Figura 2 *Representação de uma monocamada de TMD, onde as circunferências vermelhas representam o metal de transição e as azuis são as camadas de calcogênio.*

Uma aplicação interessante para esses materiais é a possibilidade de combinar monocamadas de diferentes materiais criando-se assim dispositivos baseados em heteroestruturas de van der Waals, como pode ser visualizado na figura 3.

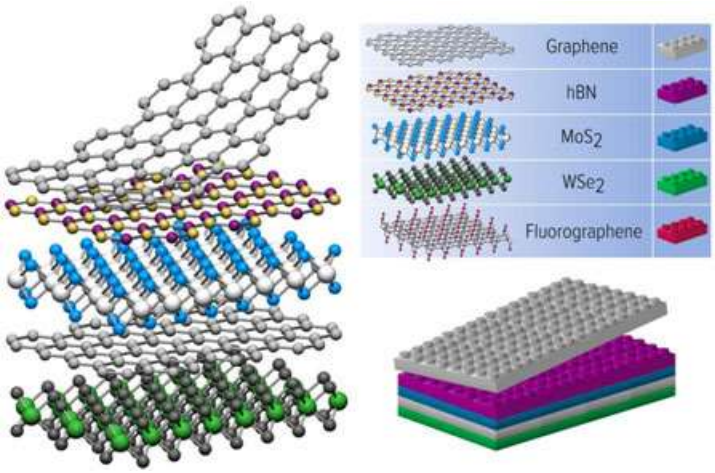

Figura 3 *Heteroestrutura de van der Waals*[7]

Nos próximos tópicos serão abordados de forma resumida alguns conceitos importantes para essa tese, seguidos das sessões onde serão abordados dois artigos sobre TMDs, elaborados durante esse projeto de doutorado e que já foram publicados.

2. Estrutura de Banda

Os TMDs possuem propriedades muito distintas do material em formato de *bulk* quando comparadas às suas características de espessuras diferentes. Uma muito importante é que em um cristal em condição de *bulk* um TMD (por exemplo, o MoS_2) é um semicondutor de *gap* indireto, porém quando observamos esse material em formato de monocamada temos um semicondutor de *gap* direto. Essa mudança pode se tornar muito interessante para propriedades de optoeletrônica como pode ser visto na figura 4.

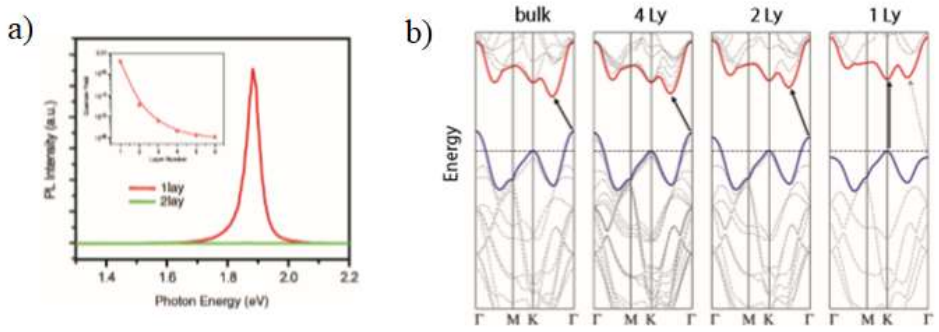

Figura 4 a) *Espectro de Fotoluminescência de MoS_2.*[8] ***b)*** *Estrutura de banda para MoS2.*[9]

3. Determinação do Número de Camadas

Como comentando anteriormente nessa tese, as propriedades de TMDs diferem muito dependendo do número de camadas do material. Portanto, é de extrema importância a determinação exata do número de camadas da amostra a ser estudada. Existem diferentes métodos que podem ser utilizados para fazer essa determinação como pode ser visto na figura 5. Alguns desses diferentes métodos incluem microscopia de força atômica (*Figuras 5. b* e *c*), contraste óptico (*Figura 5. a*) e Raman por exemplo (*Figuras 5. d, e, f* e *g*), dentro outras. Cada uma dessas técnicas observa propriedades distintas para determinar o número de camadas. O Raman, por exemplo, observa as vibrações da rede cristalina, já o contraste óptico acompanha quantidade de luz absorvida pelo material etc.

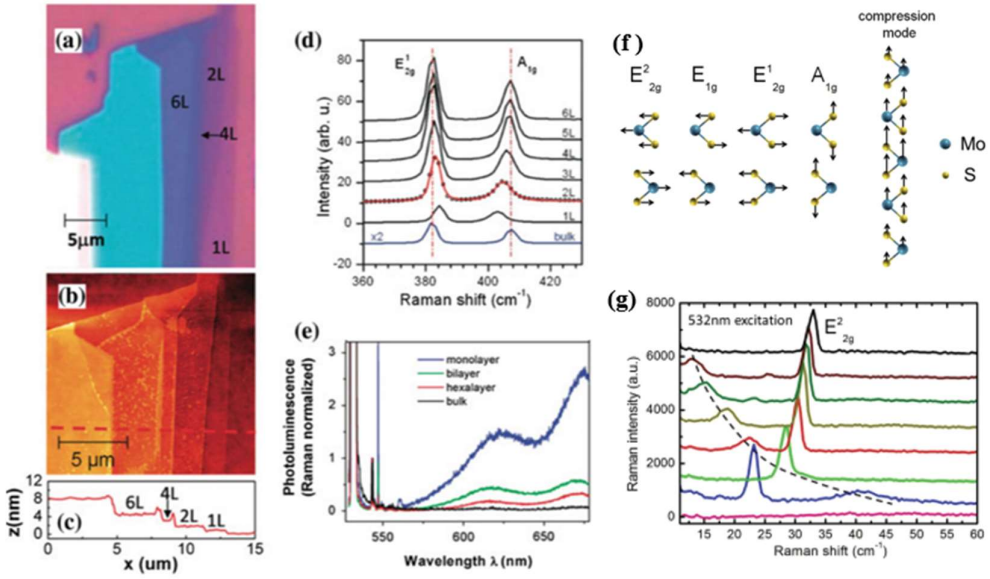

Figura 5 *Representação de diferentes métodos para identificação da espessura do material*[10]

4. Estruturas Excitônicas

Nos trabalhos apresentados foram estudados diversos tipos de estruturas excitônicas, como por exemplo o próprio éxciton que consiste em uma partícula formada por interação colombiana entre um elétron e um buraco, bi éxciton formado pela interação de dois éxcitons e, por exemplo, o tríon que combina um éxciton e um buraco ou um éxciton e um elétron.

O éxciton em materiais TMD possui uma energia de ligação muito robusta quando comparado a semicondutores mais tradicionais, como os da família III-V, possuindo uma energia de ligação aproximadamente de 300meV. Enquanto que uma energia de ligação do tríon também robusta é de aproximadamente 30meV. Vários complexos excitônicos diferentes podem ser observados em monocamadas TMD, como por exemplo o biéxciton, o que os torna interessante para estudos de física de complexos excitônicos. Na figura 6 é possível observar configurações excitônicas possíveis para TMDs do tipo MoX_2 e do tipo WX_2.

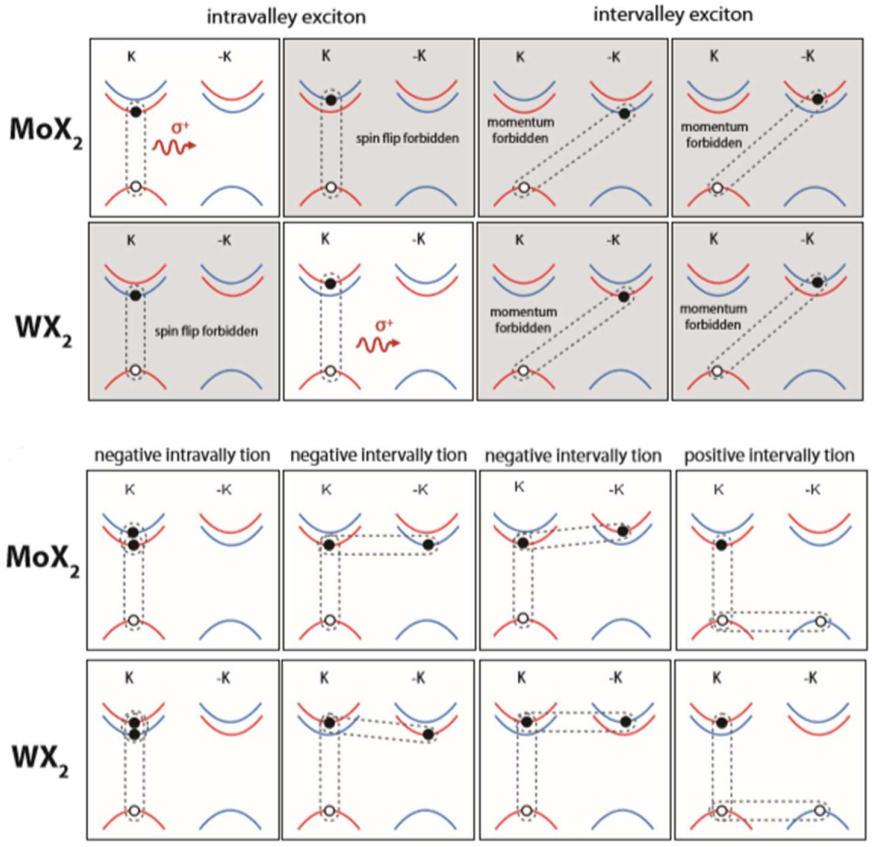

Figura 6 *Representação Esquemática de Complexos Excitônicos em TMDs*[11]

5. Física de Vale

Uma das propriedades mais intrigantes em TMDs é o efeito da degenerescência de vale. Isso ocorre pois os pontos K e K' (também chamados de K e K-) da primeira zona de Brillouin não são equivalentes em *spin*, mas continuam sendo equivalentes em *gap* de energia. Esse efeito pode ser visualizado na figura 7.

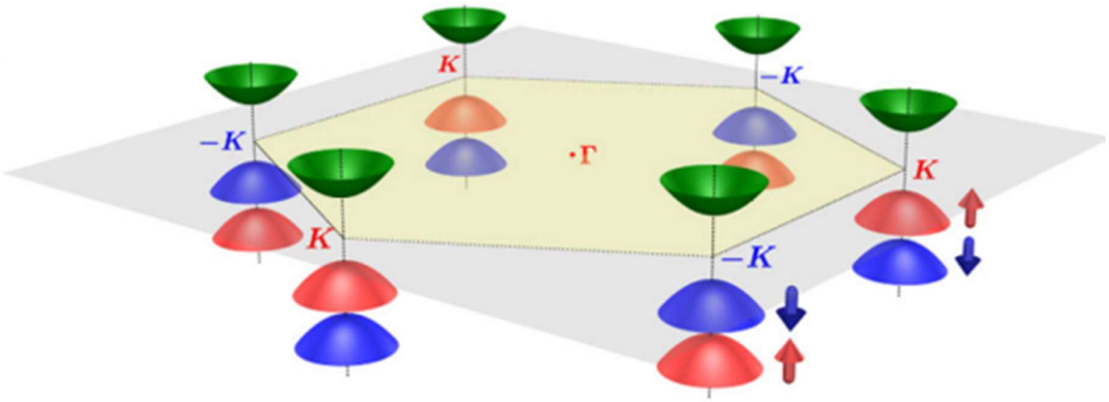

Figura 7 *Representação da Primeira Zona Brillouin*[12]

Esse fenômeno permite então que podemos, por exemplo, acessar os diferentes vales com luz circularmente polarizada, o que acaba gerando possíveis aplicações para uma eletrônica de *spin*.

Essa degenerescência acaba implicando em regras de seleção para transições permitidas e proibidas, em que a transição de menor energia do TMD acaba sendo permitida ou não em *spin*. Quando a transição é permitida o TMD é considerado tipo claro, enquanto que quanto é proibido considera-se o TMD do tipo escuro, como pode ser visto na figura 8.

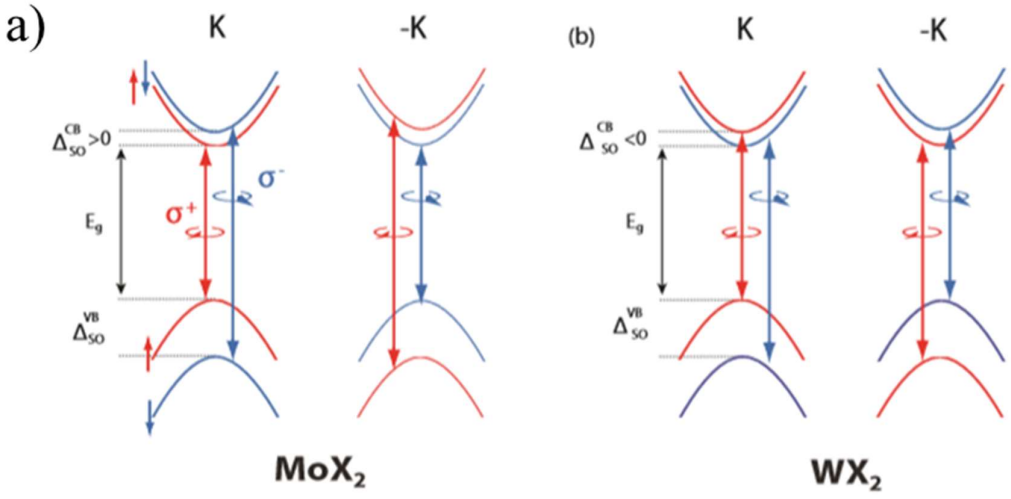

Figura 8 *Transições Permitidas em TMDs*[11]

6. Efeitos de Tensão

Além do número de camadas que comentamos nessa tese, os efeitos de tensão em monocamadas de TMDs também podem modificar substancialmente várias das propriedades do material como o *gap* de energia e propriedades magnéticas. Podemos assim pensar em eletrônica baseada em tensão com esses TMDs, exemplificada na figura 9.

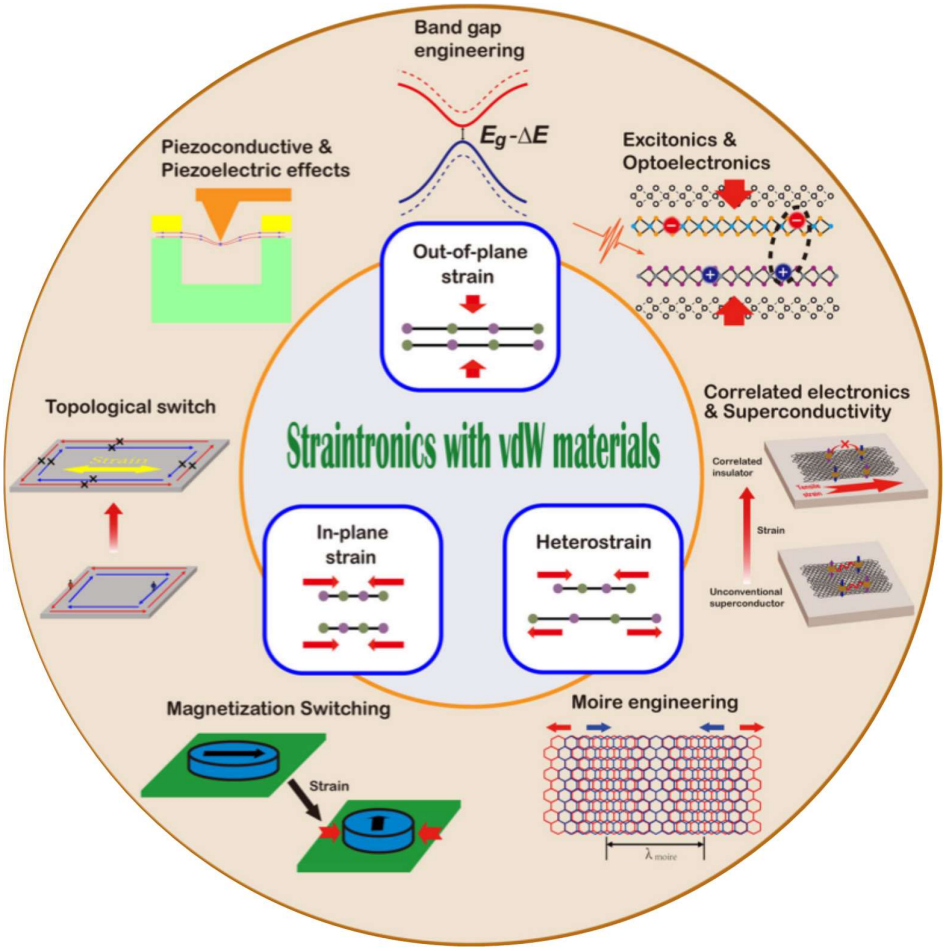

Figura 9 *Eletrônica de Tensão*[13]

Já foram realizados vários estudos sobre efeitos de tensão em TMDs, os quais mostram mudanças substanciais em picos de PL e nos picos Raman, nos permitindo assim estimar a tensão sobre uma amostra baseada nessas medidas, bem como observarmos a importância da tensão para diferentes propriedades. Usualmente, tais artigos são realizados em temperatura ambiente devido a dificuldade de fazer tais medidas em baixa temperatura. Um diferencial do artigo 2 dessa tese foi justamente fazer as medidas em baixa temperatura,

observando os resultados dos efeitos de tensão sob essa condição. Na figura 10 são mostrados efeitos da tensão controlada em uma amostra de MoS_2.

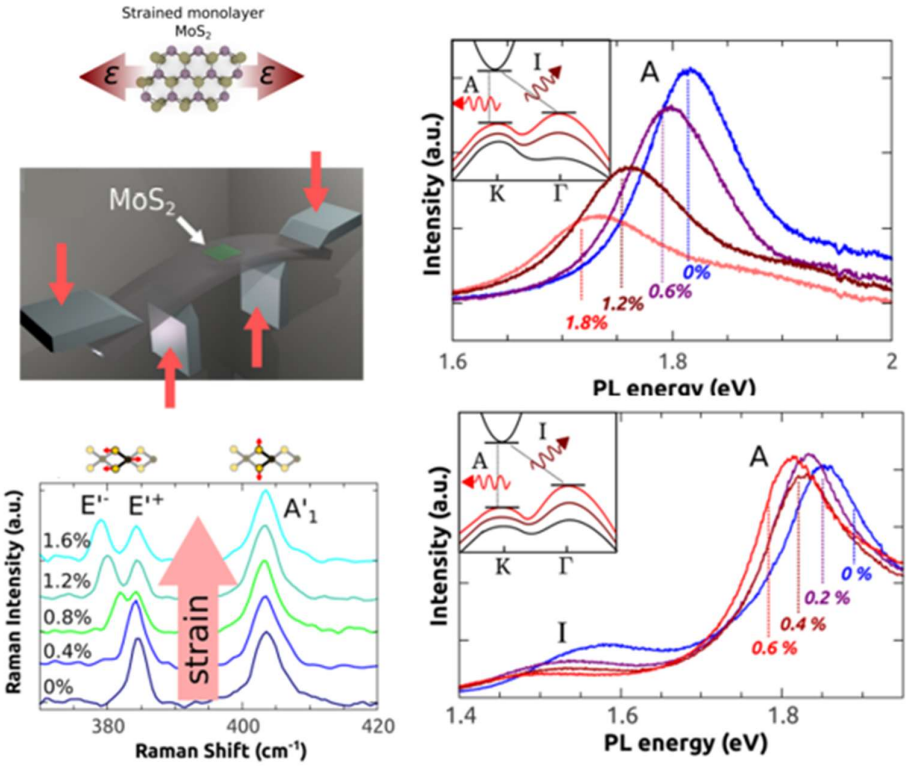

Figura 10 *Efeitos de Tensão em Diferentes Propriedades do* MoS_2[14]

Outra importante propriedade afetada pela tensão nos tipos de materiais estudados nessa tese, é a Geração de Segundo Harmônico (SHG). Como pode ser visto na figura 11, a tensão no material pode afetar substancialmente a sua intensidade, assim fazendo um mapa de SHG podemos observar como a tensão está sendo distribuída no material, bem como se temos uma tensão extensiva ou compressiva atuando no sistema estudado.[15]

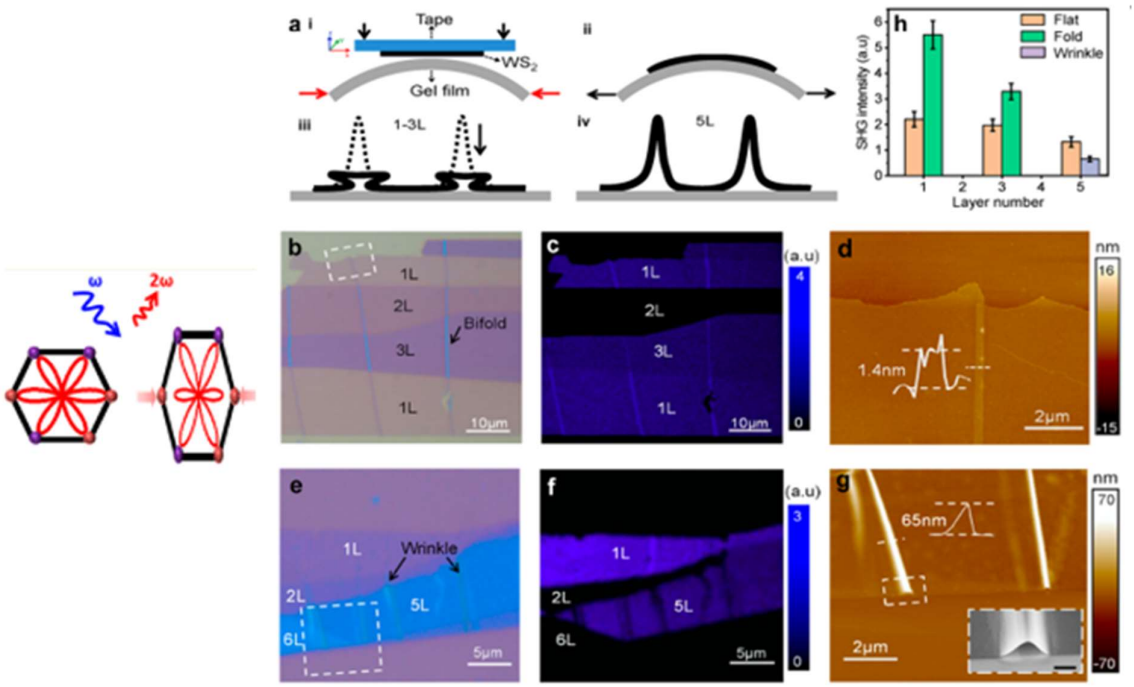

Figura 11 *Efeitos de Tensão sobre o SHG*[15]

7. Campo Magnético Perpendicular

As medidas com campo magnético realizadas nos artigos apresentados nessa tese foram sempre realizadas com campo magnético em uma configuração perpendicular, esquematizado na figura 12.

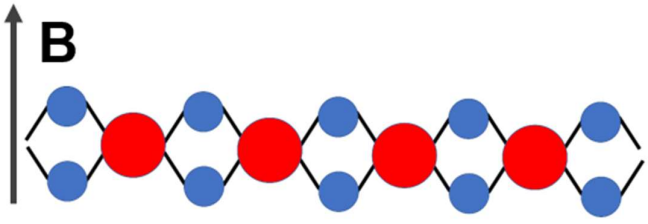

Figura 12 *Campo Magnético Perpendicular em uma Monocamada*

Um importante fenômeno que ocorre nos materiais TMDs é o chamado Efeito *Valley-Splitting*. Esse evento é similar ao que ocorre em semicondutores usuais com o Efeito *Zeeman-Splitting*, porém aqui o que ocorre é a mudança dos níveis de energia em cada um dos

vales K e K', como pode ser visto na figura 13. Essa separação dos níveis é dada pela seguinte equação: $\Delta_z = \mu_b g B$.

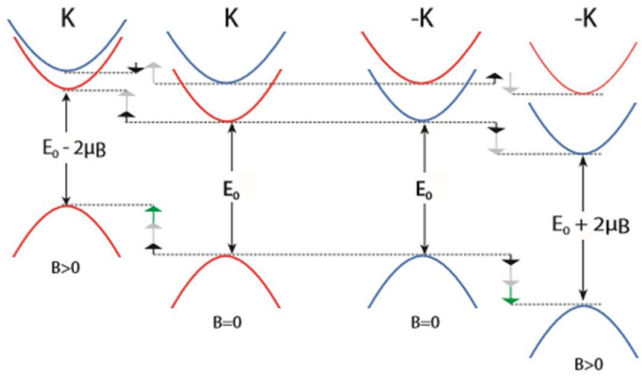

Figura 13 *Separação da Energia de Vales*[11]

Como visto na equação acima o fator-g tem um papel importante nas propriedades dos dicalcogenetos de metais de transição. Ele é objeto constante de estudo, em que valores típicos são conhecidos, porém uma dispersão ocorre devido a algumas propriedades que podem influenciar em seu valor. Na figura 14 são apresentados valores típicos para o fator-g dos TMDs $MoSe_2$, WSe_2 e WS_2.

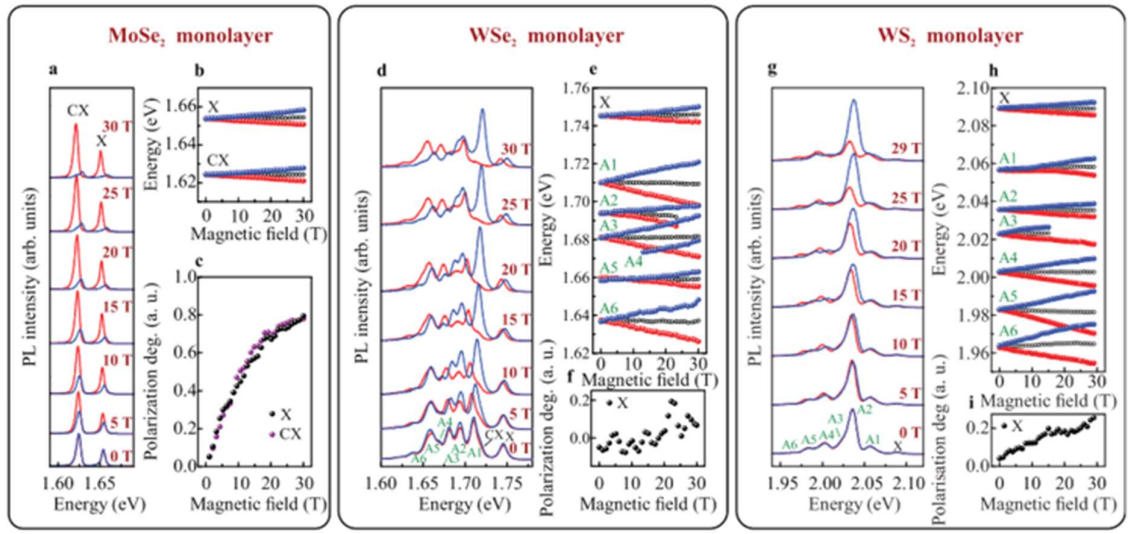

MoSe$_2$ monolayer

Line	*g*-factor
X	−4.2 ± 0.2
CX	−3.7 ± 0.3

WSe$_2$ monolayer

Line	*g*-factor
X	−4.3 ± 0.2
A1	−13.5 ± 0.7
A2	−6.5 ± 0.3
A3	−12.0 ± 0.6

Line	*g*-factor
A4	~ −12
A5	−5.3 ± 0.3
A6	−11.4 ± 0.6

WS$_2$ monolayer

Line	*g*-factor
X	−4.0 ± 0.2
A1	−4.4 ± 0.2
A2	−4.2 ± 0.2
A3	−8.5 ± 0.4

Line	*g*-factor
A4	−8.8 ± 0.4
A5	−13.2 ± 0.7
A6	−13.3 ± 0.7

Figura 14 *Fator-g para as monocamadas de MoSe2, WSe2 e WS2*[16]

Referências

[1] Novoselov, K. S. et al.; Electric field effect in atomically thin carbon films. **Science**, 306(5696),666–669, 2004

[2] Liu, Yuan. et al.; Van der Waals Heterostructures and devices **Nature Reviews Materials**, 1, 16042, 2016.

[3] Ajayan, P. et al.; Two-dimensional van der Waals materials, **Physics Today** 69, 9, 38,2016

[4] Lee, H. C. et al.; Review of the synthesis, transfer, characterization and growth mechanisms of single and multilayer graphene, **RSC Advances**, vol. 7, no. 26, pp. 15644–15693, 2017.

[5] Cao, K. et al.; Elastic straining of free-standing monolayer graphene, **Nature Communications**, vol. 11, no. 1, pp. 1–7, 2020.

[6] Novoselov, K. S. et al.; A roadmap for graphene, **Nature**, vol. 490, no. 7419, pp. 192–200, 2012.

[7] Gein, A. K. et al.; van der Waals Heterostructures, Nature 499, 419-415, 2013.

[8] Mak, K. F. et al.; Atomically Thin MoS2: A New Direct-Gap Semiconductor, **Physical Review Letters**, 105(13):136805–4, 2010.

[9] Splendiani, A. et al; Emerging Photoluminescence in Monolayer MoS 2. **Nano Letters**, 10(4):1271–1275, 2010.

[10] Kolobov, A.V.; Tominaga, J.; **Two-Dimensional Transition-Metal Dichalcogenides**. Suiça: pringer International Publishing, 2016

[11] Ludwig, J., **Optical spectroscopy of novel semiconductors in high Magnetic fields**, 2015, Tese (Doutorado em Física), Florida State University, Tallahasse, Estados Unidos.

[12] Xiao, D. et al.; Coupled Spin and Valley Physics in Monolayers of MoS2 and Other Group-VI Dichalcogenides, **Physical Review Letters**, 108: 196902, 2012.

[13] Miao. F. et al Straintronics with van der Waals materials, npj **Quantun Materials**, 6, 59, 2021.

[14] Conley, H. J. et al; Bandgap Engineering of Strained Monolayer and Bilayer MoS2, **Nano Letters**, 13, 2626–3630, 2013.

[15] Khan, A. R. et al; Emerging Photoluminescence in Monolayer MoS_2. **ACS Nano**, 14(11): 15806-15815, 2020.

[16] Koperski, M. et al; Orbital, spin and valley contributions to Zeeman splitting of excitonic resonances in $MoSe_2$, WSe_2 and WS_2 Monolayers. **2d Materials**, 6, 015001, 2019.

ARTIGOS PUBLICADOS

Os artigos publicados que compõem essa tese de doutorado se encontram a seguir.

Artigo 1: Revealing the nature of low-temperature photoluminescence peaks by laser treatment in van der Waals epitaxially grown WS2 monolayers

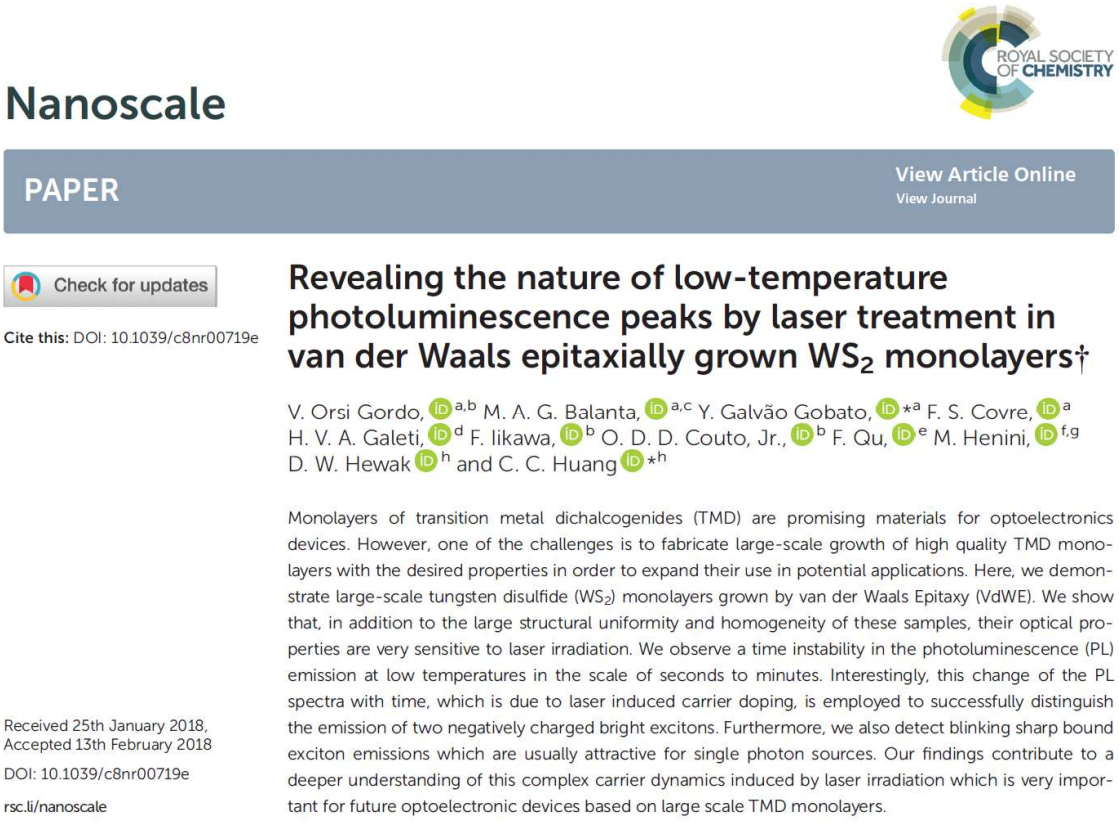

Nanoscale

PAPER

View Article Online
View Journal

Check for updates

Cite this: DOI: 10.1039/c8nr00719e

Revealing the nature of low-temperature photoluminescence peaks by laser treatment in van der Waals epitaxially grown WS_2 monolayers†

V. Orsi Gordo, [a,b] M. A. G. Balanta, [a,c] Y. Galvão Gobato, [*a] F. S. Covre, [a] H. V. A. Galeti, [d] F. Iikawa, [b] O. D. D. Couto, Jr., [b] F. Qu, [e] M. Henini, [f,g] D. W. Hewak [h] and C. C. Huang [*h]

Monolayers of transition metal dichalcogenides (TMD) are promising materials for optoelectronics devices. However, one of the challenges is to fabricate large-scale growth of high quality TMD monolayers with the desired properties in order to expand their use in potential applications. Here, we demonstrate large-scale tungsten disulfide (WS_2) monolayers grown by van der Waals Epitaxy (VdWE). We show that, in addition to the large structural uniformity and homogeneity of these samples, their optical properties are very sensitive to laser irradiation. We observe a time instability in the photoluminescence (PL) emission at low temperatures in the scale of seconds to minutes. Interestingly, this change of the PL spectra with time, which is due to laser induced carrier doping, is employed to successfully distinguish the emission of two negatively charged bright excitons. Furthermore, we also detect blinking sharp bound exciton emissions which are usually attractive for single photon sources. Our findings contribute to a deeper understanding of this complex carrier dynamics induced by laser irradiation which is very important for future optoelectronic devices based on large scale TMD monolayers.

Received 25th January 2018,
Accepted 13th February 2018
DOI: 10.1039/c8nr00719e
rsc.li/nanoscale

Revealing the nature of low-temperature photoluminescence peaks by laser treatment in van der Waals epitaxially grown WS_2 monolayers†

V. Orsi Gordo,[a,b] M. A. G. Balanta,[a,c] Y. Galvão Gobato,*[a] F. S. Covre,[a] H. V. A. Galeti,[d] F. Iikawa,[b] O. D. D. Couto Jr.,[b] F. Qu,[e] M. Henini [f,g] D. W. Hewak[h] and C. C. Huang *[h]

Received 25th January 2018,
Accepted 13th February 2018
DOI: 10.1039/c8nr00719e
rsc.li/nanoscale

[a] Departamento de Física, Universidade Federal de São Carlos, 13565-905, São Carlos, SP, Brazil. E-mail: yara.ufscar@gmail.com
[b] Instituto de Física "Gleb Wataghin", Universidade Estadual de Campinas,13083-859, Campinas, São Paulo, Brazil
[c] Universidade Federal de Uberlândia-FACIP, 38304-402, Ituiutaba, MG, Brazil
[d] Departamento de Engenharia Elétrica, Universidade Federal de São Carlos,13565-905, São Carlos, SP, Brazil
[e] Instituto de Física, Universidade de Brasília, Brasília-DF 70919-970, Brazil
[f] School of Physics and Astronomy, University of Nottingham, Nottingham NG7 2RD,UK
[g] UNESCO-UNISA Africa Chair in Nanosciences/Nanotechnology Laboratories, College of Graduate Studies, University of South Africa (UNISA), Muckleneuk Ridge,P O Box 392, Pretoria, South Africa
[h] Optoelectronics Research Centre, University of Southampton, Southampton,SO17 1BJ, UK. E-mail: cch@orc.soton.ac.uk

†Electronic supplementary information (ESI) available. See DOI: 10.1039/C8NR00719E

Monolayers of transition metal dichalcogenides (TMD) are promising materials for optoelectronics devices. However, one of the challenges is to fabricate large-scale growth of high quality TMD monolayers with the desired properties in order to expand their use in potential applications. Here, we demonstrate large-scale tungsten disulfide (WS_2) monolayers grown by van der Waals Epitaxy (VdWE). We show that, in addition to the large structural uniformity and homogeneity of these samples, their optical properties are very sensitive to laser irradiation. We observe a time instability in the photoluminescence (PL) emission at low temperatures in the scale of seconds to minutes. Interestingly, this change of the PL spectra with time, which is due to laser induced carrier doping, is employed to successfully distinguish the emission of two negatively charged bright excitons. Furthermore, we also detect blinking sharp bound exciton emissions which are usually attractive for single photon sources. Our findings contribute to a deeper understanding of this complex carrier dynamics induced by laser irradiation which is very important for future optoelectronic devices based on large scale TMD monolayers.

I. Introduction

Two-dimensional (2D) transition metal dichalcogenides (TMDs) are very attractive materials which show spin-valley coupled physics and strong excitonic effects which can be exploited in the next generation of optoelectronics devices.[1–8] The large electron and hole effective masses arising from the atomic d-orbitals along with reduced dielectric screening in 2D systems leads to exceptionally strong excitonic interactions and correlations between the charge carriers.[9] Despite the intense investigation of these materials which has occurred over

the last years, the detailed nature of emission bands of 2D semiconductor materials, particularly for WS_2 and WSe_2, is still being unveiled by recent studies.[5,8,10–13] While the photoluminescence (PL) spectra of TMD monolayers (MLs) like MoS_2 or $MoSe_2$ usually show two well-defined peaks associated with neutral excitons and trions, the spectra of WSe_2 and WS_2 MLs at lower temperatures are rather more complex.[11] Strong emission bands which are observed on the lower energy side of the trion emission in WSe_2 and WS_2 have been attributed to radiative recombination of biexcitons.[14–18] However, intra and intervalley negatively charged excitons recombination has been spectrally resolved in the same energy range of the spectrum.[11,13,19,20] The complexity to identify the origin of the peaks in these materials probed by PL spectroscopy is increased by the addition of recombination of localized-exciton complexes bound to defects/crystal imperfections/impurities[8,11,12] and by the possibility of brightening of dark excitons.[10]

The spectra of TMD MLs can also be strongly affected by laser irradiation. Recent studies found that the laser exposure increases considerably the trion/exciton PL intensity ratio accompanied by a small PL redshift in MoS_2, $MoSe_2$ and WS_2 monolayers.[21–23] It was shown that high laser excitation powers can quench the neutral exciton emission in MoS_2 MLs.[22] For WS_2, it has been shown that laser irradiation can also reduce emission from the lowest energy band of the spectrum, the so called localized state (LS) band, which is usually attributed to localized/donor–acceptor recombination states.[11,21] These laser induced effects were interpreted as monolayer photo-doping which can originate from the substrate[22] or due to the reduction of surface adsorbents.[21] Laser induced doping seems to lead samples to cyclic processes since the exposure of the MLs to air at room temperature after laser doping at low temperature seems to recover the original PL spectrum.[22] However, they depend on the type of substrate, sample preparation method, temperature, ambient conditions and aging.[21,22] This may lead to important consequences on the optical and magneto-optical properties of future devices and in studies of TMD MLs under intense laser excitation, such like investigations of exciton polaritons and many body effects.[8,24] However, few detailed studies have been performed in order to understand deeply the optical changes and instabilities, especially in the case of WS_2 and WSe_2 which, as mentioned, usually have higher density of spectral features.

In addition to the relatively broader excitonic bands, the PL spectra of WS_2 and WSe_2 MLs have also revealed sharp emission lines which can exhibit anti-bunching.[25–28] These peaks are usually related to the presence of localized impurity states.[29–31] In WSe_2, while the light emission centers at the edges of the flakes appeared to be robust on a long timescale,

practically all of them showed clear fluctuation effects on a short timescale; jittering of emission lines of the order of the linewidth (on a millisecond timescale) and larger jumps of lines on a timescale of seconds or minutes.[32] For WS_2, the sharp peaks were usually observed in specific areas in grain boundaries in triangle crystals grown by chemical vapour deposition (CVD) and were attributed to bound excitons trapped by surface impurities. These PL peaks can suddenly disappear during the PL measurements.[33] For liquid exfoliated WS_2 nanosheets (lateral dimensions of 20 to 150 nm), individual sharp peaks at different energies showed time fluctuations of positions and intensities which were associated with randomly fluctuating electrostatic environment.[7]

In this manuscript, we investigate the effects of laser irradiation on the stability of the emission lines in WS_2 monolayers grown for the first time by van der Waals epitaxy (VdWE)[34] (details are described in the Methods section and ESI†). In addition to the large structural uniformity and homogeneity of these VdWE-grown WS_2 ML samples, we show that light emission due to carrier recombination reveals time dependent instabilities. By employing macro- and micro (μ) PL measurements, we monitor the variation in time of the intensity and spectral position of the neutral exciton (X), negative trions (T_1 and T_2), bound-exciton (X_B), and localized state (LS) emissions. We show that the PL spectrum as a whole evolves significantly with time, showing the appearance of additional emission bands and disappearance of others. Sharp peaks with linewidths of ≈2 meV were also observed. They appear/disappear in a time scale of a few seconds. We attribute these instability effects to laser induced ML doping which, due to the relatively slow time scale compared to carrier recombination lifetimes leads to unstable emission behaviour. In particular, we use the optical instability effect to attribute the solabelled T_2 emission to a second trion state instead of a biexciton (XX) state. We also show that the time scale of the instability depends on the laser power density and probing spot. For low excitation intensities and large probing spots, the timescale for changes is in the minutes range. For higher laser excitation intensities and smaller spots, the PL time evolution occurs in few seconds and a clear redshift is observed. Under these conditions, at low temperature, the spectra do not recover their original shape when the excitation intensity is reduced to the low excitation regime. Moreover, for small probing areas, nonlinear increase in PL intensity with excitation power is observed. The time instability of WS_2 ML emission and its dependence on the probing spot size are particularly important for future devices of reduced dimensions, such as single photon sources based on TMDs.

II. Results and discussion

Fig. 1(b) shows macro-PL spectra of the WS_2 monolayer measured at 13 K with laser power density of 79.6 W cm^{-2}. Excitation was σ– circularly polarized and detection was performed for σ+ (black curve) and σ– (red curve) PL. We observe four main emission bands in the spectra. The one centered approximately at 640 nm (1.94 eV) is labeled LS and is attributed to emission of donor–acceptor and localized states.[11,14,21] The other 3 emissions are attributed to excitonic states of WS_2.[14,19,21,35] The higher energy emission at 591 nm (2.1 eV) is attributed to the neutral exciton (X) state. The two emissions at 598 nm (2.07 eV) and 605 nm (2.05 eV) labeled T_1 and T_2, respectively, are attributed to two negatively charged exciton states, which will be discussed in more details in the next paragraphs. Fig. 1(b) also shows that the excitonic states of largescale WS_2 are valley polarized, thus demonstrating the momentum conservation for circular polarization selection rules (depicted in Fig. 1(c)) and the efficient initialization of carrier pseudospins in a given valley.[2,15,36,37]

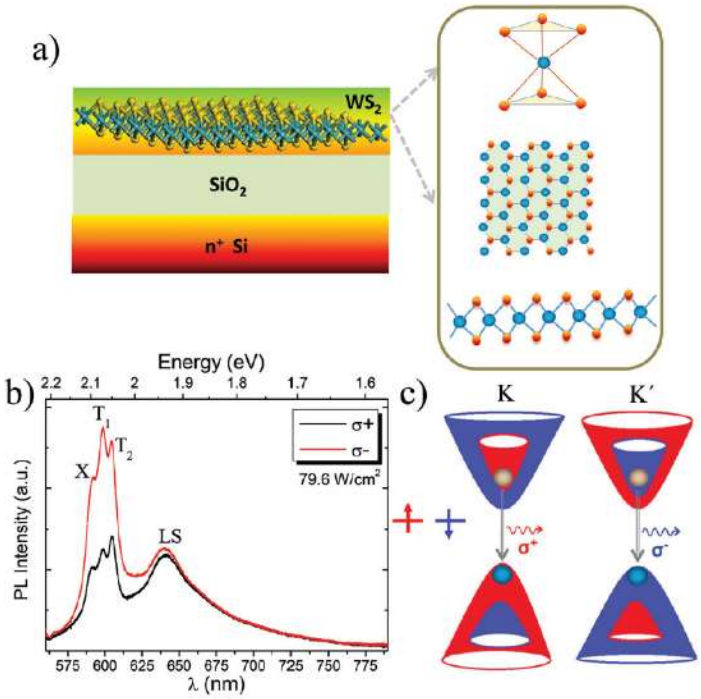

Figure 1 (a) *Illustration of monolayer WS_2 grown on SiO_2/Si substrate. Inset shows the coordination environment of W (blue sphere) in the crystal structure (upper panel), a side-(lower panel) and top-(middle panel) view of the monolayer WS_2 lattice. Sulphur is shown as golden spheres.* ***(b)*** *Circular polarization resolved*

PL measured on a WS_2 at 13 K and σ− excitation. ***(c)*** *Schematic diagram of valley-polarized light emitted by neutral exciton in K-(the left) and K'-(the right) valleys. The red (blue) color represents spin-up (down) states.*

Fig. 2(a) shows macro-PL spectra of our WS_2 ML under different excitation intensities measured at 532 nm. Even at very low powers, all four emissions previously identified in Fig. 1(b) can be observed. As power is increased, T_1 and T_2 become more pronounced and dominate the spectra. This is evidenced in Fig. 2(b), where the peak intensity for each emission is plotted as function of the excitation power (P). The solid lines represent fittings with $I_{PL} = AP^{\beta}$, where A and β are constants. We observe that X and LS emissions increase sublinearly with β values of 0.72 and 0.65, respectively. The tendency for a faster saturation of the LS band is consistent with the limited density of localized and donor–acceptor states in the material. T_1 and T_2 emissions increase faster with power. T_2 increases at a slightly faster rate ($\beta = 1.1$) as compared to T_1 ($\beta = 0.93$). As shown on the inset of Fig. 2(a), T_2 can be observed even at the smallest power we detected the PL signal (7.95 W cm^{-2}), which is more than one order of magnitude lower than the power needed to observe XX emission in WS_2 MLs grown on boron nitride.[38] It is well known that the presence of boron nitride considerably suppresses laser induced doping with carriers injected from the substrate into the TMD ML.[22] As we will discuss in the next paragraphs, our samples show strong laser induced doping effects. Considering also that our samples are not defect-free and electron-doped, we believe that, at such lower powers, XX formation would not be favoured in the experiments reported in Fig. 2(a). In this way, we attribute T_2 to a second negatively charged exciton emission, in agreement with other reports in the literature.[11,13,39]

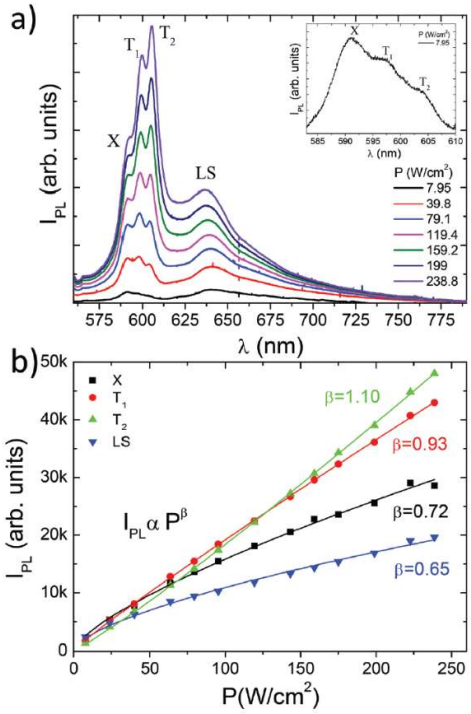

Figure 2 (a) *Macro-PL measured at 12 K for WS2 monolayer as function of excitation power. Inset: Main excitonic emission band measured at 7.95 W cm*$^{-2}$*.* ***(b)*** *PL intensity as a function of excitation power for X, T1, and T2, and LS emission. Solid lines correspond to fits with* $I_{PL} = AP^{\beta}$*, where A and β are constants. The values of β obtained from each fit are displayed for each emission.*

It is already known that different configurations of three particle complexes such as intravalley- (carriers are located within the same valley) and intervalley-(carriers are in different valleys) trions can be formed in WS_2. In the lowest energy bright trion configuration (T_1), the excess electrons occupy the lowest energy sub band in the conduction band.[11] In this case, the excess electron that constitutes the charged exciton might be in the same (singlet) or different (triplet) valley state. An energetic splitting between these two configurations (which is not resolved in our experiments), usually called trion fine structure, is determined by intervalley electron–hole exchange interaction.[19,20,40] In the highest energy trion configuration (T_2), both electrons occupy the upper conduction-band sub band and, therefore, are expected to be brighter at higher excitation intensity conditions. T_2 also comprises an intravalley singlet and an intervalley triplet trions (also not resolved in our experiments). The energy separation between T_1 and T_2 observed in our experiments is 20 meV, which is also in very good agreement with literature reports.[11,13] Note that we also considered the possibility of assigning the rise of T_2 to a dark trion brightening process. However, our assignment of T_2 peak to a

bright trion is supported by the fact that the energy separation between the T_1 and T_2 emissions expected for the dark trion process is $2\Delta_{SO}$[10] which, given the experimental value of 20 meV, would imply in Δ_{SO} values considerably smaller than the predicted ones.[41–43]

Fig. 3(a) presents macro-PL spectra (at a fixed laser power) taken with time intervals of few minutes between each measurement. We observed that, in approximately 40 minutes, X and LS emissions decrease by considerable amounts, with LS emission decreasing more than X in absolute values. T_1 also decreases at a slower rate while T_2 increases with time.

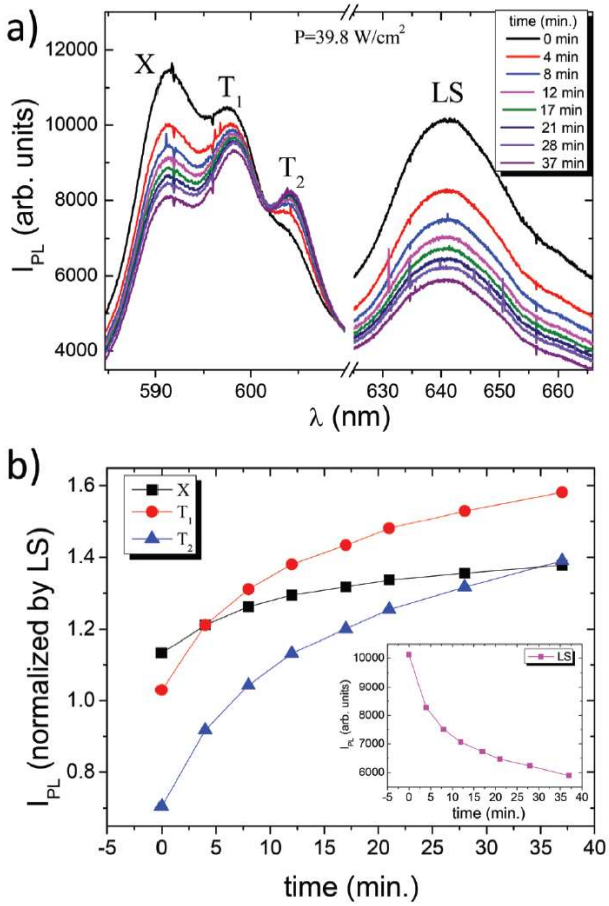

Figure 3 (a) *PL spectra at 12 K and fixed excitation power for different times after the first measured spectrum (black curve).* ***(b)*** *PL intensity of X, T_1, and T_2 emissions normalized by the LS emission intensity (shown on the inset) for different times after first measured spectrum.*

The quenching of LS emission under strong laser pumping and the appearance of an emission band at the lower energy side of T_1 has already been reported in literature.[21] The quenching of LS has been interpreted as laser induced removal of surface adsorbents (associated with LS emission).[21,44] Surface desorption may leave carriers in the system.

However, laser exposure has also been demonstrated to lead to another efficient way to dope the system via carrier injection from the substrate.[22] We, therefore, attribute the increase of T_2 emission with time to an enhanced probability that electrons occupy the upper conduction sub band states due to high electron doping induced by laser irradiation.[22,45] This enhancement of T_2 emission (in comparison to X and T_1) with photo doping is consistent with the results obtained by electron injection in gated devices.[11] In this way, we use laser irradiation as a contactless approach to induce changes in the spectrum of WS_2 and identify T_2 as a trionic state. This is further confirmed in Fig. 3(b), where the intensities of X, T_1, and T_2 as function of time are normalized by the LS emission since this emission is associated with surface desorption and, therefore, also responsible for doping the system. We observe that, relative to LS emission, T_1 and T_2 emissions increase at very similar rates when electrons are added to the system. This behavior further corroborates our attribution of T_2 to a trion state rather than a XX one. As also seen in Fig. 3(b), X emission is more independent of the changes in LS. The absolute decrease in X intensity is attributed to the formation of charged complexes as the system is further doped with increase of time.

In order to obtain more information about the doping dynamics and emission stability in our sample in a microscopic level, we performed μ-PL measurements under different excitation power conditions. Fig. 4 presents a μ-PL experiment performed at 10 K with a laser spot diameter of approximately 5 μm at 532 nm. Fig. 4(a) presents a sequence of measurements where laser power is increased (blue curves) and then lowered (red curves). The first spectrum (at 50.9 W cm^{-2}) shows a pronounced LS band and the excitonic features of X and T_1 emissions. As power is raised T_2 emission becomes more pronounced and the excitonic emissions dominate the spectrum in comparison to LS emission (1528 W cm^{-2}). As power is lowered, however, the spectra do not resume back to their initial characteristics. When we compare the spectra measured at 50.9 W cm^{-2}, the X emission is similar in the blue and red curves, but LS emission is weaker and T_2 maintains its dominant behaviour in the red spectrum. This irreversible behaviour of LS band is consistent with the already mentioned surface desorption induced by laser power.[21] The desorption seems to leave electrons in the system which contribute to the preservation of the T_2 emission even at very low laser powers. Moreover, the fact that the X emission changes very slightly while T_2 changes drastically when power is lowered also corroborates our attribution of T_2 to a trion state. If T_2 was due to a biexciton recombination, which depends strongly on the exciton density, T_2 should more or less follow the X emission behavior.

When the power density is high, however, other emissions might also contribute to the intensity of T_2 peak. This is shown in Fig. 4(b), where the logarithm of the peak intensity of this emission is plotted as a function of the logarithm of the excitation power. Blue dots represent power increase and red dots represent power decrease. It is observed that the behaviour is definitely non-linear and it is not possible to fit the data (in the same way we performed in macro-PL experiments) with a dependence such like $I_{PL} = AP^{\beta}$ with a single value for β. At very high carrier densities, other excitonic peaks like bound XX[12,14,15] and/or charged XX[46] (which are observed/expected to be observed in the same energy range) may also be contributing to the overall T_2 intensity.

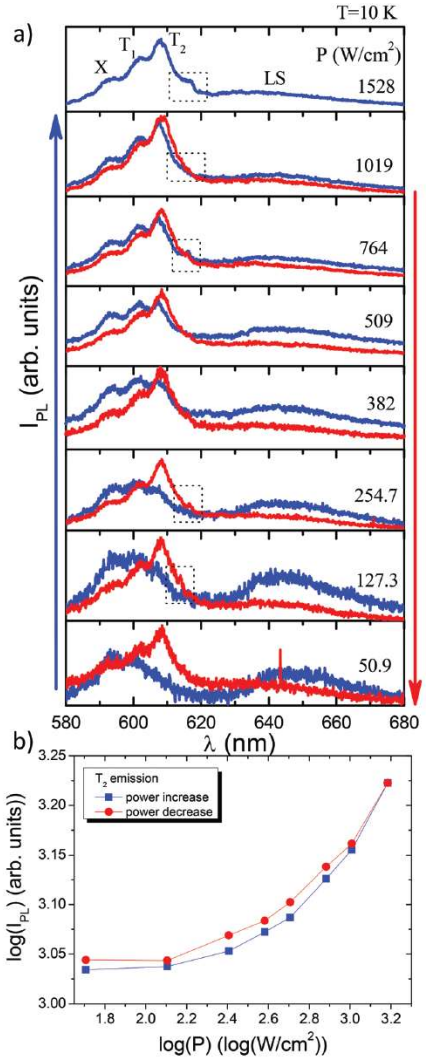

Figure 4 (a) *From bottom to top (blue curves): PL spectra of WS_2 monolayer as excitation power is increased from 50.9 to 1528 W cm^{-2}. From top to bottom (red curves): PL spectra as excitation power is decreased back to 50.9 W cm^{-2}. Dashed squares indicate small changes in the spectra which do not behave in a*

consistent way as power is increased or decreased. ***(b)*** *Integrated PL intensity versus excitation power extracted from (a).*

Another feature observed in the spectra shown in Fig. 4(a) (highlighted by dashed square boxes) is the random appearance of extra emission lines in the lower energy side of T_2. For example, the features highlighted at 1528 W cm^{-2} laser power have not been detected in the previous measurement at 1019 W cm^{-2} (blue spectrum) and are hardly seen again in the sequence at 1019 W cm^{-2} (red spectrum). Other examples can be seen at 254.7 and 127.3 W cm^{-2} spectra (red curves), where the highlighted features appear in the lowering of the power but were not there when power was raised. These unstable peaks appear in an energy region which is usually expected to present recombination of impurity bound exciton states.[11,14] The high carrier density induced in μ-PL excitation seems to be more efficient in activating this kind of recombination, which is a process possibly linked to the surface desorption already discussed.

Fig. 5 presents time stability of the μ-PL emission of our sample when the laser spot is further reduced to 2 μm. As we observe in Fig. 5(a), when the probing spot size is reduced it is easier to identify the contribution of T_2 and bound states (labeled X_B). Fig. 5(b) shows how the μ-PL spectrum changes with time in an interval of 20 minutes under 318 W cm^{-2} excitation at 488 nm. A few minutes after the first spectrum is acquired, we observe that X and LS emissions almost vanish in intensity. T_1 also decreases initially but seems to keep its intensity as time passes. T_2, on the other hand, gains intensity with time. This is consistent with macro-PL results shown in Fig. 3 and illustrates once more the role of carrier doping induced by laser excitation on the optical emission of neutral and charged excitons. It is interesting to note the behaviour of X_B emission in Fig. 5(b). The sharp lines which characterize this emission (with linewidths which can reach 2 meV) are not stable, with variations in intensity and spectral position. This is an indication that the carrier trap/release process by impurity states happens in a time scale of minutes which is the same scale that T_2 gains intensity with time. The same behaviour is observed when the measurement is performed at different positions on the sample surface. This is presented in Fig. 5(c) and (d). The main difference here is that, due to the higher excitation power (637 W cm^{-2}), X and LS emissions seem to be almost immediately quenched due to the accelerated doping process.

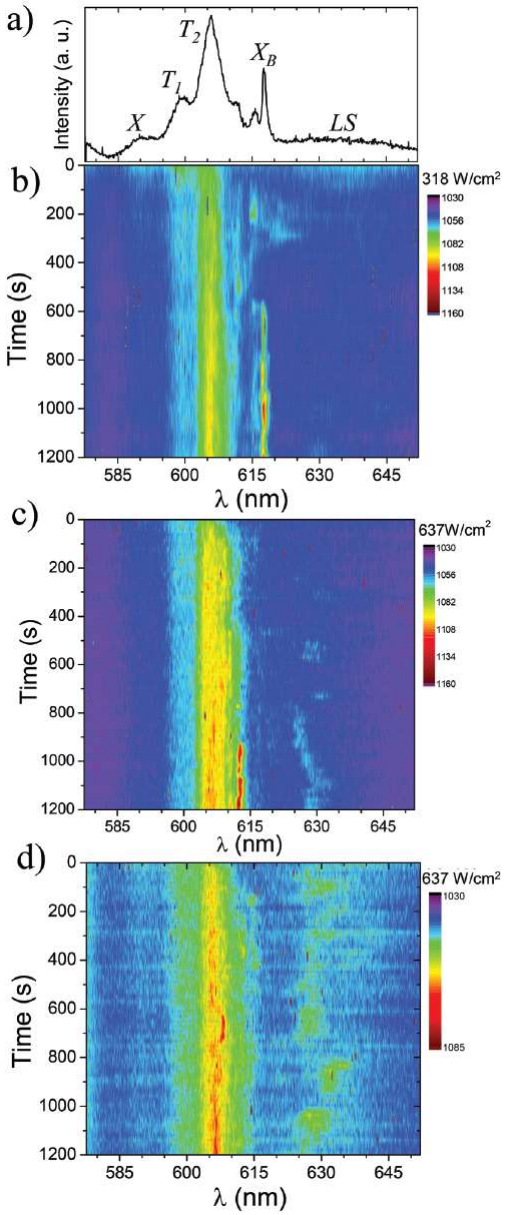

Figure 5 (a) *μ-PL spectra shown in (b) integrated in time.* ***(b)***, ***(c)***, *and* ***(d)*** *Time variation of μ-PL spectra of WS_2 monolayer in the lower excitation power regime for 3 different positions on the sample surface.*

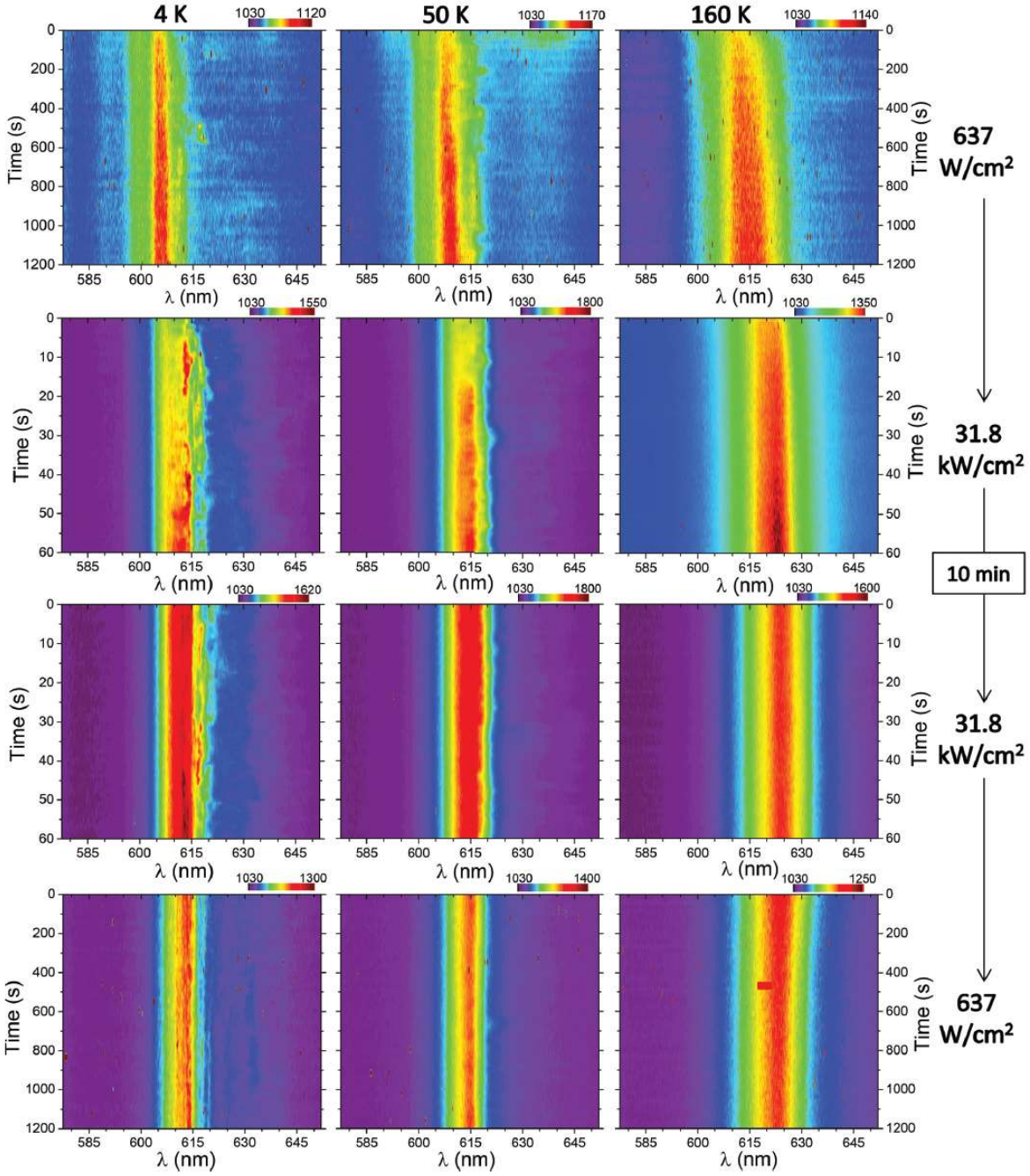

Figure 6 *Color code map showing the variation of μ-PL of WS_2 monolayer in time. First row: Excitation power set at 637 W cm^{-2}. Second row: Power is increased to 31.8 kW cm^{-2}. Third row: Waited for 10 minutes under 31.8 kW cm^{-2} and repeated previous measurement. Fourth row: Power is decreased back to 637 W cm^{-2}. The same procedure is repeated for different temperatures [4 K (left column), 50 K (middle column), and 160 K (right column)].*

Fig. 6 shows how the emission of our WS_2 monolayer changes in time when it is submitted to extreme laser powers (laser spot of 2 μm at 488 nm). Each column of viewgraphs represents measurements at different temperatures (4, 50, and 160 K). Horizontally, power is changed. In this way, for each temperature, μ-PL evolution in time is tracked in a sequence of four measurements. First, immediately after the sample is subjected to a laser excitation of 637 W cm^{-2}, the PL emission is tracked for 20 minutes. Then the power is increased to 31.8 kW cm^{-2} and the measurement is performed once more (for 60 seconds). Subsequently, the laser incidence is maintained on the sample and, after 10 minutes, the last experiment is repeated. Finally, the power is lowered again to 637 W cm^{-2} and the PL is measured once more during 20 minutes. At 4 K and 637 W cm^{-2} (first measurement), the behaviour is exactly the same as illustrated in Fig. 5(c) and (d). When the power is increased to 31.8 kW cm^{-2}, a strong redshift of the emission band is observed. Nevertheless, the emission is still unstable and seems to increase in intensity as time passes. This is an indication that electron doping is still taking place in the system. After 10 minutes of exposure under strong pumping conditions, the emission is slightly more redshifted and has gained intensity in comparison to the previous measurement. Instability still takes place, as we can observe the appearance/disappearance of sharp lines with time in the lower energy side of T_2 band. As power is reduced back to 637 W cm^{-2} (lower viewgraph in the first column), the emission does not blueshift back and the intensity is higher than in the first measurement at the same power. Fig. 7(a) summarizes these experiments by showing the time integrated μ-PL for each view graph of the first column of Fig. 6. By reducing the power after strong pumping conditions, we observe that the neutral exciton emission is quenched (blue curve), while the spectrum is dominated by T_2 and X_B emissions which are strongly favoured after laser doping. The process is, therefore, irreversible and the spectrum maintains its redshift with respect to the initial measurement.

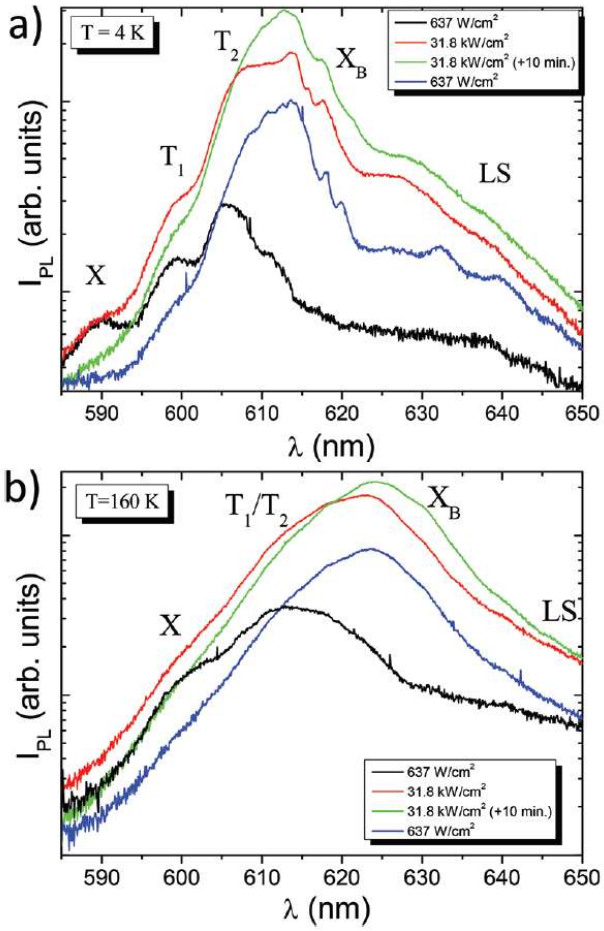

Figure 7 (a) *Time integrated μ-PL spectra for the four viewgraphs shown in the first column of Fig. 6 (4 K).* ***(b)*** *Time integrated μ-PL spectra for the four viewgraphs shown in the last column of Fig. 6 (160 K).*

Fig. 6 also shows how the emission instability varies with temperature. At 50 K and low power, μ-PL spectrum is slightly broader, but it is still possible to see the enhancement of T_2 emission with time and the appearance/disappearance of sharp peaks in the X_B emission region. As power is increased, the PL spectrum gains intensity with exposure time. As power is lowered back, the redshift is also not reversed and the intensity is higher than at the beginning of the experiment, in a similar way to what happens at 4 K. A different behaviour is observed at 160 K. At this temperature, under low power, the PL spectra exhibit broad emission and the whole spectrum moves to the lower energy as time passes. Besides, the X_B related sharp peaks are no more observed. As power increases the redshift is enhanced. As power is lowered again, the spectrum is dominated by a broad emission which superimposes trions (PL measurements as function of temperature, not shown, demonstrate that at this

temperature T_1 and T_2 emissions tend to merge and have comparable intensities) and X_B emission bands. This is shown in Fig. 7(b) (blue spectrum). However, the lower viewgraph of the third column of Fig. 6 indicates that, when power is lowered back to its initial value at 160 K, a slight blueshift of the emission starts to happen in a very slow time scale. This indicates that elevated temperatures are possibly an important ingredient to revert laser induced doping in these TMD monolayers. However, the time scale seems to be slow enough even at room temperature.[23] The overall behaviour of our sample clearly shows that doping/undoping of the WS_2 monolayer is a very slow process which depends on time and pumping laser power. Moreover, we show that the effect is present even at relatively elevated temperatures. These are very important issues which can affect the performance of future optoelectronic devices based on this type of TMD.[6]

III. Conclusions

We have investigated the nature of optical emission and laser irradiation effects on the optical properties of large-scale van der Waals epitaxially grown WS_2 monolayers. We showed that laser irradiation results in dramatic changes in the relative intensity of the individual exciton emission lines. As power or laser exposure time are increased, we show that monolayer doping builds up on a time scale of minutes and can be detected by the pronounced increase in the emission intensities of the two trion emissions T_1 and T_2. The enhancement of trionic emissions, particularly T_2, is demonstrated to be due to carrier injection from substrate and desorption of surface molecules which contribute to the doping process. Reduction of the probing area shows that local carrier recombination dynamics under continuous doping conditions is complex. In particular, bound electron states which present sharp emission lines show considerable intensity instability with time. Under strong laser pumping conditions, the spectra of exposed areas are irreversibly changed, presenting large redshifts due to the dominance of the spectra by trions, bound exciton states, and possibly XX complexes. Temperature increase may contribute to reverting the process, but our experiments indicate that the time scales are still long. Our results can contribute to a better understanding of the optical properties and photo-induced doping process mechanism in laser-scale VdWE WS_2 monolayers, which is of great interest for future nanodevices employing this material system.

IV. Experimental methods

We investigated large-scale (10 mm by 10 mm) WS_2 MLs grown on 300 nm thick thermal oxide (SiO_2) on silicon substrates by van der Waals epitaxy (VdWE) process. VdWE can provide the vapour phase epitaxy of these layered TMDs on the substrates even with mismatched lattice constants.[34] Here, for the first time VdWE technique has been successfully developed to fabricate large-scale ML WS_2 on quartz and SiO_2/Si wafers. Different from typical CVD growth which has been demonstrated to provide large-scale ML films formed by the growth and merging of individual TMD flakes,[47,48] VdWE technique allows very fast growth (typically 5 minutes) of continuous and homogeneous WS_2 ML films (typical sizes are 25 mm by 25 mm with in-house built system at the University of Southampton). VdWE-grown ML characteristics can be found in the ESI section.† Figure S1† shows the spatial homogeneity of a ML of WS_2 grown on 300 nm SiO_2/Si and quartz substrates. The spatial and structural homogeneity of our WS_2 ML films are demonstrated by using Raman (see Figure S2†) and PL (see Figure S3†) spectroscopy measurements taken at room temperature.

In the preparation of our VdWE-grown WS_2 MLs samples, WCl_6 (99.9% pure from Sigma Aldrich) was used as the precursor, kept in a bubbler at room temperature and delivered to VdWE quartz tube reactor (with 50 mm diameter and 1000 mm length) to react with H_2S gas (99.9% pure from BOC) to form WS_2 epitaxially on SiO_2/Si substrates at temperatures in the range of 700–1000 °C. WCl_6 vapors were delivered with argon gas (99.999% pure from BOC) through a mass flow controller (MFC) and the H_2S gas was delivered through another MFC. The flow rates of argon and H_2S gases were in the ranges of 50–300 mL min^{-1}. These van der Waals epitaxially grown WS_2 MLs on SiO_2/Si substrates are illustrated in Fig. 1(a). Hall measurements show that samples are n-type.

Macro-PL measurements were performed using a closedcycle refrigerator cryostat. μ-PL measurements were carried out in vacuum with He cryostat equipped with three-axis stepper motors to control the sample position. The samples were excited using 488 and 532 nm solid state laser sources. The laser spot diameter on the sample for Macro-PL measurements is approximately 400 μm. For μ-PL spot sizes of 5 and 2 μm were employed. In all experiments, detection was performed with 0.5 m spectrometers coupled with Si CCD detectors.

Conflicts of interest

There are no conflicts to declare.

Acknowledgements

The authors acknowledge V. I. Falko for the discussions and A. G. Rodrigues for Raman measurements. The authors also acknowledge the financial supports from the Brazilian agencies Fundação de Amparo a Pesquisa do Estado de São Paulo (FAPESP grants 2012/11382-9, 2016/10668-7, 2016/16365-6, and 2014/50513-7) and Conselho Nacional de Desenvolvimento Científico e Tecnológico (CNPq) (grant 305769/2015-4). and the UK Engineering and Physical Sciences Research Council. This work was funded in part through the Future Photonics Manufacturing Hub at the University of Southampton (EPSRC EP/N00762X/1). The data that support the findings of this study are available from the corresponding authors upon reasonable request.

References

1 Q. H. Wang, K. K. Zadeh, A. Kis, J. N. Coleman and M. S. Strano, Nat. Nanotechnol., 2012, 7, 699.

2 X. Xu, W. Zao, D. Xiao and T. F. Heinz, Nat. Phys., 2014, 10, 343.

3 H. Zeng and X. Cui, Chem. Soc. Rev., 2015, 44, 2629.

4 Y. Ye, Z. J. Wong, X. Lu, X. Ni, H. Zhu, X. Chen, Y. Wang and X. Zhang, Nat. Photonics, 2015, 9, 733.

5 A. V. Kolobov and J. Tominaga, Two-Dimensional Transition-Metal Dichalcogenides, Springer, 2016.

6 K. F. Mak and J. Shan, Nat. Photonics, 2016, 10, 216.

7 L. Klopotowski, C. Backes, A. A. Mitioglu, V. Vega-Mayoral, D. Hanlon, J. N. Coleman, V. Y. Ivanov, D. K. Maude and P. Plochocka, Nanotechnology, 2016, 27, 424701.

8 M. Koperski, M. R. Molas, A. Arora, K. Nogajewski, A. O. Slobodeniuk, C. Faugeras and M. Potemski, Nanophotonics, 2017, 6, 1289.

9 F. Wu, F. Qu and A. H. MacDonald, Phys. Rev. B: Condens. Matter Mater. Phys., 2015, 91, 075310.

10 M. Danovich, v. Zolyomi and V. I. Falko, Sci. Rep., 2017, 7, 45998.

11 M. R. Molas, K. Nogajewski, A. O. Slobodeniuk, J. Binder, M. Bartos and M. Potemski, Nanoscale, 2017, 9, 13128.

12 E. Mostaani, M. Szyniszewski, C. H. Price, R. Maezono, M. Danovich, R. J. Hunt, N. D. Drummond and V. I. Falko, Phys. Rev. B, 2017, 96, 075431.

13 J. Jadczak, J. K. Girzycka, P. Kapuscinski, Y. S. Huang, A. Wojs and L. Bryja, Nanotechnology, 2017, 28, 395702.

14 G. Plechinger, P. Nagler, J. Kraus, N. Paradiso, C. Strunk, C. Schueller and T. Korn, Phys. Status Solidi RRL, 2015, 8, 457.

15 Y. You, X. X. Zhang, T. C. Berkelbach, M. S. Hyberstsen, D. R. Reichman and T. F. Heinz, Nat. Phys., 2015, 11, 477.

16 J. Shang, X. Shen, C. Cong, N. Peimyoo, B. Cao, M. Eginligil and T. Yu, ACS Nano, 2015, 9, 647.

17 Z. He, W. Xu, Y. Zhou, X. Wang, Y. Sheng, Y. Rong, S. Guo, J. Zhang, J. M. Smith and J. H. Warner, ACS Nano, 2016, 10, 2176.

18 I. Paradisanos, S. Germanis, N. T. Pelekanos, C. Fotakis, E. Kymakis, G. Kioseoglou and E. Stratakis, Appl. Phys. Lett., 2017, 110, 193102.

19 G. Plechinger, P. Nagler, A. Arora, R. Schmidt, A. Chernikov, A. G. del Aguila, P. C. M. Christianen, R. Bratschitsch, C. Schuller and T. Korn, Nat. Commun., 2016, 7, 12715.

20 A. Singh, K. Tran, M. Kolarczik, J. Seifert, Y. Wang, K. Hao, D. Pleskot, N. M. Gabor, S. Helmrich, N. Owschimikov, U. Woggon and X. Li, Phys. Rev. Lett., 2016, 117, 257402.

21 Z. He, X. Wang, W. Xu, Y. Zhou, Y. Sheng, Y. Rong, J. M. Smith and J. H. Warner, ACS Nano, 2016, 10, 5847.

22 F. Cadiz, C. Robert, G. Wang, W. Kong, X. Fan, M. Blei, D. Lagarde, M. Gay, M. Manca, T. Taniguchi, K. Watanabe, T. Amand, X. Marie, P. Renucci, S. Tongay and B. Urbaszek, 2D Mater., 2016, 3, 045008.

23 Y. Lee, S. J. Yun, M. S. Kim, G. H. Han, A. K. Sood and J. Kim, Nanoscale, 2017, 9, 2272.

24 S. Dufferwiel, S. Schwarz, F. Withers, A. A. P. Trichet, F. Li, M. Sich, O. D. Pozo-Zamudio, C. Clark, A. Nalitov, D. D. Solnyshkov, G. Malpeuch, K. S. Novoselov, J. M. Smith, M. S. Skolnick, D. N. Krizhanovskii and A. I. Tartakovskii, Nat. Commun., 2015, 6, 8579.

25 Y. M. He, G. Clark, J. R. Schaibley, Y. He, M. C. Chen, Y. J. Wei, X. D. Ding, Q. Zhang, W. Yao, X. Xu, C. Y. Lu and J. W. Pan, Nat. Nanotechnol., 2015, 10, 497.

26 A. Srivastava, M. Sidler, A. V. Allain, D. S. Lembke, A. Kis and A. Imamoglu, Nanotechnology, 2015, 10, 491.

27 M. Koperski, K. Nogajewski, A. Arora, V. Cherkez, P. Mallet, J.-Y. Veuillen, J. Marcus, P. Kossacki and M. Potemski, Nat. Nanotechnol., 2015, 10, 503.

28 C. Palacios-Berraquero, D. M. Kara, A. R. P. Montblanch, M. Barbone, P. Latawiec, D. Yoon, A. K. Ott, M. Loncar, A. C. Ferrari and M. Atature, Nat. Commun., 2017, 8, 15093.

29 C. Chakraborty, L. Kinnischtzke, K. M. Goodfellow, R. Beams and A. N. Vamivakas, Nat. Nanotechnol., 2015, 10, 507.

30 G. Clark, J. R. Schaibley, J. Ross, T. Taniguchi, K. Watanabe, J. R. Hendrickson, S. Mou, W. Yao and X. Xu, RSC Adv., 2016, 6, 27677.

31 Y. He, O. Iff, N. Lundt, V. Baumann, M. Davanco, K. Srinivasan and S. H. C. Schneider, Nat. Commun., 2016, 7, 13409.

32 S. Schwarz, A. Kozikov, F. Withers, J. K. Maguire, A. P. Foster, S. Dufferwiel, L. Hague, M. N. Makhonin, L. R. Wilson and A. K. Geim, 2D Mater., 2016, 3, 025038.

33 T. Kato and T. Kaneko, ACS Nano, 2014, 8, 12777.

34 A. Koma, J. Cryst. Growth, 1999, 201, 236.

35 W. Yang, J. Shang, J. Wang, X. Shen, B. Cao, N. Peimyoo, C. Zou, Y. Chen, Y. Wang, C. Cong, W. Huang and T. Yu, Nano Lett., 2016, 16, 1560.

36 D. Xiao, G. B. Liu, W. Feng, X. Xu and W. Yao, Phys. Rev. Lett., 2012, 108, 196802.

37 A. M. Jones, H. Yu, N. M. Ghimire, S. Wu, G. Aivazian, J. S. Ross, B. Zhao, J. Yan, D. G. Mandrus, D. Xiao, W. Yao

and X. Xu, Nat. Nanotechnol., 2013, 8, 634.

38 M. Okada, Y. Miyauchi, K. Matsuda, T. Taniguchi, K. Watanabe, H. Shinohara and R. Kitaura, Sci. Rep., 2017,

7, 322.

39 A. Boulesbaa, B. Huang, K. Wang, M. W. Lin, M. M. Samani, C. Rouleau, K. Xiao, M. Yoon, B. Sumpter, A. Puretzky and D. Geohegan, Phys. Rev. B: Condens. Matter Mater. Phys., 2015, 92, 115443.

40 G. Plechinger, P. Nagler, A. Arora, A. G. del Aguila, M. Ballottin, T. Frank, P. Steinleitner, M. Gmitra, J. Fabian, P. C. M. Christianen, R. Bratschitsch, C. Schuller and T. Korn, Nano Lett., 2016, 16, 7899.

41 G. B. Liu, W. Y. Shan, Y. Yao, W. Yao and D. Xiao, Phys. Rev. B: Condens. Matter Mater. Phys., 2013, 88, 085433.

42 K. Kosmider, J. W. Gonzalez and J. Fernandez-Rossier, Phys. Rev. B: Condens. Matter Mater. Phys., 2013, 88, 245436.

43 A. Kormanyos, G. Burkard, M. Gmitra, J. Fabian, V. Zolyomi, N. D. Drummond and v. Falko, 2D Mater., 2015, 2, 022001.

44 K. D. Shiang, Surf. Sci., 1993, 292, 145.

45 X. H. Wang, J. Q. Ning, Z. C. Su, C. C. Zheng, B. R. Zhu, L. Xie, H. S. Wua and S. J. Xu, RSC Adv., 2016, 6, 27677.

46 K. Hao, J. F. Specht, P. Nagler, L. Xu, K. Tran, A. Singh, C. K. Dass, C. Schueller, T. Korn, M. Richter, A. Knorr, X. Li and G. Moody, Nat. Commun., 2017, 8, 15552.

47 Y. Zhang, Y. Zhang, Q. Ji, J. Ju, H. Yuan, J. Shi, T. Gao, D. Ma, M. Liu, Y. Chen, X. Song, H. Y. Hwang, Y. Cui and Z. Liu, ACS Nano, 2013, 7, 8963.

48 K. Kang, S. Xie, L. Huang, Y. Han, P. Y. Huang, K. F. Mak, C. J. Kim, D. Muller and J. Park, Nature, 2015, 520, 656.

Supporting information: Revealing the nature of low-temperature photoluminescence peaks by laser treatment in Van der Waals epitaxially grown WS2 monolayers

V. Orsi Gordo,[1, 2] M. A. G. Balanta,[1, 3] Y. Galvão Gobato,[1, *] F. S. Covre,[1] H. V. A. Galeti,[4] F. Iikawa,[2] O. D. D. Couto Jr.,[2] F. Qu,[5] M. Henini,[6, 7] D. W. Hewak,[8] and C. C. Huang[8, ǂ]

[1]Departamento de Física, Universidade Federal de São Carlos, 13565-905, São Carlos, SP, Brazil
[2]Instituto de Física "Gleb Wataghin", Universidade Estadual de Campinas, 13083-859, Campinas, São Paulo, Brazil
[3]Universidade Federal de Uberlândia-FACIP, 38304-402, Ituiutaba, MG, Brazil
[4] Departamento de Engenharia Elétrica, Universidade Federal de São Carlos, 13565-905, São Carlos, SP, Brazil
[5]Instituto de Física, Universidade de Brasília, Brasília-DF 70919-970, Brazil.
[6]School of Physics and Astronomy, University of Nottingham, Nottingham NG7 2RD, UK
[7]UNESCO-UNISA Africa Chair in Nanoscience.s/Nanotechnology Laboratories, College of Graduate Studies, University of South Africa (UNISA), Muckleneuk Ridge, P O Box 392, Pretoria, South Africa
[8]Optoelectronics Research Centre, University of Southampton, Southampton, SO17 1BJ, UK
(Dated: February 13, 2018)

I. STRUCTURAL CHARACTERIZATION OF VAN DER WAALS EPITAXIALLY (VDWE) GROWN MONOLAYERS

In this section, we present additional characterization results which demonstrate the large-scale uniformity of our Van der Waals epitaxially (VdWE) grown WS_2 monolayers. Figure S1(a), Figure S1(b), and Figure S1(c) show a photo, an optical microscope image, and a SEM image, respectively, of samples grown on 300 nm SiO_2 on a Si wafer. Figure S1(d) shows a picture of a WS_2 monolayer grown on quartz substrate. The images present no color variation/pattern and/or structural non-uniformity, thus demonstrating the large-scale homogeneity of the thin films. The samples are also homogeneous over larger scales such as 35 by 30 mm. As observed in Figure S1(a), the films on SiO_2/Si have a purple-ish colour which is due to optical contrast with the substrate. When the monolayer WS_2 is grown on quartz or c-plane sapphire substrates, the colour of the monolayer on these transparent substrates is usually light-yellow, as observed in previous reports [1,2]. This is shown in Figure S1(d) for a monolayers grown on quartz.

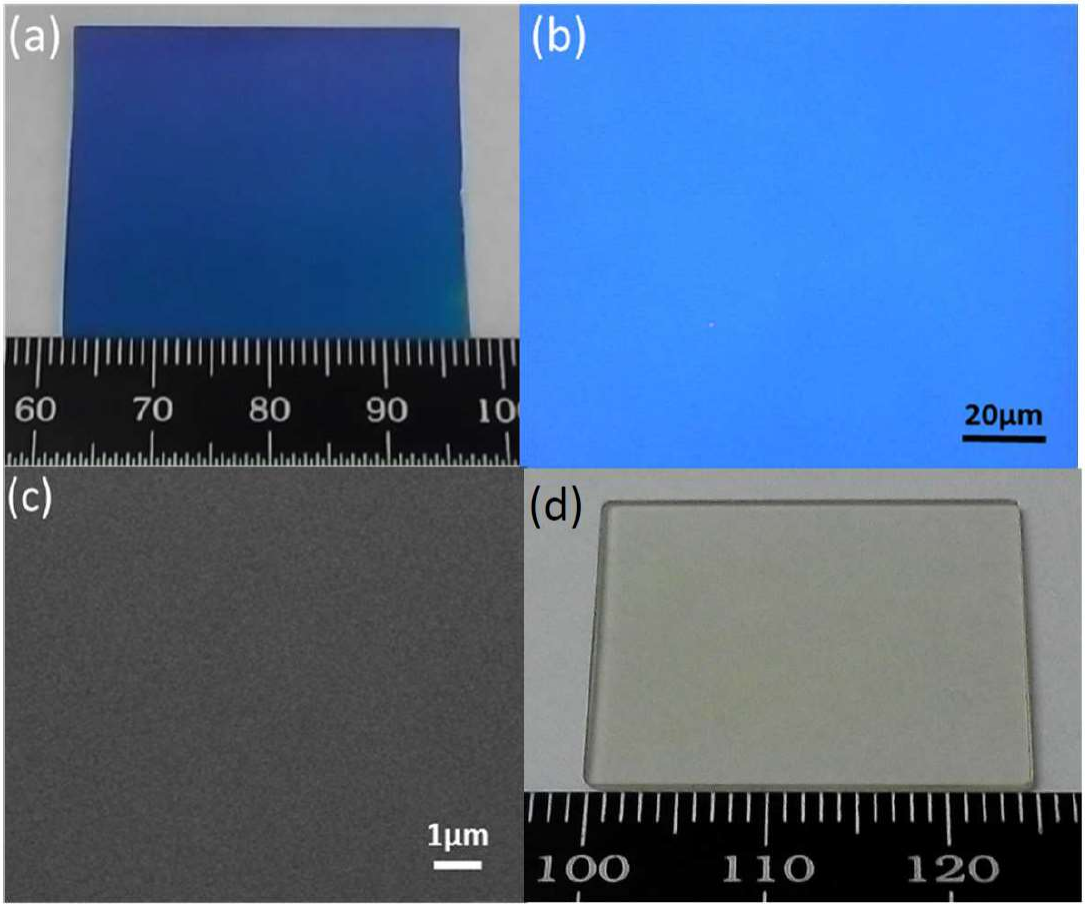

FIG. S1*: (a) A photo of VdWE-grown WS_2 monolayer on large-scale (35 mm by 30 mm) 300 nm SiO_2/Si wafer. (b) An optical microscope image of VdWE-grown WS_2 monolayer shown in (a). (c) A top view SEM image of VdWE-grown WS_2 monolayer shown in (a). (d) A photo of typical VdWE-grown WS_2 in quartz*

Figure S2 shows Raman spectroscopy characterization of the samples. Figure S2(a) illustrates Raman spectra (excited at 514.5 nm) obtained in VdWE-grown monolayer on SiO_2/Si substrates. We can clearly observe the two main Raman modes of WS_2 monolayers, namely the 2LA+ E1 (356 cm^{-1}) and A0(418.5 cm^{-1}) modes [3]. The inset in Figure S2(a) shows Raman spectra measured at 3 different positions separated by 6 mm along the surface of one of the samples. As it can be seen, the shape of the spectra and peak position do not vary with position on such scale. Figure S2(b) presents the intensity of the 2LA+ E1 mode (excited at 532 nm) obtained in a two-dimensional Raman mapping over an area of 4 mm by 5 mm. We observe relatively small variations in peak intensity over such large scale, which demonstrates the structural homogeneity of our WS_2 monolayer films. Figures S2(c) and (d) show Raman spectra (excited at 514.5 nm) of monolayer and few monolayers WS2 grown on quartz, respectively. Figure S2(c) shows that the Raman spectra of monolayers on quartz subtrates agree with the ones shown in Figure S2(a) for SiO_2/Si substrates. Comparing Figures S2(c) and (d), we observe an inversion of the relative intensity between the 2LA+ E1 and A0 peaks. This is a characteristic behavior of the Raman spectra of WS_2 when one goes from monolayer to more than one monolayer. Due to change in the band structure, the 2LA+ E1 mode scattering is a resonant process for monolayer samples for excitation at 514.5 nm, which makes the intensity of this peak higher than the A0[3].

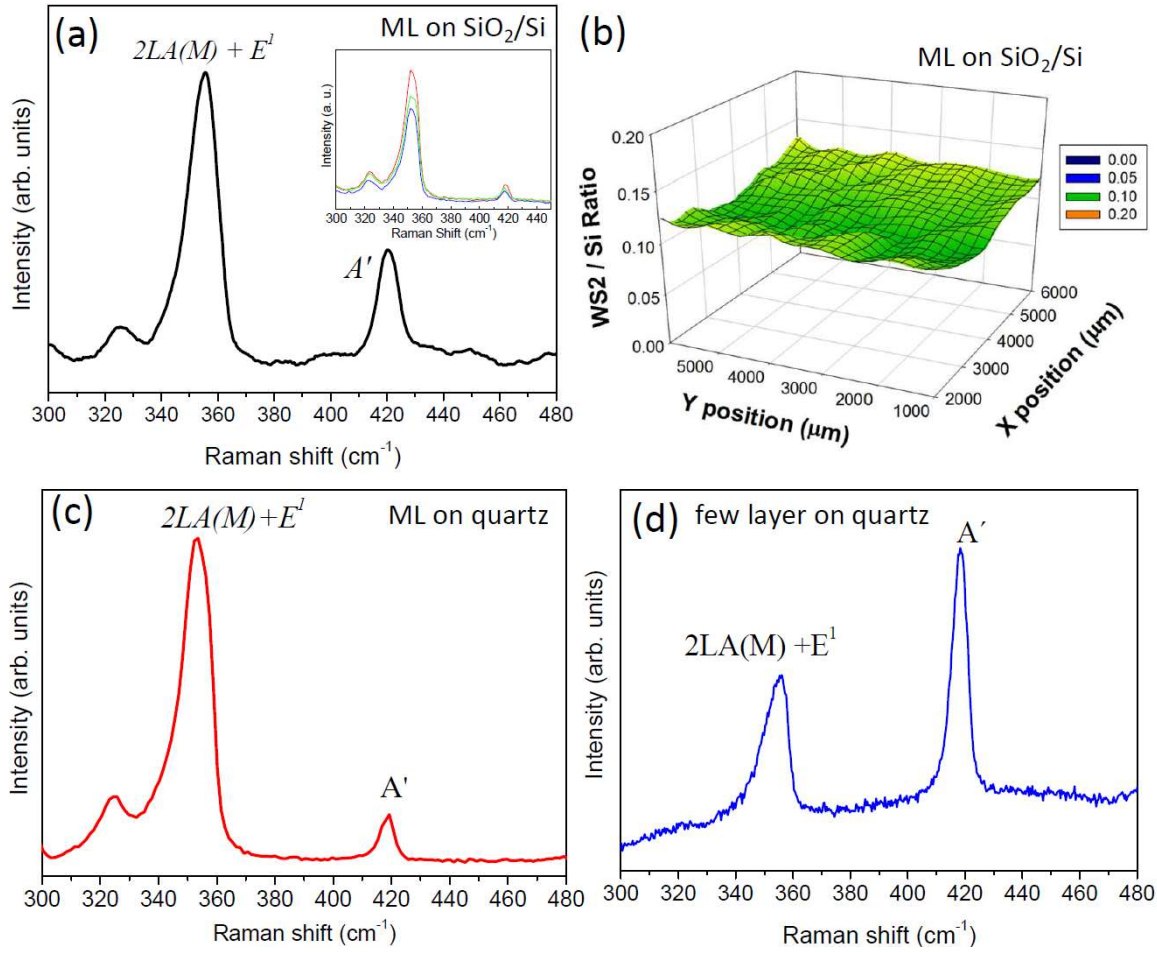

FIG. S2: *(a) Raman spectrum of VdWE-grown monolayer WS2 on SiO2/Si at 300K using 514.5 nm excitation with low laser power. The inset shows the Raman spectra at different positions on a dierent piece of the wafer. (b) Raman of VdWE-grown WS_2 monolayer on quartz. (c) Room temperature Raman spectra mapping of VdWE-grown monolayer WS_2 on 300nm SiO_2/Si substrate corresponding to the intensity ratio of WS_2 (2LA+E1) peak to Si peak over the area of 4 mm by 5 mm using 532 nm laser excitation. (d) Typical Raman spectrum of few monolayers of VdWE-grown WS2 on quartz at 300K using 514.5 nm laser excitation.*

Figure S3 presents the photoluminescence (PL) characterization of our samples at room temperature measured with 532 nm laser excitation. Figure S3(a) shows the PL of a monolayer grown on SiO_2/Si. The PL peak position at approximately 2.01 eV is in good agreement with previous literature reports [4]. Figure S3(b) shows the PL mapping at 2.009 eV over an area of 4 mm by 5 mm (the same area probed in Figure S2(b)), demonstrating good homogeneity in PL intensity over such scale in our VdWE samples. Figure S3(c) compares the emission energy position between a monolayer and a few monolayers WS_2 on quartz. As can be seen, the recombination energy decreases by approximately 27 meV as

additional layers are grown on the system, which is consistent with the bandgap decrease expected for such situation [5].

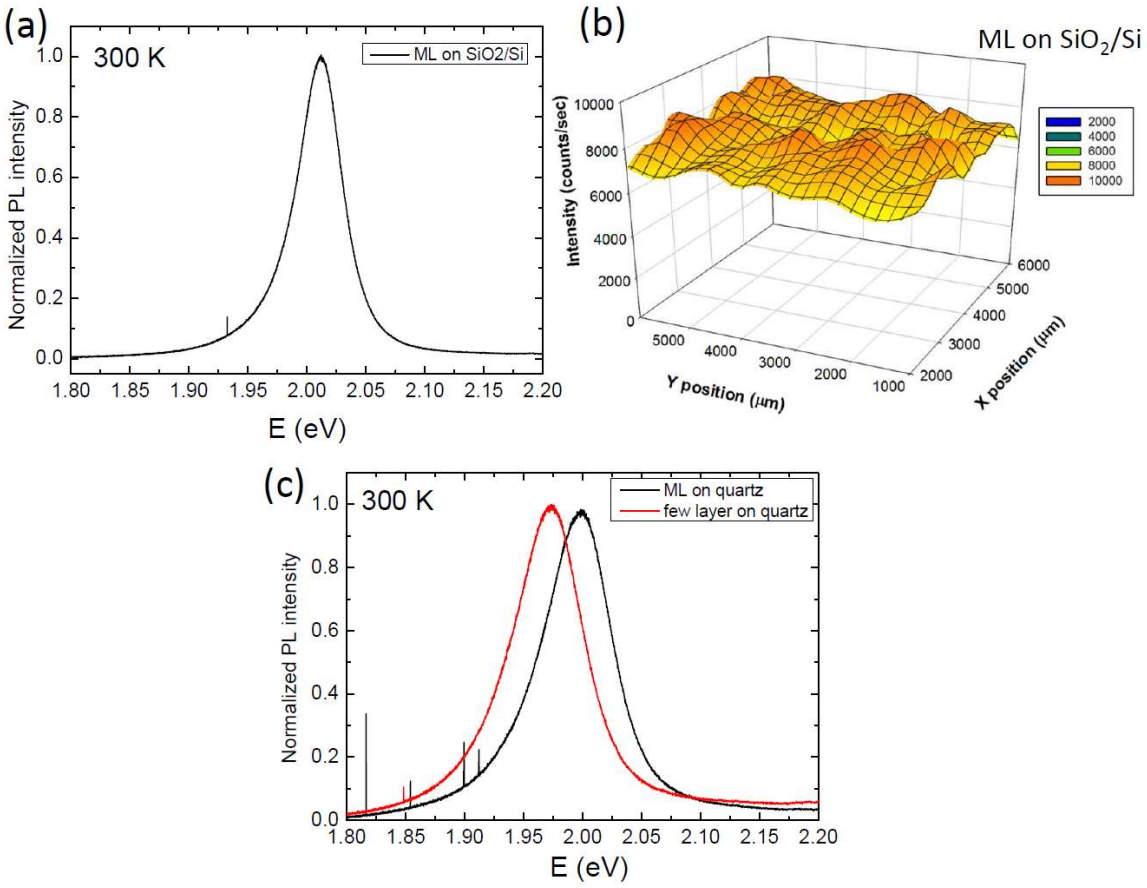

***FIG. S3**: (a) Typical room temperature PL spectrum of VdWE-grown monolayer WS2 on SiO2 using 532 nm laser line as excitation. 300K PL spectra mapping at 2.009eV of VdWE-grown monolayer WS_2 on 300nm SiO_2/Si substrate using 532 nm laser excitation for the same area on the sample shown in Figure S2(c). (c) PL spectra at 300K using 532 nm excitation at low laser power of monolayer and few monolayers of WS_2 on quartz substrate.*

* Electronic address: yara.ufscar@gmail.com

Ł Electronic address: cch@orc.soton.ac.uk

1 Y. Zhang, Y. Zhang, Q. Ji, J. Ju, H. Yuan, J. Shi, T. Gao, D. Ma, M. Liu, Y. Chen, et al., ACS Nano 7, 8963 (2013).

2 K. Kang, S. Xie, L. Huang, Y. Han, P. Y. Huang, K. F. Mak, C. J. Kim, D. Muller, and J. Park, Nature 520, 656 (2015).

3 A. Berkdemir, H. R. Gutierrez, A. R. Botello-Mendez, N. Perea-Lopez, A. L. Elias, C. I. Chia, B. Wang, V. H. Crespi, F. Lopez-Urias, J. C. Charlier, et al., Sci. Rep. 3, 1755 (2012).

4 A. Chernikov, T. C. Berkelbach, H. M. Hill, A. Rigosi, Y. Li, O. B. Aslan, D. R. Reichman, M. S. Hybertsen, and T. F. Heinz, Phys. Rev. Lett. 113, 076802 (2014).

5 H. R. Gutierrez, N. Perea-Lopez, A. L. Elias, A. Berkdemir, B. Wang, R. Lv, F. Lopez-Urias, V. H. Crespi, H. Terrones, and M. Terrones, Nano Lett. 13, 3447 (2013).

Artigo 2: Revealing the impact of strain in the optical properties of bubbles in monolayer $MoSe_2$

Nanoscale

ROYAL SOCIETY OF CHEMISTRY

PAPER

View Article Online
View Journal

Check for updates

Cite this: DOI: 10.1039/d2nr00315e

Revealing the impact of strain in the optical properties of bubbles in monolayer $MoSe_2$†

F. S. Covre,[a] P. E. Faria, Junior,[b] V. O. Gordo,[c] C. Serati de Brito,[a] Y. V. Zhumagulov,[b] M. D. Teodoro,[a] O. D. D. Couto, Jr.,[c] L. Misoguti,[d] S. Pratavieira,[d] M. B. Andrade,[d] P. C. M. Christianen,[e] J. Fabian,[b] F. Withers[f] and Y. Galvão Gobato*[a]

Strain plays an important role for the optical properties of monolayer transition metal dichalcogenides (TMDCs). Here, we investigate strain effects in a monolayer $MoSe_2$ sample with a large bubble region using μ-Raman, second harmonic generation (SHG), μ-photoluminescence and magneto μ-photoluminescence at low temperature. Remarkably, our results reveal the presence of a non-uniform strain field and the observation of emission peaks at lower energies which are the signatures of exciton and trion quasiparticles red-shifted by strain effects in the bubble region, in agreement with our theoretical predictions. Furthermore, we have observed that the emission in the strained region decreases the trion binding energy and enhances the valley *g*-factors as compared to non-strained regions. Considering uniform biaxial strain effects within the unit cell of the TMDC monolayer (ML), our first principles calculations predict the observed enhancement of the exciton valley Zeeman effect. In addition, our results suggest that the exciton–trion fine structure plays an important role for the optical properties of strained TMDC ML. In summary, our study provides fundamental insights on the behaviour of excitons and trions in strained monolayer $MoSe_2$ which are particularly relevant to properly characterize and understand the fine structure of excitonic complexes in strained TMDC systems/devices.

Received 17th January 2022,
Accepted 19th March 2022
DOI: 10.1039/d2nr00315e
rsc.li/nanoscale

Revealing the impact of strain in the optical properties of bubbles in monolayer MoSe2†

F. S. Covre,[a] P. E. Faria, Junior,[b] V. O. Gordo,[c] C. Serati de Brito,[a] Y. V. Zhumagulov,[b] M. D. Teodoro,[a] O. D. D. Couto, Jr.,[c] L. Misoguti,[d] S. Pratavieira,[d] M. B. Andrade,[d] P. C. M. Christianen,[e] J. Fabian,[b] F. Withers[f] and Y. Galvão Gobato*[a]

Received 17th January 2022,
Accepted 19th March 2022
DOI: 10.1039/d2nr00315e
rsc.li/nanoscale

[a] Departamento de Física, Universidade Federal de São Carlos, 13565-905 São Carlos, SP, Brazil. E-mail: yara@df.ufscar.br
[b] Institute for Theoretical Physics, University of Regensburg, 93040 Regensburg, Germany

[c] Instituto de Física “Gleb Wataghin”, Universidade Estadual de Campinas, 13083-859 Campinas, São Paulo, Brazil
[d] Instituto de Física de São Carlos – Universidade de São Paulo, CEP 13566-590 São Carlos, São Paulo, Brazil
[e] High Field Magnet Laboratory (HFML – EMFL), Radboud University, 6525 ED Nijmegen, The Netherlands
[f] College of Engineering, Mathematics and Physical Sciences, University of Exeter, Exeter EX4 4QF, UK

†Electronic supplementary information (ESI) available. See DOI: https://doi.org/10.1039/d2nr00315e

Strain plays an important role for the optical properties of monolayer transition metal dichalcogenides (TMDCs). Here, we investigate strain effects in a monolayer MoSe2 sample with a large bubble region using μ-Raman, second harmonic generation (SHG), μ-photoluminescence and magneto μ-photoluminescence at low temperature. Remarkably, our results reveal the presence of a non-uniform strain field and the observation of emission peaks at lower energies which are the signatures of exciton and trion quasiparticles red-shifted by strain effects in the bubble region, in agreement with our theoretical predictions. Furthermore, we have observed that the emission in the strained region decreases the trion binding energy and enhances the valley g-factors as compared to non-strained regions. Considering uniform biaxial strain effects within the unit cell of the TMDC monolayer (ML), our first principles calculations predict the observed enhancement of the exciton valley Zeeman effect. In addition, our results suggest that the exciton–trion fine structure plays an important role for the optical properties of strained TMDC ML. In summary, our study provides fundamental insights on the behaviour of excitons and trions in strained monolayer $MoSe_2$ which are particularly relevant to properly characterize and understand the fine structure of excitonic complexes in strained TMDC systems/devices.

I. Introduction

Monolayer (ML) transition metal dichalcogenide (TMDC) materials have attracted great attention in recent years due their unique optical and electrical properties for possible application in the next generation of optoelectronic devices.[1,2] Strain engineering is a powerful tool to control the physical properties of few layers of TMDCs and consequently it could be used for the development of strain based devices.[3-9] TMDCs can support large strain fields before they rupture which could open new opportunities for novel 2D devices.[4] It was previously shown that the presence of strain can change considerably the optical properties of ML TMDCs due to the change in band-gap, even inducing a direct to indirect transition.[10–16]

In addition, strain can also affect the value of the valley g-factors of ML TMDCs and consequently explain the dispersion of reported values in the literature.[17–22]

Strain-induced bubbles are usually formed during the transfer of ML TMDCs on the substrate and can create smooth[23–25] or localized strain profiles[25–28] depending on the size of the bubble. Localized strain in small bubbles usually gives rise to single photon emission with high brightness, which can be accurately controlled by the strain profile.[25] Larger bubbles can be prepared by different approaches and depending on the preparation technique the emission from these bubbles is very uniform and shows a strain-induced bandgap reduction as expected for a given monolayer/substrate combination.[25] Bubbles can also be formed by irradiating the sample with ionized hydrogen, which also offers the possibility to control the size, position, and shape of these dome-like structures.[25,29–31] Despite the availability of previous studies in the literature, the second harmonic generation (SHG) and the optical properties of TMDC bubbles as a function of temperature, laser power and magnetic field strength are far from being explored.

Here, we have investigated the impact of the strain and dielectric environment on the optical properties of a $MoSe_2$ ML sample with a large bubble region. We probed the optical properties of our sample at room and low temperatures and under perpendicular magnetic field. We have observed photoluminescence (PL) peaks at lower energies in the bubble region which were associated to a red-shift of the exciton and trion emissions due to the presence of tensile biaxial strain. This interpretation is consistent with our theoretical calculations and to our results of the PL decay times and the laser power and temperature dependence of the PL peaks. Furthermore, the observation of red-shifted Raman modes and the reduction of the SHG intensity in the bubble region confirms the presence of non-uniform biaxial tensile strain in the bubble region. Remarkably, we have observed a decrease of the trion binding energy, an increase of exciton and trion g factors and an increase of the exciton polarization degree in the bubble region. Performing realistic first principle calculations we confirm the enhancement of the valley g-factor due to the tensile biaxial strain, but we also found that additional mechanisms are present in the real sample. Particularly, we speculate that the spatial changes in the dielectric screening, doping and strain have a non-trivial impact on the fine structure of the excitons and trions. Our results offer new insights and open new opportunities to modify exciton and trion energies and g-factors in TMDC based devices under strain.

II. Results and discussion

a. SHG, PL and Raman characterization

Let us start with the general optical characterization of the studied sample. Fig. 1(a) shows the typical optical image of the monolayer $MoSe_2$/hBN/SiO_2 sample which is covered by Poly (methyl methacrylate) (PMMA). We remark that the dark image at the edge could be due an interference effect, related to region in which the layers are folded.[25,38] We observe the presence of some small bubbles with typical sizes of ∼1 μm and a large bubble with diameter size of ∼15 μm. These bubbles are filled with hydrocarbon (HC) residues.[39] Therefore, the $MoSe_2$ ML is not directly in contact to the h-BN substrate in these bubble regions. In order to probe the strain profile of this sample we have performed SHG, μ-Raman spectroscopy and μ-PL measurements as a function of the position (vertical black arrow in (a)).

Fig. 1(b) shows the SHG intensity mapping of our $MoSe_2$ sample at room temperature. The SHG measurements have a higher spatial resolution (around 600 nm) as compared to the PL and Raman measurements, which have typical spatial resolution of 1–3 μm depending on the actual experimental setup used. We remark that the SHG intensity decreases in the small bubbles and also within the large bubble. The SHG intensity is very sensitive to the structural configuration of 2D materials and therefore can also be used to probe position dependent strain in 2D materials.[40] It was shown that the presence of mechanical strain reduces the symmetry of a crystal and that even small strain values can have a considerable impact on the SHG intensity.[40–43] Interestingly, Fig. 1(b) also shows that the SHG intensity is not homogeneous in the large bubble region showing changes of the SHG intensity which evidences spatial variation of the biaxial strain in this region. Recent studies have evidenced doughnut-like patterns.[44–46] Our SHG results evidenced localized patterns in the bubble region (dark regions in SHG intensity mapping of Fig. 1(b)) which are similar to the doughnut-like patterns observed in nano-bubbles but with a more complex strain field. However, further studies using nano-optical measurements would be necessary to understand in more details the strain fields of larger bubbles. Furthermore, we also remark an important increase of SHG intensity on the edge of the bubble, which indicates the presence of compressive strain in this region. These SHG results are similar to previous results observed in folded and wrinkled regions in ML TMDCs.[43]

Fig. 1(c) shows the color plot of the position-dependent PL spectra of the $MoSe_2$ ML also at 4.2 K along the direction indicated by the vertical arrow in Fig. 1(a). We observe some small changes of the PL peak position in the flat region and an important red-shift in the large bubble region. In the flat region, we clearly observe two emission peaks associated to the neutral exciton (X) and the negatively charged exciton, or trion (T), as observed in other studies. Fig. 1(e) shows typical PL spectra in the flat and bubble regions at 4.2 K, at the positions indicated by the white dashed lines in Fig. 1(c). The exciton peak is observed at around 1.648 eV and the trion peak at an energy of about 1.619 eV. These PL peaks have a typical full width at half maximum (FWHM) of ≈8 meV. As expected the observed FWHM is higher than that usually observed for h-BN encapsulated samples, which we attribute to the broadening effect of disorder (inhomogeneous broadening).[47,48] Due to the local strain and dielectric[47] fluctuations in the flat region, these PL energy peaks also show small changes with the laser position. Furthermore, we remark that, near the edges of the bubble, a small blue shift of the PL peaks with respect to the flat region is observed, confirming the presence of compressive strain in this region, which is consistent with the observed increase of the SHG intensity and the blue shift of the Raman modes (see Fig. S3†). Remarkably, in the large bubble region we observed the emergence of red-shifted emission peaks (labelled L4 and L3) in the PL spectrum. An additional, less intense and broader emission peak, labelled L2, is also observed. These observed emission peaks in the bubble region are very sensitive to the laser position, consistent with a spatial variation of the strain. In particular, we observed that in the middle of the bubble the PL peaks are blue shifted relative to the PL in other regions in the bubble, indicating a complex spatial change of the strain on the bubble region, which is consistent to the SHG mapping and Raman results in this region. We also observed changes in the relative intensities of the trion and exciton PL intensities with varying position, attributed to the spatial variation in the doping level in the bubble region. We have estimated the doping level[49,50] for different studied positions and obtained values on the order of 1×10^{-12} cm^{-2}. For higher doping levels it is more difficult to observe spectra in which both L3 and L4 PL peaks are clearly peaks, because of the very intense trion (L3) peak, which is dominating the emission. As we are mainly interested in the effect of strain, we have focused our attention on positions on the sample with a relatively low doping level, in which both L3 and L4 peaks are visible in the PL spectrum, permitting a detailed study of the nature of these peaks.

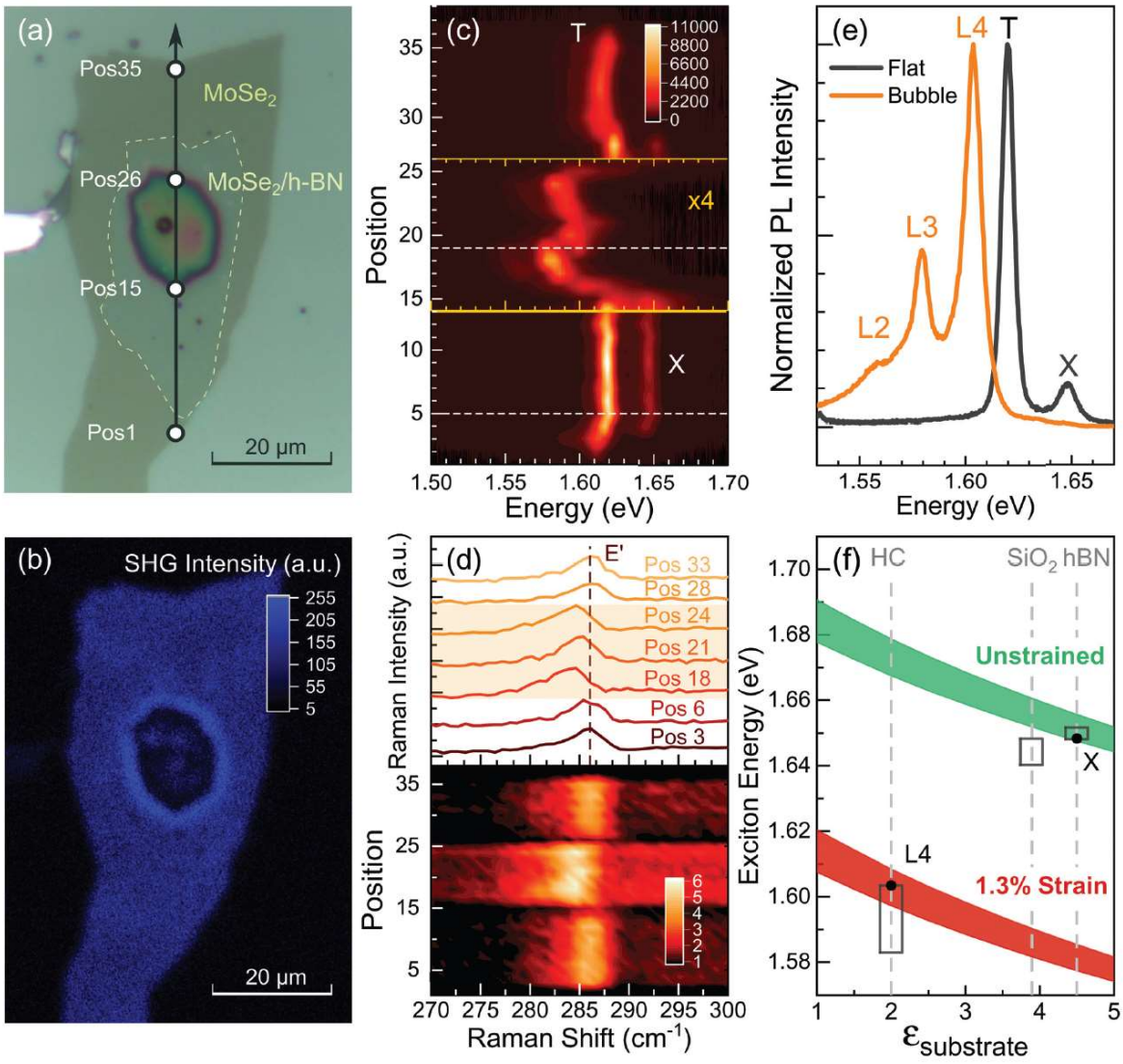

Figure 8 (a) *Optical microscope image of the MoSe2/hBN sample with a large bubble.* ***(b)*** *SHG intensity mapping at 300 K showing the intensity variation due to strain.* ***(c)*** *Color code map of the PL intensity (~1.5 μm step size) as a function of the position indicated by the vertical arrow in (a) measured with 488 nm laser excitation at 4 K.* ***(d)*** *E' Raman peak and color code map for different positions measured with 488 nm laser excitation at 4.2 K.* ***(e)*** *Typical PL spectra of the flat and bubble regions.* ***(f)*** *Theoretical dependence of the excitonic energy as a function of the dielectric constant of the substrate, indicated by the dashed vertical lines for HC,[32] SiO_2 33 and h-BN.[34,35] The unstrained and 1.3% tensile biaxial strain situations are shown. We considered $\varepsilon_t = 3$[36,37] for the top dielectric region composed of PMMA. The experimental data for the different regions (on h-BN, on SiO_2 and the bubble) is shown in rectangles. The excitonic peaks X and L4 from panel (e) are highlighted with the closed circles.*

Furthermore, we observed that the emission peaks in the bubble region are usually broader (FWHM ≈ 10 meV) than in the flat region (FWHM ≈ 8 meV). In general, it was

observed that the PL peaks in the bubble region are always red-shifted with respect to the emission peaks in the flat region, which indicates the presence of tensile strain (Fig. 1(c)). This redshift depends on the laser position. Typically, the PL peak energies of the emission peaks in the bubble region (Fig. 1(e)) ≈1.603 eV for the L4 peak, ≈1.579 eV for the L3 peak and ≈1.557 eV for the L2 peak. As mentioned above, this L2 band is broader and has much lower intensity. The laser power dependence of this L2 peak indicates that this emission could be associated to localized states (Fig. S4†). Therefore, we will focus our attention on the more intense and narrow L3 and L4 PL peaks. The nature of these emission peaks will be discussed in more detail below.

Further details of the strain profile in the sample are revealed through Raman spectroscopy. Usually, the Raman modes of ML TMDCs are red-shifted under increasing biaxial tensile strain and blue shifted under compressive strain.[51] In addition, it was shown that the polarization dependent Raman shows a splitting of the E' mode under uniaxial strain.[52,53] The position dependent E' Raman mode[54] is shown in Fig. 1(d), again for the positions along the arrow direction indicated in Fig. 1(a). In the bubble region, we have observed a red-shift (with a maximum value of ≈2 cm^{-1}) for the E' Raman mode, which confirms the presence of tensile strain. Similar results were also observed at room temperature. We remark that no splitting of the E' Raman mode was observed, which indicates the presence of biaxial strain. This result is consistent to our results of polarization resolved SHG (not shown here). We have estimated a maximum strain of about 1.3% on the bubble region. We also observe that the maximum strain does not occur in the middle of the bubble, suggesting a complex strain profile across the bubble. Furthermore, as mentioned above, we observed a small blue shift of Raman modes close to the edge of the large bubble (see Fig. S3†), which can affect the exciton energy at these regions. In general, the observed Raman results are consistent with the results of the PL and SHG intensity mapping.

To provide further insight into the complex behaviour of the optical spectra observed across the sample, we theoretically investigate the total energy of the exciton peak (specifically, the 1 s state of the A exciton) as a function of strain and dielectric environment. The exciton energy can be written as

$$E_A(\varepsilon, \varepsilon_t, \varepsilon_b) = E_g(\varepsilon_t, \varepsilon_b) - \Omega_A(\varepsilon_t, \varepsilon_b) + \Delta_A \varepsilon \quad (1)$$

in which ε is the strain, $\varepsilon_{t(b)}$ is the dielectric constant of the top (bottom) region adjacent to the TMDC, Eg is the TMDC band gap, Ω_A is the exciton binding energy and Δ_A is the gauge factor. The band gap and the binding energies depend on the dielectric constant of the top and bottom dielectric layers.[55] The effect of strain can be incorporated via the gauge factors. Using the Raman and PL data, we estimate a gauge factor of Δ_A = 54 meV $\%^{-1}$ for biaxial strain in the bubble region of our sample. We note that the gauge factor for biaxial strain is approximately twice the value of the gauge factor of uniaxial strain reported in experiments.[4,14,56–58]

We summarize in Fig. 1(f) the dependence of the exciton energy on the dielectric constant of the substrate and for different values of the biaxial strain (0% and 1.3%). The theoretical parameters used for $MoSe_2$ ML were obtained by analyzing several high-quality measurements[59–61] of the exciton energies in h-BN encapsulated samples. The ∼10 of meV energy window from the theoretical calculations account for the dielectric disorder present in real samples.[47] Looking at the measured exciton energy in the flat region, we note that they nicely fall on top of the theoretical curve for zero strain and h-BN substrate. For the bubble region (not on h-BN but on top of HC residues), we also found a very good agreement comparing the calculated exciton energies with the experimentally determined value of 1.3% of biaxial strain. The larger rectangular region incorporates the strain fluctuation in the bubble. Our results in Fig. 1(f) also reveal that the spectra taken at the SiO_2 region very close to the h-BN also exhibit a nonzero strain value, and hence shows a reduced exciton energy when compared to the unstrained curve. We also incorporate in Fig. 1(f) the selected peak positions X of the flat region and L4 of the bubble region [from Fig. 1(e)], since these are the two different spectra we investigate in further detail below. Additional details of the exciton calculations and parameters used to compute the exciton energy are discussed in the ESI.†

b. Temperature and laser power dependencies

In order to investigate in more detail the nature of the observed emission peaks in the bubble region, we have investigated the PL spectrum as a function of temperature and laser power for different positions on the $MoSe_2$ ML. Fig. 2 shows the PL spectra for the different positions labelled A1 and A2 in the optical microscope image in the inset of Fig. 2. Position A1 corresponds to the flat $MoSe_2$ ML which shows an exciton peak at ∼1.648 eV and a trion peak at ∼1.619 eV (Fig. 2(a)). Position A2 corresponds to the bubble region (also a region

with reduced doping). The PL spectrum from this region shows two lower energy peaks (at ~1.604 eV and ~1.579 eV) (Fig. 2(d)).

The temperature and laser power dependencies of the PL spectra were analyzed by fitting them by using Voigt functions. Fig. 2(c) and (f) show the double logarithmic representation of the PL intensity of the observed peaks as a function of laser power for both positions. The laser power dependence can be expressed as $I \alpha P^k$, where I is the integrated PL intensity and P the laser power. The k values for each emission peak are indicated in these figures. The obtained values are close to unity as expected for exciton and trion PL peaks. On the other hand, the laser power dependence of the L2 peak of Fig. 1(e) (laser power results in Fig. S4†) is not linear and at higher laser power has a slope lower than 1, which is typical for emission of localized states. As a consequence, we attribute L4 and L3 peaks on the bubble region to exciton and trion emission rather than originating from localized excitons. These peaks can not be associated to localized quantum emitters which are observed in regions with high local strains exhibiting sharp PL lines over a wide range of energies, usually at an energy below the trion emission.[62,63] Actually, the L4 and L3 emission peaks have typical linewidths that are much broader than these strain-induced quantum emitters. Previous studies of straindependent measurements on ML–$MoSe_2$ were performed at 300 K[56,64] and have shown a uniform red shift of the exciton and trion peak energy, without the appearance of lower-energy emission features. Furthermore, the emission from higher order exciton complexes for $MoSe_2$ ML, such as neutral or charged biexcitons, have also been observed at low temperatures at lower energy than the exciton PL peak.[65,66] However, their binding energies are not consistent with the energy positions of the L4 and L3 emission peaks and their linear laser power dependence. To further confirm the nature of L3 and L4 emission peaks we have investigated the temperature dependence of their integrated PL intensity, which usually provides key insights into a possible localized nature of PL peaks.[67]

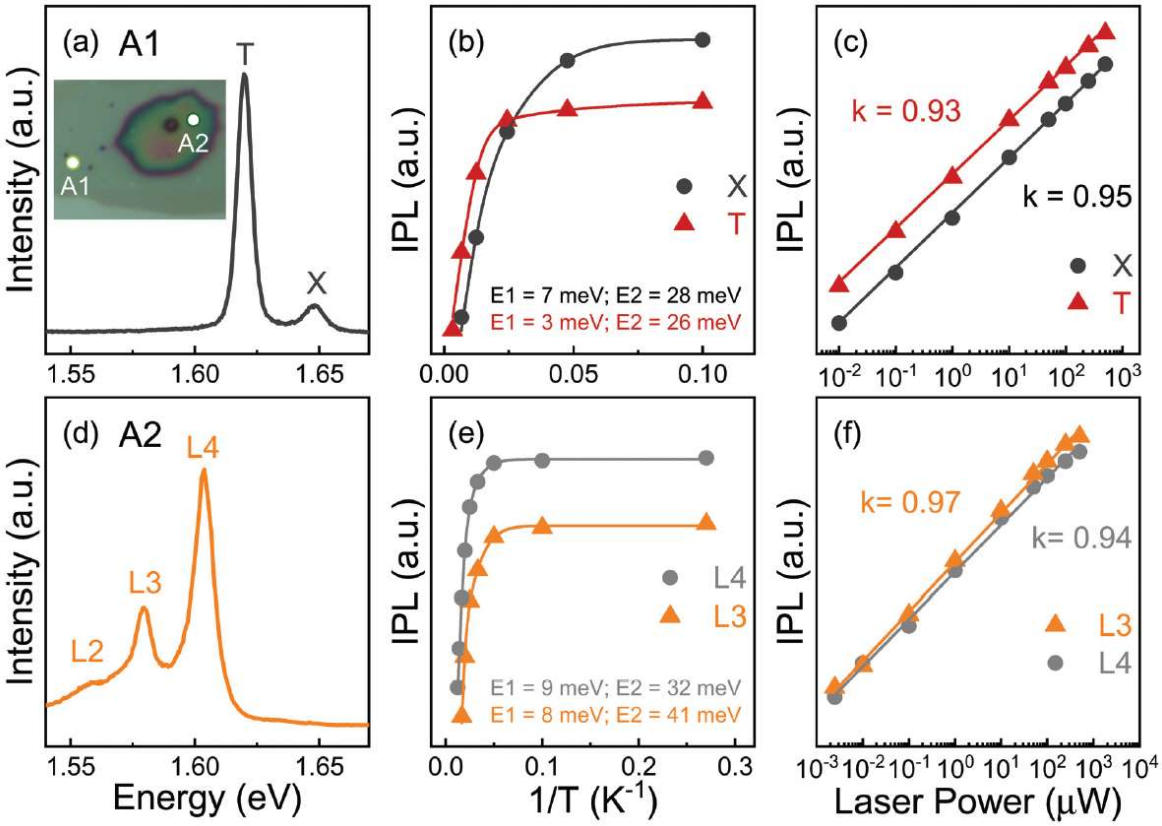

Figure 9 (a) *Typical PL spectrum of ML $MoSe_2$ for position A1 at 4 K.* ***(b)*** *Temperature and* ***(c)*** *laser power dependence of the integrated PL intensity for the peaks X and T using 405 nm laser excitation.* ***(d)*** *PL spectrum for position A2 at 4 K.* ***(e)*** *Temperature and* ***(f)*** *laser power dependence of the integrated PL intensity for L3 and L4 peaks using 730 nm laser excitation.*

The temperature dependence of the integrated PL intensity (Fig. 2(b) and (e)) was fitted using a modified Arrhenius formula:[68]

$$I(T) = \frac{I_0}{1 + a_1 e^{\frac{-E1}{k_B T}} + a_2 e^{\frac{-E2}{k_B T}}} \quad (2)$$

where I0 is the integrated PL intensity at T = 0 K, kB is the Boltzmann constant, and a_1 and a_2 are fitting parameters.[68] The temperature dependence arises from thermal equilibrium between dark and bright excitons (with a E1 separation) and the second term arises from defects and phonon scattering at higher temperatures (E2 energy scale).[68] Fig. 2-(b) and (e) show the curve fitting for the trion and exciton peaks for the A1 and A2 positions respectively. The obtained parameters for X, T, L4 and L3 have similar values, which

disregards a localization nature of the L4 and L3 emission peaks. Finally, we have performed time-resolved PL (RTPL) spectroscopy at 4.2 K for all emission peaks (Fig. S5†). We observed two PL decay components. A first fast component (τ_1), which is limited by our temporal resolution, and a long component (τ_2). We have observed that X, T, L3 and L4 have similar decay times. It is well known that the PL decay time of the bright exciton and trions are usually ∼1.8 and ∼15 ps respectively, depending on the thickness of the h-BN layer.[48,69] However, the exciton decay times can also increase to ∼100–300 ps if the bright excitons are localized.[70,71] For defect bound bright exciton longer values are usually observed with typical PL decay times of ∼200 ns.[72] In addition, for dark excitons/trions values of decay times of ∼1.3 ns[73] were usually observed. In addition, we remark that the long decay times observed for all emission peaks have similar values which are usually observed for excitons trapped by deep localized states or for emission of dark states. In general, the obtained decay time values in the region of the bubble sample do not indicate that the main contribution to these peaks (L3 and L4) could be due to localized exciton emission as it is also not consistent with the temperature and laser power dependence of PL peaks.

Furthermore, we observed that the energy separation of L4 and L3 is smaller (≈24 meV) than the energy separation between X and T (≈28 meV). It was previously reported that the trion binding energy depends on strain[74] and the dielectric environment.[75–77] Particularly, since the trion binding energy increases with a decreasing dielectric constant,[75,76] the observed reduction of the trion binding energy in the bubble region can be attributed to the presence of tensile biaxial strain. As a result, we associate the L4 and L3 mainly to the exciton and trion emission, respectively, which are red-shifted due to biaxial tensile strain. We also remark that the L4 exciton peak is more intense than the L3 trion peak in this region. Therefore, for this laser position our experimental results show that the $MoSe_2$ ML has reduced doping relative to the flat region. A detailed spatial mapping of the PL intensity in the bubble region show a significant spatial dependence of doping (see the PL spectrum for another laser position in Fig. S6†). In order to probe the effect of the strain on magnetooptical properties in the bubble region, we have focused our attention in the positions with reduced doping (namely, the position A2).

c. Magneto-optics

We now turn to the magneto-PL properties of the studied sample under a perpendicular magnetic field. Fig. 3(c) and (d) show typical circularly polarized PL spectra for the flat and bubble regions at 0 and 6 T, respectively. Additionally, Fig. 3(e) and (f) show the resulting field-dependent valley Zeeman splitting, ΔE, fitted (solid curves) using

$$\Delta E = E^{\sigma+} - E^{\sigma-} = g\mu_B B \quad (3)$$

where $\mu_B = 58\ \mu eV\ T^{-1}$ is the Bohr magneton, B is the applied magnetic field, and g is the valley g-factor. $E^{\sigma+}$ and $E^{\sigma-}$ are the peak energies of the σ^+ or σ^- polarized PL of each species. For position A1 (flat region), we obtained $g_X \approx -4.3$ and for $g_T \approx -4.4$ in agreement with the literature values.[19,78] For the A2 position (bubble region) we obtained $g_{L3} \approx -5.9$ and $g_{L4} \times -4.8$ for the L3 and L4 emission peaks, respectively (Fig. 3(f)). The estimated error for the extracted g-factors is ≈0.1.

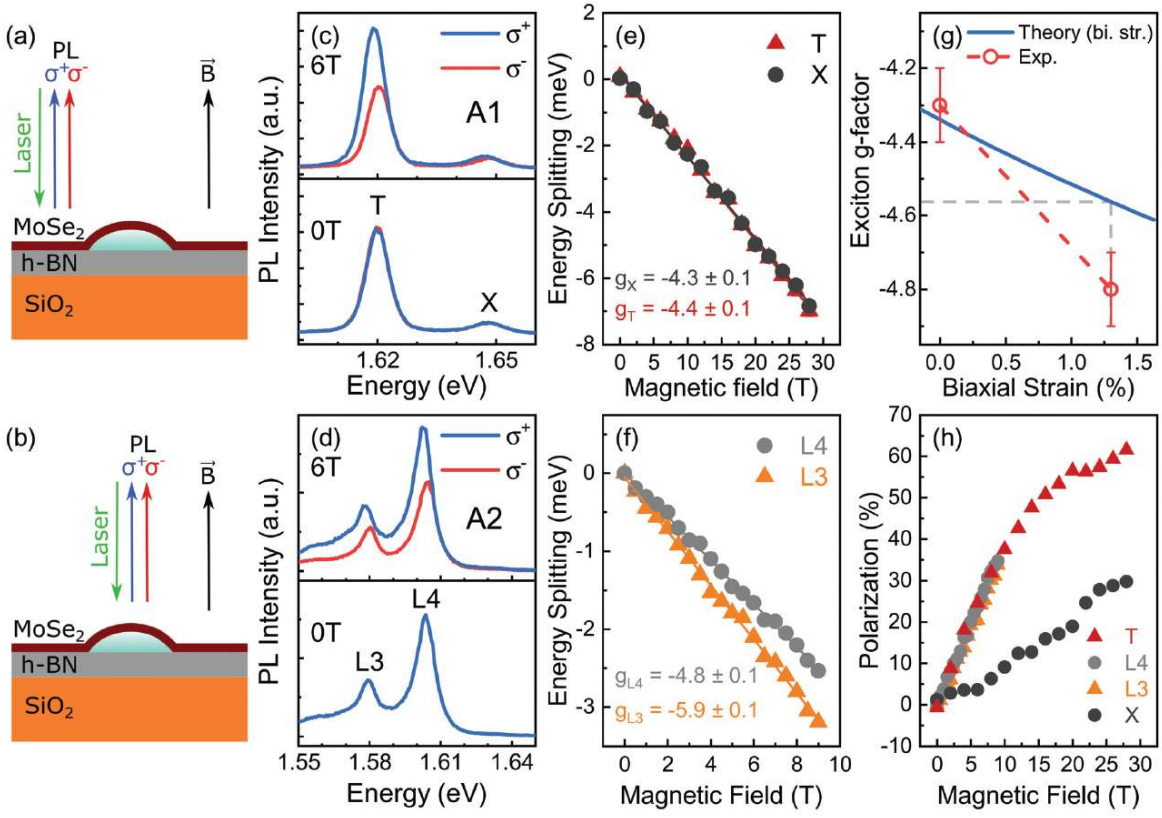

Figure 10 *Schematic representation of the magneto-PL experiment for the $MoSe_2$ ML under perpendicular magnetic field in the* ***(a)*** *unstrained and* ***(b)*** *bubble regions. Typical polarized resolved PL at 6 T*

*at 4 K for the **(c)** flat region, position A1, and **(d)** bubble region, position A2. **(e)** and **(f)** Magnetic field dependence of the exciton splitting for positions A1 and A2 respectively. **(g)** Theoretical prediction of the exciton g-factor as a function of biaxial strain calculated from first principles (blue curve), compared to the experimental values (red curves) for the exciton. **(h)** Circular polarization degree of different emission peaks as a function of magnetic field.*

To understand the isolated impact of biaxial strain on the A exciton g-factor, we perform first principles calculations of the orbital angular momentum of the bands that constitute the excitonic states.[17,79–81] These theoretical developments have been corroborated by recent experiments that were able to disentangle the electron and hole g-factor contributions in the observed exciton g-factor, providing an excellent agreement to the measured values.[82,83] Within this approach we have access to the g-factors of the conduction, g_c, and valence, g_v, bands that constitute the A exciton at one specific valley. The final g-factor of the A exciton is then written as $g_A = 2(g_c - g_v)$ and incorporates the effect of strain calculated directly from first principles. Our calculations for the A exciton g-factor under biaxial strain, shown in Fig. 3(g), reveal that tensile strain increases the exciton g-factor (in absolute value), in line with the experimental measurements. Therefore, based on these g-factor calculations and the analysis of previous sections, we then associate the observed increase of the exciton g-factor in the bubble region, as compared to the flat region, to the presence of a biaxial tensile strain. We note however that our g-factor calculations consider solely the A exciton g-factor, which consistently supports the interpretation of the L4 peak being mainly an exciton state with a g-factor of −4.8. The L3 peak with a g-factor of −5.9 is then attributed to trion emission. Further details of the first principles calculations are given in the ESI.†

Let us now analyze the comparison in Fig. 3(g) on more quantitative grounds. Our first principles calculations consider a uniform biaxial strain (as a limiting case of the non-uniform strain present in the sample), which directly probes the fundamental microscopic and intrinsic physics at the K valleys, indeed predicting an enhancement of the valley g-factors. However, the exciton g-factor enhancement of ∼0.22 (−4.34 at 0 strain to −4.56 at 1.3% strain) is not as large as the experimental value of ∼0.5 (from −4.3 to −4.8). For the trion state, the valley g-factor enhancement is even larger, ∼1.1 (from −4.8 to −5.9). This suggests that there are additional contributions to the valley g-factors beyond the influence of strain on the orbital level, and, these contributions very likely depend on the particular strain value (and how uniform it is), the doping and the dielectric environment, thus influencing the fine structure of

exciton and trion states. For instance, recent experiments in ML MoS_2 revealed that doping effects drastically modify the exciton and trion g-factors[84] and that the fine structure of trions is indeed relevant, with different g-factors associated to different trion states.[85] Furthermore, recent calculations have shown that the interplay of doping and dielectric confinement can significantly alter the fine structure of excitons and trions.[86] Although there has been some recent developments on the theory of magneto-excitons[87–89] and doping effects on trions,[77,86,90] a more complete picture that incorporates magnetic field, strain effects, doping, and dielectric confinement on an equal footing is still missing. Our results thus highlight the need for further theoretical developments along this line.

Besides the g-factors, we also analyzed the degree of the valley polarization, defined as $P = (I^{\sigma+} - I^{\sigma-})/(I^{\sigma+} + I^{\sigma-})$. The value of P is shown in Fig. 3(h) as a function of magnetic field. We observed that the polarization degree is zero at 0 T for all emission peaks and increases with increasing field strength as expected. We remark that the field-induced exciton polarization has a lower value than the trion polarization. Actually, the trion PL emission usually has a longer decay time and much longer inter-valley scattering time, which explains its higher field induced circular polarization as compared to the polarization of exciton PL.[91] Furthermore, we observed that in the bubble region the field induced exciton polarization is higher than in the flat region. As mentioned previously it was observed that the exciton PL decay in the bubble region is longer than in the flat region (Fig. S5†). As the valley polarization depends on the intervalley scattering time and exciton lifetimes as well, the observed increase of magnetic field induced exciton polarization is probably due to a higher increase of intervalley scattering times in the bubble region which could be due to an enhanced contribution of dark states induced by the presence of biaxial strain. However, further studies are needed to understand this result in more detail.

In general, most of the laser positions in the bubble regions show L2, L3 and L4 emission peaks (please see Fig. 1(c) or Fig. S4†). However, as discussed previously, the strain in the bubble region is not homogeneous as evidenced by the SHG intensity image (Fig. 1(b)) and Raman results (Fig. 1(e)). In particular, it was observed that for some laser positions it is possible to collect the PL signal from regions with different strains and doping. Fig. S6† shows the magnetic field dependence of the degree of circular polarization for a different position (labelled A5) in the bubble region with higher doping which shows the emission peaks X, T1, T2, L3 and L4. For this laser position (A5), the magnetic field dependence of the PL spectrum is more complex. The magnetic field dependence of the emission peaks shows

an unusual behaviour. We have extracted the g-factor for the X emission peak resulting g-factor $g_X \approx -6.1$ (Fig. S6†). This value of g-factor is much higher than that the g-factor of the exciton observed in the flat region. The energy separation between dark and bright exciton states can change as a function of the amount of strain and the value of the dielectric constant.[9] In addition, effects of disorder could result in some brightening of spin dark exciton states, which could also give some mixed contributions (unresolved bright + dark emissions).[92,93] However, our obtained values of the g-factor are not consistent with a large contribution of dark states to the exciton PL in the bubble region.[21] Further studies in $MoSe_2$ ML samples with controlled strain would be necessary to understand in detail if there is a possible contribution of dark states in strained TMDs deposited on different substrates.

In general, the observed results for different laser positions show that the tensile biaxial strain induces a red-shift of the exciton peak energy in ML $MoSe_2$ and enhances its exciton g-factor. However, this enhancement seems to depend on other effects as well, such as doping and the fine structure of the exciton and trion states. Finally, our investigations show that biaxial strain has an important impact on the low temperature optical and magneto-optical properties of excitons and trions in monolayer $MoSe_2$, which are particularly relevant to properly characterize and understand the fine structure of excitons and trions in strained TMDC systems.

III. Experimental methods

a. Sample preparation

The sample was prepared through a dry transfer technique. Monolayer $MoSe_2$ was produced by exfoliation of bulk crystals (HQgraphene) onto a PVA/PMMA double layer. The $MoSe_2$ monolayer was subsequently identified using optical microscopy. To transfer the $MoSe_2$, the PVA was dissolved using water (without water coming into contact with flakes on the PMMA). The PMMA membrane together with the monolayer $MoSe_2$ subsequently float on top of DI water. The PMMA membrane is then lifted with a metallic membrane holder, dried, and then inverted before being aligned using micromanipulators and microscopy to cover a h-BN crystal exfoliated onto SiO_2. After transfer, the membrane together with $MoSe_2$ are heated at 130 degrees for 10 min to improve adhesion to the substrate. The large quantity of trapped contamination was a random event, likely due to contaminated $MoSe_2$ after

exfoliation or contaminated h-BN on SiO_2. No special fabrication approach was used to increase the probability of bubble formation.

b. Optical measurements

Optical measurements at B = 0 T were performed in homemade μ-PL and μ-Raman setups using 405 nm/488 nm laser excitation, a 50× Mitutoyo objective and a 50 cm spectrometer coupled with a silicon CCD detector (Andor, Shamrock/iDus). A Horiba LabRAM HR Evolution system with a 1800 g mm^{-1} grating and a 50× objective was also used for complementary μ-Raman measurements with 633 nm laser excitation. For magneto-PL measurements, the sample was mounted on Attocube piezoelectric x–y–z translation stages in order to control the sample position. In addition, this system was placed inside a helium closed-cycle cryostat with superconducting magnet coils (Attocube – Attodry1000) with the magnetic field up to 9 T perpendicular to the sample. PL measurements were performed using a continuous-wave (cw) laser with a photon energy of 2.33 or 1.70 eV. The PL signal was collimated by an aspheric lens (NA = 0.64) and the selection of circular polarization components was performed before to be focused into a 50 μm multimode optical fiber, being dispersed by a 75 cm spectrometer and detected by a silicon CCD detector (Andor, Shamrock/iDus). For higher magnetic field measurements a Bitter magnet was used allowing for magnetic fields up to B = 30 T. PL measurements were performed using a cw green laser with photon energy of 2.33 eV. The laser was focused by an Attocube objective (40× and numerical aperture NA = 0.55) with spot size of about 3 μm. The resultant PL signal was collected by the same objective and measured by a Princeton spectrometer (Acton SpectraPro-300i) equipped with a liquid-nitrogen cooled CCD PyLoN from Princeton Instruments. Circular polarization for excitation and detection were controlled independently with appropriated optics and a Faraday configuration was used. Time resolved PL measurements were performed at 0 T by means of a standard TCSPC technique (PicoQuant/Picoharp 300) using a 1.69 eV pulsed laser (PicoQuant/LDH Serie) delivering 70 ps pulses at a repetition frequency of 80 MHz with the signal dispersed by a 75 cm spectrometer and detected by a hybrid PMT device (PicoQuant). SHG intensity mapping measurements were performed using an inverted Zeiss Laser Scanning Microscope (model LSM 780), a mode locked fs pulsed Ti-Sapphire laser at 800 nm wavelength (Coherent Chameleon) and 20× objective (0.8 NA).

IV. Conclusions

In summary, we have investigated the optical and magnetooptical properties of strained $MoSe_2$ ML bubbles at low temperature. We have observed an significant red-shift of the emission peaks (≈45 meV), a red-shift of the Raman modes (≈2 cm^{-1}) and a large reduction of the SHG intensity which depends on the laser position. These results evidence the presence of non-uniform tensile strain of maximum value ≈1.3% in the bubble region. Furthermore, the analysis of time resolved and temperature and laser power-dependent PL reveals that the nature of the most intense lines are the same for the bubble and flat regions. As a result, we attributed the dominant emission from the bubble region to exciton and trion emission rather than to localized excitonic states. We observed a lower value for the trion binding energy (≈24 meV) in the bubble region as compared to ≈28 meV in the nonstrained region of $MoSe_2$ ML. Remarkably, a significant increase in the valley Zeeman g-factor was observed in the bubble region (from −4.3 to −4.8 for excitons and from −4.4 to −5.9 for trions). The valley g-factor enhancement of excitons can be qualitatively captured by our first principles calculations. However, our results reveal that only the influence of strain on the orbital level is not enough to explain our experimental findings. Particularly, our experimental values suggest that the exciton and trion fine structure plays an important role here and it is quite sensitive to strain, doping and dielectric confinement, thus requiring further theoretical investigations to incorporate these effects on an equal footing. In general, our findings open new routes to modify energies and g-factors of excitonic complexes in TMDC monolayers materials which are particularly relevant to the development of systems with controlled strain.

Conflicts of interest

There are no conflicts to declare.

Acknowledgements

This work has been supported by “Fundação de Amparo a Pesquisa do Estado de São Paulo” (FAPESP) (grants no. 2009/54035-4, 12/11382-9, 14/19142-2, 13/18719-1, 18/01808-5 and 19/23488-5), Conselho Nacional de Desenvolvimento Científico e Tecnológico (CNPq) (grants 426634/2018-7, 311678/2020-3 and 306107/2019-8) and by HFML-RU/NWO-I, member of the European Magnetic Field Laboratory (EMFL). P. E. F. J. and J. F. acknowledge the financial support of the Deutsche Forschungsgemeinschaft (DFG, German Research Foundation) SFB 1277 (Project-ID 314695032, projects B07 and B11), SPP 2244

(Project No. 443416183), and the European Union Horizon 2020 Research and Innovation Program under contract number 881603 (Graphene Flagship). F. S. C. and C. S. B. acknowledges the CNPq and Capes, respectively, for the financial support of their PhD fellowships. We acknowledge F. Iikawa for preliminary optical characterization and helpful discussions, J. Buhot and M. Ballottin for the optical alignment of the magneto-PL setup in HFML-Nijmegen and J. F. Felix for helpful discussions regarding the sample preparation.

References

1 A. K. Geim and I. V. Grigorieva, Nature, 2013, 499, 419–425.

2 K. S. Novoselov, A. Mishchenko, A. Carvalho and A. H. C. Neto, Science, 2016, 353, aac9439.

3 S. Deng, A. V. Sumant and V. Berry, Nano Today, 2018, 22, 14–35.

4 Z. Peng, X. Chen, Y. Fan, D. J. Srolovitz and D. Lei, Light: Sci. Appl., 2020, 9, 1–25.

5 S. Yang, Y. Chen and C. Jiang, InfoMat, 2021, 3, 397–420.

6 A. Castellanos-Gomez, R. Roldán, E. Cappelluti, M. Buscema, F. Guinea, H. S. J. van der Zant and G. A. Steele, Nano Lett., 2013, 13, 5361–5366.

7 H. Li, A. W. Contryman, X. Qian, S. M. Ardakani, Y. Gong, X. Wang, J. M. Weisse, C. H. Lee, J. Zhao, P. M. Ajayan, J. Li, H. C. Manoharan and X. Zheng, Nat. Commun., 2015, 6, 1–7.

8 F. Li, T. Shen, C. Wang, Y. Zhang, J. Qi and H. Zhang, Nano-Micro Lett., 2020, 12, 1–44.

9 F. Dirnberger, J. D. Ziegler, P. E. Faria Junior, R. Bushati, T. Taniguchi, K. Watanabe, J. Fabian, D. Bougeard, A. Chernikov and V. M. Menon, Sci. Adv., 2021, 7, eabj3066.

10 D. Lloyd, X. Liu, J. W. Christopher, L. Cantley, A. Wadehra, B. L. Kim, B. B. Goldberg, A. K. Swan and J. S. Bunch, Nano Lett., 2016, 16, 5836–5841.

11 H. J. Conley, B. Wang, J. I. Ziegler, J. R. F. Haglund, S. T. Pantelides and K. I. Bolotin, Nano Lett., 2013, 13, 3626–3630.

12 P. Johari and V. B. Shenoy, ACS Nano, 2012, 6, 5449–5456.

13 G. Plechinger, A. Castellanos-Gomez, M. Buscema, H. S. J. van der Zant, G. A. Steele, A. Kuc, T. Heine, C. Schüller and T. Korn, 2D Mater., 2015, 2, 015006.

14 R. Frisenda, M. Drüppel, R. Schmidt, S. M. De Vasconcellos, D. P. de Lara, R. Bratschitsch, M. Rohlfing and A. Castellanos-Gomez, npj 2D Mater. Appl., 2017, 1, 1–7.

15 R. Yang, J. Lee, S. Ghosh, H. Tang, R. M. Sankaran, C. A. Zorman and P. X.-L. Feng, Nano Lett., 2017, 17, 4568– 4575.

16 Y. Y. Hui, X. Liu, W. Jie, N. Y. Chan, J. Hao, Y.-T. Hsu, L.-J. Li, W. Guo and S. P. Lau, ACS Nano, 2013, 7, 7126– 7131.

17 T. Woźniak, P. E. Faria Junior, G. Seifert, A. Chaves and J. Kunstmann, Phys. Rev. B, 2020, 101, 235408.

18 A. Arora, M. Koperski, A. Slobodeniuk, K. Nogajewski, R. Schmidt, R. Schneider, M. R. Molas, S. M. de Vasconcellos, R. Bratschitsch and M. Potemski, 2D Mater., 2018, 6, 015010.

19 D. MacNeill, C. Heikes, K. F. Mak, Z. Anderson, A. Kormányos, V. Zólyomi, J. Park and D. C. Ralph, Phys. Rev. Lett., 2015, 114, 037401.

20 A. A. Mitioglu, K. Galkowski, A. Surrente, L. Klopotowski, D. Dumcenco, A. Kis, D. K. Maude and P. Plochocka, Phys. Rev. B, 2016, 93, 165412.

21 C. Robert, B. Han, P. Kapuscinski, A. Delhomme, C. Faugeras, T. Amand, M. R. Molas, M. Bartos, K. Watanabe, T. Taniguchi, B. Urbaszek, M. Potemski and X. Marie, Nat. Commun., 2020, 11, 1–8.

22 G. Wang, L. Bouet, M. M. Glazov, T. Amand, E. L. Ivchenko, E. Palleau, X. Marie and B. Urbaszek, 2D Mater., 2015, 2, 034002.

23 J. Feng, X. Qian, C.-W. Huang and J. Li, Nat. Photonics, 2012, 6, 866–872.

24 A. V. Tyurnina, D. A. Bandurin, E. Khestanova, V. G. Kravets, M. Koperski, F. Guinea, A. N. Grigorenko, A. K. Geim and I. V. Grigorieva, ACS Photonics, 2019, 6, 516–524.

25 E. Blundo, E. Cappelluti, M. Felici, G. Pettinari and A. Polimeni, Appl. Phys. Rev., 2021, 8, 021318.

26 S. Kumar, A. Kaczmarczyk and B. D. Gerardot, Nano Lett., 2015, 15, 7567–7573.

27 A. Branny, S. Kumar, R. Proux and B. D. Gerardot, Nat. Commun., 2017, 8, 1–7.

28 C. Palacios-Berraquero, D. M. Kara, A. R.-P. Montblanch, M. Barbone, P. Latawiec, D. Yoon, A. K. Ott, M. Loncar, A. C. Ferrari and M. Atatüre, Nat. Commun., 2017, 8, 1–6.

29 E. Blundo, M. Felici, T. Yildirim, G. Pettinari, D. Tedeschi, A. Miriametro, B. Liu, W. Ma, Y. Lu and A. Polimeni, Phys. Rev. Res., 2020, 2, 012024.

30 D. Tedeschi, E. Blundo, M. Felici, G. Pettinari, B. Liu, T. Yildrim, E. Petroni, C. Zhang, Y. Zhu, S. Sennato, Y. Lu and A. Polimeni, Adv. Mater., 2019, 31, 1903795.

31 E. Blundo, C. D. Giorgio, G. Pettinari, T. Yildirim, M. Felici, Y. Lu, F. Bobba and A. Polimeni, Adv. Mater. Interfaces, 2020, 7, 2000621.

32 A. Sen, V. Anicich and T. Arakelian, J. Phys. D: Appl. Phys., 1992, 25, 516.

33 T. C. Berkelbach, M. S. Hybertsen and D. R. Reichman, Phys. Rev. B: Condens. Matter Mater. Phys., 2013, 88, 045318.

34 A. V. Stier, N. P. Wilson, K. A. Velizhanin, J. Kono, X. Xu and S. A. Crooker, Phys. Rev. Lett., 2018, 120, 057405.

35 R. Geick, C. H. Perry and G. Rupprecht, Phys. Rev., 1966, 146, 543–547.

36 V. K. Thakur, D. Vennerberg, S. A. Madbouly and M. R. Kessler, RSC Adv., 2014, 4, 6677–6684.

37 Z. Shi, L. Song and T. Zhang, J. Infrared, Millimeter, Terahertz Waves, 2019, 40, 80–91.

38 H. Luo, X. Li, Y. Zhao, R. Yang, L. Bao, Y. Hao, Y. N. Gao, N. N. Shi, Y. Guo, G. Liu, L. Zhao, Q. Wang, Z. Zhang, G. Zhang, J. Sun, Y. Huang, H. Gao and X. Zhou, Phys. Rev. Mater., 2020, 4, 074006.

39 S. J. Haigh, A. Gholinia, R. Jalil, S. Romani, L. Britnell, D. C. Elias, K. S. Novoselov, L. A. Ponomarenko, A. K. Geim and R. Gorbachev, Nat. Mater., 2012, 11, 764–767.

40 L. Mennel, M. M. Furchi, S. Wachter, M. Paur, D. K. Polyushkin and T. Mueller, Nat. Commun., 2018, 9, 1– 6.

41 J. Liang, J. Zhang, Z. Li, H. Hong, J. Wang, Z. Zhang, X. Zhou, R. Qiao, J. Xu, P. Gao, Z. Liu, Z. Liu, Z. Sun, S. Meng, K. Liu and D. Yu, Nano Lett., 2017, 17, 7539–7543.

42 L. Mennel, M. Paur and T. Mueller, APL Photonics, 2019, 4, 034404.

43 A. R. Khan, B. Liu, T. Lu, L. Zhang, A. Sharma, Y. Zhu, W. Ma and Y. Lu, ACS Nano, 2020, 14, 15806–15815.

44 R. Rosati, F. Lengers, C. Carmesin, M. Florian, T. Kuhn, F. Jahnke, M. Lorke and D. E. Reiter, Nano Lett., 2021, 21, 9896–9902.

45 T. P. Darlington, C. Carmesin, M. Florian, E. Yanev, O. Ajayi, J. Ardelean, D. A. Rhodes, A. Ghiotto, A. Krayev, K. Watanabe, T. Taniguchi, J. W. Kysar, A. N. Pasupathy, J. C. Hone, F. Jahnke, N. J. Borys and P. J. Schuck, Nat. Nanotechnol., 2020, 15, 854–860.

46 A. Rodriguez, M. Kalbáč and O. Frank, 2D Mater., 2021, 8,

025028.

47 A. Raja, L. Waldecker, J. Zipfel, Y. Cho, S. Brem, J. D. Ziegler, M. Kulig, T. Taniguchi, K. Watanabe, E. Malic, et al., Nat. Nanotechnol., 2019, 14, 832–837.

48 H. H. Fang, B. Han, C. Robert, M. A. Semina, D. Lagarde, E. Courtade, T. Taniguchi, K. Watanabe, T. Amand, B. Urbaszek, M. M. Glazov and X. Marie, Phys. Rev. Lett., 2019, 123, 067401.

49 P. Back, M. Sidler, O. Cotlet, A. Srivastava, N. Takemura, M. Kroner and A. Imamoğlu, Phys. Rev. Lett., 2017, 118, 237404.

50 D. Van Tuan, B. Scharf, Z. Wang, J. Shan, K. F. Mak, I. Žutić and H. Dery, Phys. Rev. B, 2019, 99, 085301.

51 Y. Zhang, H. Guo, W. Sun, H. Sun, S. Ali, Z. Zhang, R. Saito and T. Yang, J. Raman Spectrosc., 2020, 51, 1353–1361.

52 A. M. Dadgar, D. Scullion, K. Kang, D. Esposito, E. H. Yang, I. P. Herman, M. A. Pimenta, E. J. Santos and A. N. Pasupathy, Chem. Mater., 2018, 30, 5148–5155.

53 A. Mitioglu, J. Buhot, M. V. Ballottin, S. Anghel, K. Sushkevich, L. Kulyuk and P. C. Christianen, Phys. Rev. B, 2018, 98, 235429.

54 P. Soubelet, A. E. Bruchhausen, A. Fainstein, K. Nogajewski and C. Faugeras, Phys. Rev. B, 2016, 93, 155407.

55 Y. Cho and T. C. Berkelbach, Phys. Rev. B, 2018, 97, 041409.

56 J. O. Island, A. Kuc, E. H. Diependaal, R. Bratschitsch, H. S. J. van der Zant, T. Heine and A. Castellanos-Gomez, Nanoscale, 2016, 8, 2589–2593.

57 Z. Khatibi, M. Feierabend, M. Selig, S. Brem, C. Linderälv, P. Erhart and E. Malic, 2D Mater., 2018, 6, 015015.

58 F. Carrascoso, R. Frisenda and A. Castellanos-Gomez, Nano Mater. Sci., 2022, 4(1), 44–51.

59 B. Han, C. Robert, E. Courtade, M. Manca, S. Shree, T. Amand, P. Renucci, T. Taniguchi, K. Watanabe, X. Marie, L. E. Golub, M. M. Glazov and B. Urbaszek, Phys. Rev. X, 2018, 8, 031073.

60 M. Goryca, J. Li, A. V. Stier, T. Taniguchi, K. Watanabe, E. Courtade, S. Shree, C. Robert, B. Urbaszek, X. Marie, et al., Nat. Commun., 2019, 10, 1–12.

61 T. Goldstein, Y.-C. Wu, S.-Y. Chen, T. Taniguchi, K. Watanabe, K. Varga and J. Yan, J. Chem. Phys., 2020, 153, 071101.

62 A. Branny, G. Wang, S. Kumar, C. Robert, B. Lassagne, X. Marie, B. D. Gerardot and B. Urbaszek, Appl. Phys. Lett., 2016, 108, 142101.

63 L. Yu, M. Deng, J. L. Zhang, S. Borghardt, B. Kardynal, J. Vučković and T. F. Heinz, Nano Lett., 2021, 21(6), 2376– 2381.

64 F. Carrascoso, H. Li, R. Frisenda and A. Castellanos-Gomez, Nano Res., 2020, 14, 1698–1703.

65 K. Hao, J. F. Specht, P. Nagler, L. Xu, K. Tran, A. Singh, C. K. Dass, C. Schüller, T. Korn, M. Richter, A. Knorr, X. Li and G. Moody, Nat. Commun., 2017, 8, 1–7.

66 C. E. Stevens, J. Paul, T. Cox, P. K. Sahoo, H. R. Gutiérrez, V. Turkowski, D. Semenov, S. A. McGill, M. D. Kapetanakis, I. E. Perakis, D. J. Hilton and D. Karaiskaj, Nat. Commun., 2018, 9, 1–7.

67 J. Joshi, T. Zhou, S. Krylyuk, A. V. Davydov, I. Žutić and P. M. Vora, ACS Nano, 2020, 14, 8528–8538.

68 D. Edelberg, D. Rhodes, A. Kerelsky, B. Kim, J. Wang, A. Zangiabadi, C. Kim, A. Abhinandan, J. Ardelean, M. Scully, D. Scullion, L. Embon, R. Zu, E. J. G. Santos, L. Balicas, C. Marianetti, K. Barmak, X. Zhu, J. Hone and A. N. Pasupathy, Nano Lett., 2019, 19, 4371–4379.

69 C. Robert, D. Lagarde, F. Cadiz, G. Wang, B. Lassagne, T. Amand, A. Balocchi, P. Renucci, S. Tongay, B. Urbaszek and X. Marie, Phys. Rev. B, 2016, 93, 205423.

70 T. Godde, D. Schmidt, J. Schmutzler, M. Aßmann, J. Debus, F. Withers, E. M. Alexeev, O. D. Pozo-Zamudio, O. V. Skrypka, K. S. Novoselov, M. Bayer and A. I. Tartakovskii, Phys. Rev. B, 2016, 94, 165301.

71 S. Ayari, A. Smiri, A. Hichri, S. Jaziri and T. Amand, Phys. Rev. B, 2018, 98, 205430.

72 G. Moody, K. Tran, X. Lu, T. Autry, J. M. Fraser, R. P. Mirin, L. Yang, X. Li and K. L. Silverman, Phys. Rev. Lett., 2018, 121, 057403.

73 E. Liu, J. V. Baren, Z. Lu, M. M. Altaiary, T. Taniguchi, K. Watanabe, D. Smirnov and C. H. Lui, Phys. Rev. Lett., 2019, 123, 027401.

74 M. D. Tran, J. H. Kim and Y. H. Lee, Curr. Appl. Phys., 2016, 16, 1159–1174.

75 D. Van Tuan, M. Yang and H. Dery, Phys. Rev. B, 2018, 98, 125308.

76 M. Florian, M. Hartmann, A. Steinhoff, J. Klein, A. W. Holleitner, J. J. Finley, T. O. Wehling, M. Kaniber and C. Gies, Nano Lett., 2018, 18, 2725–2732.

77 Y. V. Zhumagulov, A. Vagov, N. Y. Senkevich, D. R. Gulevich and V. Perebeinos, Phys. Rev. B, 2020, 101, 245433.

78 M. Koperski, M. R. Molas, A. Arora, K. Nogajewski, M. Bartos, J. Wyzula, D. Vaclavkova, P. Kossacki and M. Potemski, 2D Mater., 2018, 6, 015001.

79 T. Deilmann, P. Krüger and M. Rohlfing, Phys. Rev. Lett., 2020, 124, 226402.

80 J. Förste, N. V. Tepliakov, S. Y. Kruchinin, J. Lindlau, V. Funk, M. Förg, K. Watanabe, T. Taniguchi, A. S. Baimuratov and A. Högele, Nat. Commun., 2020, 11, 4539.

81 F. Xuan and S. Y. Quek, Phys. Rev. Res., 2020, 2, 033256.

82 C. Robert, H. Dery, L. Ren, D. Van Tuan, E. Courtade, M. Yang, B. Urbaszek, D. Lagarde, K. Watanabe, T. Taniguchi, T. Amand and X. Marie, Phys. Rev. Lett., 2021, 126, 067403.

83 M. Zinkiewicz, T. Woźniak, T. Kazimierczuk, P. Kapuscinski, K. Oreszczuk, M. Grzeszczyk, M. Bartoš, K. Nogajewski, K. Watanabe, T. Taniguchi, C. Faugeras, P. Kossacki, M. Potemski, A. Babiński and M. R. Molas, Nano Lett., 2021, 21, 2519–2525.

84 J. Klein, A. Hötger, M. Florian, A. Steinhoff, A. Delhomme, T. Taniguchi, K. Watanabe, F. Jahnke, A. W. Holleitner, M. Potemski, C. Faugeras, J. J. Finley and A. V. Stier, Phys. Rev. Res., 2021, 3, L022009.

85 M. Grzeszczyk, K. Olkowska-Pucko, K. Nogajewski, K. Watanabe, T. Taniguchi, P. Kossacki, A. Babiński and M. R. Molas, Nanoscale, 2021, 13, 18726–18733.

86 Y. V. Zhumagulov, A. Vagov, D. R. Gulevich and V. Perebeinos, arXiv preprint arXiv:2104.11800, 2021.

87 F. Katsch, D. Christiansen, R. Schmidt, S. M. de Vasconcellos, R. Bratschitsch, A. Knorr and M. Selig, Phys. Rev. B, 2020, 102, 115420.

88 R. Y. Kezerashvili and A. Spiridonova, Phys. Rev. Res., 2021, 3, 033078.

89 F. Xuan and S. Y. Quek, npj Comput. Mater., 2021, 7, 198.

90 Y. V. Zhumagulov, A. Vagov, D. R. Gulevich, P. E. Faria Junior and V. Perebeinos, J. Chem. Phys., 2020, 153, 044132.

91 Y. Zhang, K. Shinokita, K. Watanabe, T. Taniguchi, Y. Miyauchi and K. Matsuda, Adv. Funct. Mater., 2021, 31, 2006064.

92 M. Danovich, V. Zólyomi and V. I. Fal'Ko, Sci. Rep., 2017, 7, 1–5.

93 G. A. Prando, M. E. Severijnen, I. D. Barcelos, U. Zeitler, P. C. M. Christianen, F. Withers and Y. Galvão Gobato, Phys. Rev. Appl., 2021, 16, 064055.

Supporting Information: Revealing the impact of strain in the optical properties of bubbles in monolayer MoSe2

F. S. Covre,[a] P. E. Faria, Junior,[b] V. O. Gordo,[c] C. Serati de Brito,[a] Y. V. Zhumagulov,[b] M. D. Teodoro,[a] O. D. D. Couto, Jr.,[c] L. Misoguti,[d] S. Pratavieira,[d] M. B. Andrade,[d] P. C. M. Christianen,[e] J. Fabian,[b] F. Withers[f] and Y. Galvão Gobato*[a]

[a] Departamento de Física, Universidade Federal de São Carlos, 13565-905 São Carlos, SP, Brazil. E-mail: yara@df.ufscar.br

[b] Institute for Theoretical Physics, University of Regensburg, 93040 Regensburg, Germany

[c] Instituto de Física "Gleb Wataghin", Universidade Estadual de Campinas, 13083-859 Campinas, São Paulo, Brazil

[d] Instituto de Física de São Carlos – Universidade de São Paulo, CEP 13566-590 São Carlos, São Paulo, Brazil

[e] High Field Magnet Laboratory (HFML – EMFL), Radboud University, 6525 ED Nijmegen, The Netherlands

[f] College of Engineering, Mathematics and Physical Sciences, University of Exeter, Exeter EX4 4QF, UK

1. Calculation of the exciton energy

The exciton properties of monolayer transition metal dichalcogenides (TMDCs) are calculated via the effective Bethe-Salpeter equation (BSE)[1–4] considering parabolic bands with the Rytova-Keldish (RK) potential[5–8] mediating the electron-hole electrostatic interaction, which accurately describes 2D monolayers subjected to different dielectric environments[8–18]. The BSE for excitons in k-space reads

$$\left[\left(\frac{\hbar^2}{2m_0}\right)\frac{k^2}{\mu}-\Omega_\lambda\right]F_\lambda(\vec{k})-\sum_{\vec{k}'}\mathrm{V_{RK}}(\vec{k}-\vec{k}')F_\lambda(\vec{k}')=0\,, \tag{1}$$

with Ω_λ and $F_\lambda(\vec{k})$ being the exciton binding energy and wavefunction for the λ-th state, respectively, and the exciton reduced mass is written as $\mu^{-1} = m_c^{-1} + m_v^{-1}$, with $m_{c(v)}$ being the effective mass of the conduction (valence) band.

The RK potential reads

$$\mathrm{V_{RK}}(\vec{K})=\frac{1}{\Lambda}\frac{e^2}{2\varepsilon_0}\frac{1}{\varepsilon K+r_0K^2} \tag{2}$$

with r_0 being the screening length of the TMDC and ε being the effective dielectric constant due to the surroundings, given by $\varepsilon = (\varepsilon_t + \varepsilon_b)/2$, with $\varepsilon_{t(b)}$ indicating the dielectric constant of the top (bottom) region adjacent to the TMDC.

We take into account the renormalization of the screening length due to the dielectric surroundings via

$$r_0(\varepsilon_t, \varepsilon_b) = \frac{d\varepsilon_m}{2}\left(1 - \frac{\varepsilon_t^2 + \varepsilon_b^2}{2\varepsilon_m^2}\right) \tag{3}$$

in which d is the effective thickness of the TMDC and εm is the dielectric constant of the TMDC monolayer[8,19].

The band gap renormalization of the monolayer TMDC due to the dielectric screening[9,12] can be incorporated as

$$E_g(\varepsilon_t, \varepsilon_b) = E_0 + \Sigma(\varepsilon_t, \varepsilon_b), \tag{4}$$

With

$$\Sigma(\varepsilon_t, \varepsilon_b) = \frac{e^2}{4\pi\varepsilon_0}\frac{1}{\varepsilon_m d}\left[\frac{L_t + L_b}{\sqrt{L_t L_b}}\tanh^{-1}\left(\sqrt{L_t L_b}\right) - \ln(1 - L_t L_b)\right], \tag{5}$$

in which $L_i=(\varepsilon_m-\varepsilon_i) / (\varepsilon_m+\varepsilon_i)$, i = t,b. Note that $E_g(1,1) = E_0 +\Sigma(1,1)$ is the band gap of the bare monolayer TMDC.

The final exciton energy, associated to the absorption or photoluminescence peak, is then given by

$$E_X = E_g(\varepsilon_t, \varepsilon_b) - \Omega_X(\varepsilon_t, \varepsilon_b), \tag{6}$$

in which X refers to the excitonic state we are interested in. Particularly to our analysis to calibrate the parameters for $MoSe_2$, we are interested in the 1s and 2s states of the A exciton.

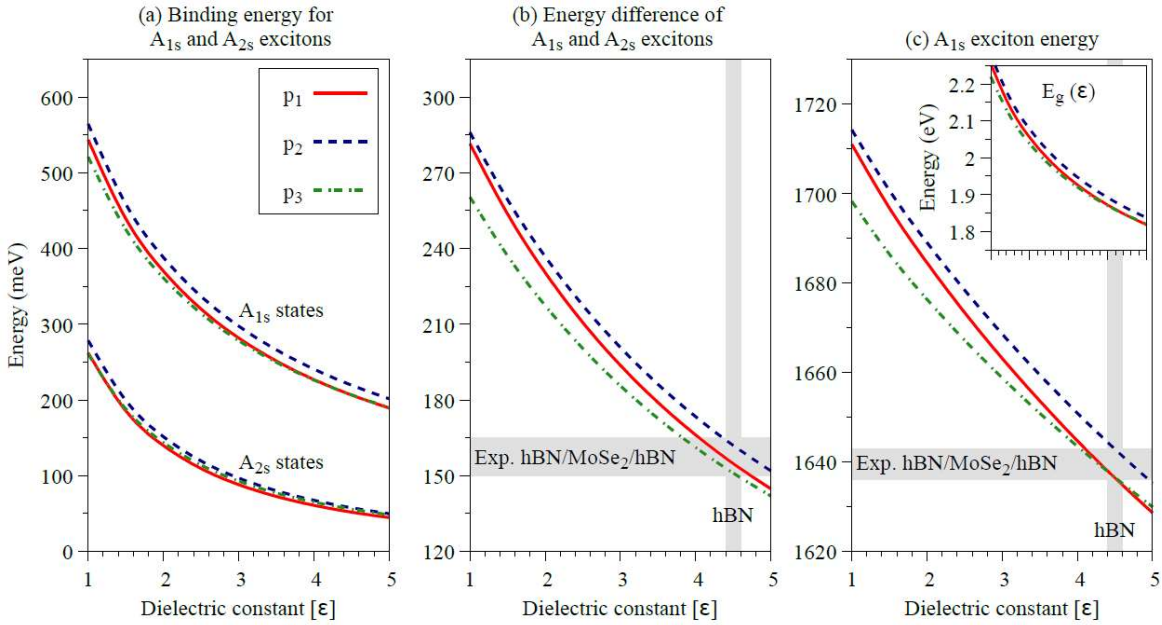

***Figure S1**: (a) Binding energies of 1s and 2s A excitons states, (b) energy difference between 1s and 2s A excitons binding energies and (c) the total 1s A exciton energy as function of the dielectric constant $\varepsilon = (\varepsilon_t + \varepsilon_b)/2$. The inset in panel (c) shows the band gap dependence with respect to ε, given by Eq. (4). The shaded regions in panels (b) and (c) represent the experimental data collected in Table S1. The parameter sets p1-p3 are given in Table S2.*

The exciton energy EX depends on the intrinsic parameters of the TMDC monolayer, namely, μ, r0, d and E0. To obtain a reliable parameters' set that captures the experimental values and allows us to understand the changes in the dielectric environment of the MoSe2 bubble, we average different parameters available in the literature, summarized in Table S1. The energy variation of ~ 10 meV among the different experiments is consistent with typical dielectric disorder present in monolayer TMDCs[12]. Furthermore, it is also worth mentioning that the reduced exciton mass is not influenced by the dielectric environment[20]. The experimental values of r0 given in Table S1 are a bit smaller than what is predicted by theory, for instance, Ref.8 reports r0 = 5.2 nm and d =6.0 Å, and Ref.21 provides r0 =5.6 nm and d =6.5 Å. Taking into account the fluctuations in the experimental and theoretical values, we suggest three different parameter sets that best reproduce

***Table S1**: Parameters extracted from experimental studies on hBN/MoSe2/hBN samples.*

	μ	ε	r_0 (nm)	E_A (meV)	Δ_{21} (meV)	T (K)
Han et al.[15]	0.28	4.5	4.5	1636.0	150.0	4
Goryca *et al.*[16]	0.35	4.4	3.9	1643.0	165.0	4
Goldstein *et al.*[17]	0.35	4.5	4.5	1643.6	152.4	4

***Table S2**: Calibrated parameter sets used in the exciton calculations. The value of E0 = 1615 meV is kept the same in all cases.*

	μ	r_0 (nm)	d (Å)
p_1	0.30	4.5	6.5
p_2	0.35	4.5	6.0
p_3	0.35	5.0	6.5

the high-quality experiments in hBN encapsulated MoSe2. These values are given in Table S2 and the calculated results are summarized in Fig. S1. By performing the calculations with these 3 parameter sets we are able to nicely capture the dielectric dependence in an energy window of ~ 10 of meV, as expected in real samples due to the dielectric disorder of the surroundings12, and thus reproducing the experimental values given in Table S1. Furthermore, in Fig. 1 of the main text we show that these parameter sets nicely describe the A exciton peaks obtained via photoluminescence at the PMMA/MoSe2/hBN region at nominally zero strain and allows us to understand the variation of strain and dielectric surroundings in different regions of the sample.

2. First principles calculations

We performed the first principles calculations of the orbital angular momentum using the density functional theory (DFT) implemented in the WIEN2k package22. We used the Perdew-Burke-Ernzerhof (PBE) exchange-correlation functional23, a Monkhorst-Pack k-grid of 15×15 and selfconsistent convergence criteria of 10-6 e for the charge and 10-6 Ry for the energy. We considered a core–valence separation energy of -6 Ry, atomic spheres with orbital quantum numbers up to 10 and the plane-wave cutoff multiplied by the smallest atomic radii is set to 9. For the spin-orbit coupling effects, the core electrons are treated fully relativistically whereas valence electrons are treated via a second variational procedure24, with the scalar-relativistic wave functions calculated in an energy window of -10 to 10 Ry. The chosen energy window thus provides more than a 1000 bands, which are crucial for a proper convergence of the angular momentum implementation, as shown in Ref.25. The angular momenta of the conduction and valence band states that give rise to the A exciton are calculated with the the state-of-the-art approach given in Refs.25–28. The resulting g-factor of the Zeeman shift at the K-valley for the relevant conduction and valence bands is then written as gc(v) = Lc(v) +1, with the value of 1 referring to the spin-up character of the bands involved (spin-conserving optical transition). The A exciton g-factor is then given by gA =

2(gc−gv) with the prefactor 2 taking into account the time-reversal relation between K and -K valleys. We considered the unstrained MoSe2 monolayer with lattice parameters of a0 =3.289 Å and d0 = 3.335 Å[29] and the biaxial strain is applied by compressing or stretching the lattice parameter, accompanied with the change in the thickness as given by from Ref4. For all cases we considered a vacuum spacing of 16 Å to avoid self-interaction.

3. Experiments

Figure S2 shows the color-code mapping of the PL intensity as a function of the position at 300K for the same positions indicated in Figure 1. We observed that there is a clear red shift in the bubble region which depends on the laser position. Similar behaviour was observed in Figure 1 at 4K. Fig. S2-(b) illustrates typical PL spectrum in the flat region and in the bubble region .

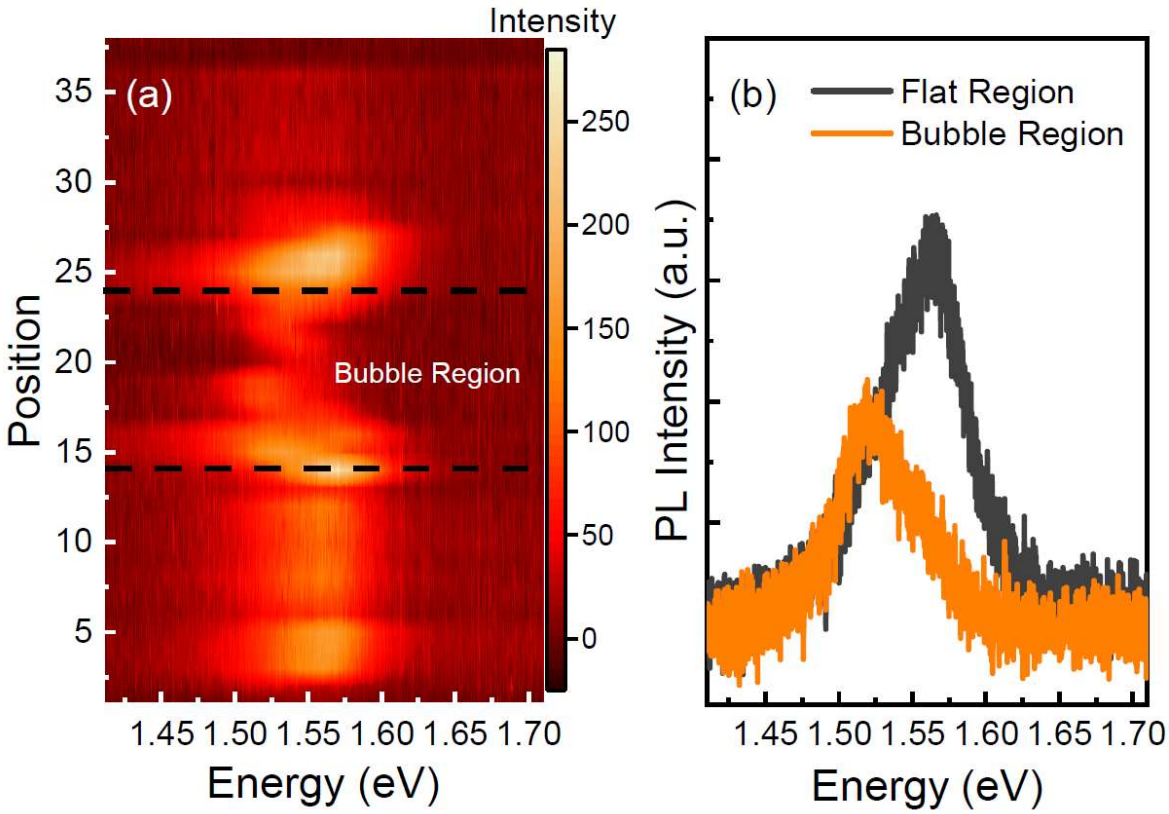

Figure S2: *(a) Color-code mapping of the PL Intensity as a function of the position at 300K (b) Typical PL spectrum in the flat and bubble region also at 300K.*

Figure S3 shows the E′ Raman mode for different laser positions on the sample measured with 633nm laser excitation at 300K. Figure S3-(b) shows the optical image of the

sample and the laser positions of Raman measurements. We observe a clear blue shift on the edge of the bubble which indicates a compressive strain. On the other hand, a red shift of E´ is observed in the bubble region. In addition, we remark that this red shift depends on the laser position in the bubble region. Similar behavior was observed for other Raman modes.

Figure S4-(a) shows typical PL spectra in the bubble region for 633nm laser excitation and 20 μW at 4K. Figure S4(b) shows the laser power dependence for L2 PL peak in low and high laser power regimes. In general, we have observed a non-linear laser power dependence probably due to a saturation of available trap sites in the ML $MoSe_2$. We have fitted the curves in different laser power regimes using the power law. It is well known that for a free exciton emission it is expected to observe a linear dependence with k=1. However, we have obtained lower values for k for both laser power regimes which indicates that the emission L2 is related to localized trap states in the bubble region.

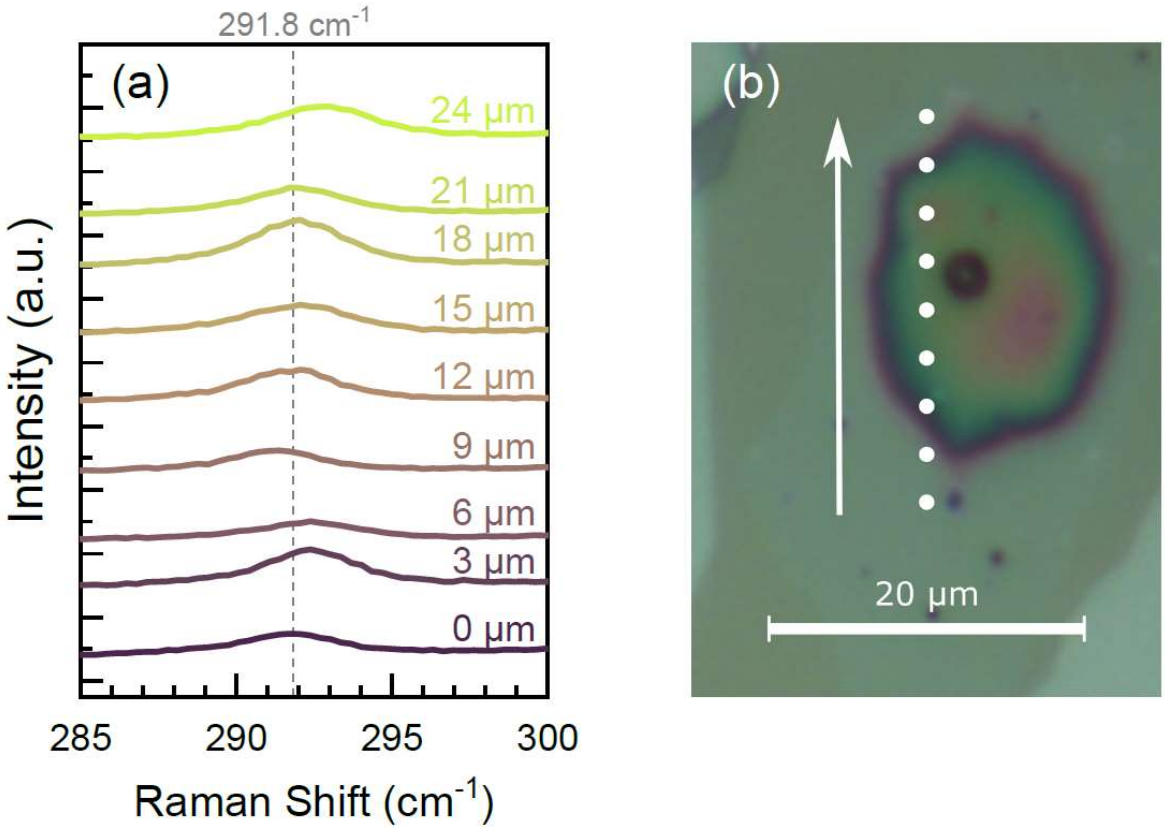

Figure S3: *(a) Typical Raman spectra in the region of the E' mode as a function of laser position measured with 633nm laser excitation at 300K (b) Optical image of the bubble and laser position of Raman measurements*

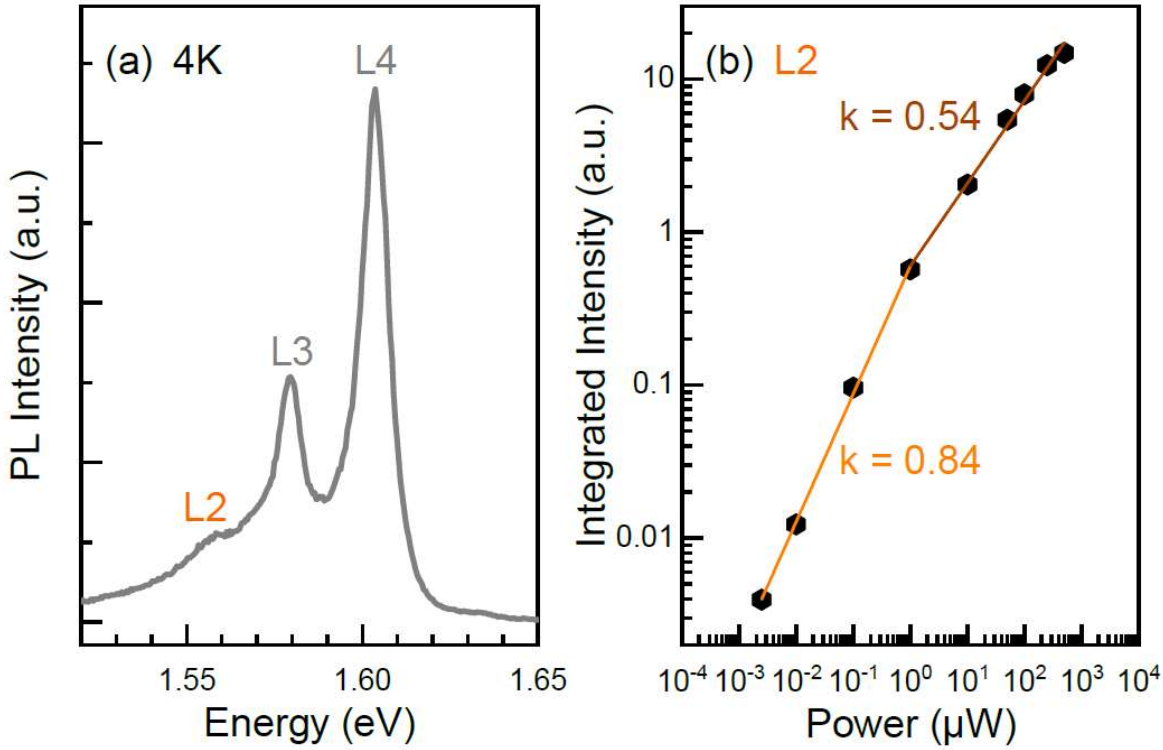

Figure S4: *(a) PL spectrum in the bubble region and (b) Laser power dependence of L2 at 4K*

Figure S5 shows the PL intensity as a function of time for the X and T emissions in the flat region and for the L3 and L4 emissions in the bubble region at 4K. We have observed two decay components, the first being limited by our temporal resolution of our experimental setup. The PL decay times are shown in Figure S5. In general, We have observed that X, T, L3 and L4 have similar PL decay times. We remark that the main component of the L4 and L3 emission has a very short lifetime. This result is consistent with the identification of L4 and L3 as exciton and trion respectively.

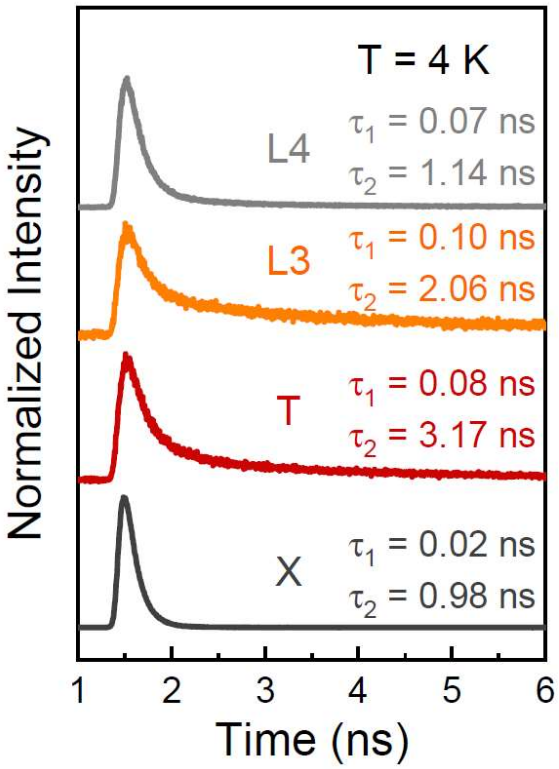

***Figure S5**: Time-resolved PL of X and T in the flat region and L3 and L4 in the bubble region at 4K. Two decay components are observed, the first being limited by the temporal resolution of our experimental system.*

Figure S6-(a) shown the color code map of polarized the PL intensity as a function of magnetic field for a different position in the bubble region labelled A5. We have observed a complex behaviour for the PL peak energies as a function of magnetic field. Figure S6-(b) shows a typical polarization resolved PL at 0T and 6T. Figure S6-(c) shows the exciton splitting as function of magnetic field and the extracted exciton g-factor.

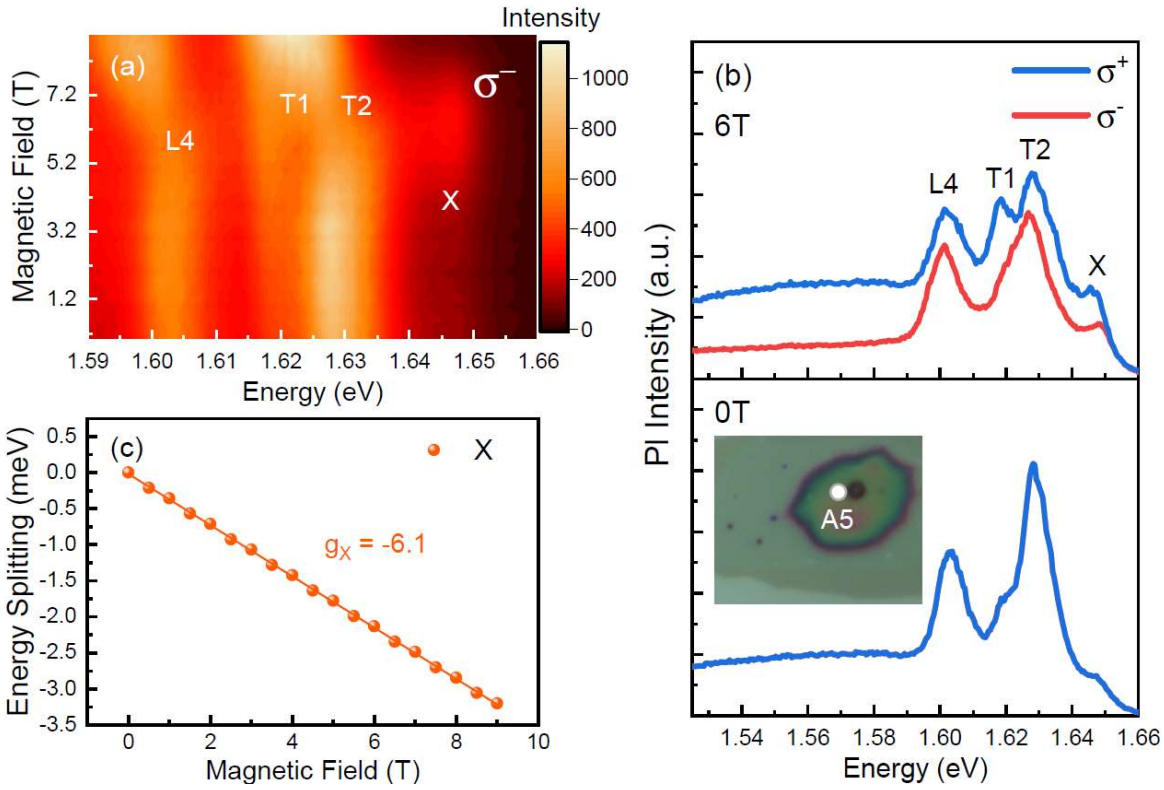

Figure S6: *(a)Color code mapping of the μ-PL intensity versus magnetic field in the bubble region (position A5) under linearly polarized excitation.(b) Typical polarization resolved PL at 0T and 6T (c) Exciton energy splitting versus magnetic field at 4K*

References

[1] M. Rohlfing and S. G. Louie, Phys. Rev. Lett., 1998, 81, 2312–2315.

[2] M. Rohlfing and S. G. Louie, Phys. Rev. B, 2000, 62, 4927.

[3] P. E. Faria Junior, M. Kurpas, M. Gmitra and J. Fabian, Phys. Rev. B, 2019, 100, 115203.

[4] K. Zollner, P. E. Faria Junior and J. Fabian, Phys. Rev. B, 2019, 100, 195126.

[5] N. S. Rytova, Mosc. Univ. Phys. Bull., 1967, 3, 18.

[6] L. Keldysh, Sov. J. Exp. Theo. Phys. Lett., 1979, 29, 658.

[7] P. Cudazzo, I. V. Tokatly and A. Rubio, Phys. Rev. B, 2011, 84, 085406.

[8] T. C. Berkelbach, M. S. Hybertsen and D. R. Reichman, Phys. Rev. B, 2013, 88, 045318.

[9] Y. Cho and T. C. Berkelbach, Phys. Rev. B, 2018, 97, 041409.

[10] A. Chernikov, T. C. Berkelbach, H. M. Hill, A. Rigosi, Y. Li, O. B. Aslan, D. R. Reichman, M. S. Hybertsen and T. F. Heinz, Phys. Rev. Lett., 2014, 113, 076802.

[11] A. Raja, A. Chaves, J. Yu, G. Arefe, H. M. Hill, A. F. Rigosi, T. C. Berkelbach, P. Nagler, C. Schüller, T. Korn et al., Nature communications, 2017, 8, 1–7.

[12] A. Raja, L.Waldecker, J. Zipfel, Y. Cho, S. Brem, J. D. Ziegler, M. Kulig, T. Taniguchi, K.Watanabe, E. Malic et al., Nature nanotechnology, 2019, 14, 832–837.

[13] A. V. Stier, K. M. McCreary, B. T. Jonker, J. Kono and S. A. Crooker, Nature communications, 2016, 7, 1–8.

[14] A. V. Stier, N. P. Wilson, K. A. Velizhanin, J. Kono, X. Xu and S. A. Crooker, Phys. Rev. Lett., 2018, 120, 057405.

[15] B. Han, C. Robert, E. Courtade, M. Manca, S. Shree, T. Amand, P. Renucci, T. Taniguchi, K. Watanabe, X. Marie, L. E. Golub, M. M. Glazov and B. Urbaszek, Phys. Rev. X, 2018, 8, 031073.

[16] M. Goryca, J. Li, A. V. Stier, T. Taniguchi, K. Watanabe, E. Courtade, S. Shree, C. Robert, B. Urbaszek, X. Marie et al., Nature communications, 2019, 10, 1–12.

[17] T. Goldstein, Y.-C.Wu, S.-Y. Chen, T. Taniguchi, K.Watanabe, K. Varga and J. Yan, The Journal of Chemical Physics, 2020, 153, 071101.

[18] K.-Q. Lin, C. Shen Ong, S. Bange, P. E. Faria Junior, B. Peng, J. D. Ziegler, J. Zipfel, C. Bäuml, N. Paradiso, K. Watanabe et al., arXiv, 2020, arXiv–2006.

[19] B. Scharf, D. Van Tuan, I. Žuti´c and H. Dery, Journal of Physics: Condensed Matter, 2019, 31, 203001.

[20] L.Waldecker, A. Raja, M. Rösner, C. Steinke, A. Bostwick, R. J. Koch, C. Jozwiak, T. Taniguchi, K.Watanabe, E. Rotenberg, T. O.Wehling and T. F. Heinz, Phys. Rev. Lett., 2019, 123, 206403.

[21] A. Laturia, M. L. Van de Put and W. G. Vandenberghe, npj 2D Materials and Applications, 2018, 2, 1–7.

[22] P. Blaha, K. Schwarz, F. Tran, R. Laskowski, G. K. Madsen and L. D. Marks, The Journal of chemical physics, 2020, 152, 074101.

[23] J. P. Perdew, K. Burke and M. Ernzerhof, Phys. Rev. Lett., 1996, 77, 3865–3868.

[24] D. J. Singh and L. Nordstrom, Planewaves, Pseudopotentials, and the LAPW method, Springer Science & Business Media, 2006.

[25] T. Wo´zniak, P. E. Faria Junior, G. Seifert, A. Chaves and J. Kunstmann, Phys. Rev. B, 2020, 101, 235408.

[26] T. Deilmann, P. Krüger and M. Rohlfing, Phys. Rev. Lett., 2020, 124, 226402.

[27] J. Förste, N. V. Tepliakov, S. Y. Kruchinin, J. Lindlau, V. Funk, M. Förg, K. Watanabe, T. Taniguchi, A. S. Baimuratov and A. Högele, Nature Communications, 2020, 11, 4539.

[28] F. Xuan and S. Y. Quek, Phys. Rev. Research, 2020, 2, 033256.

[29] A. Kormányos, G. Burkard, M. Gmitra, J. Fabian, V. Zólyomi, N. D. Drummond and V. Fal'ko, 2D Materials, 2015, 2, 022001.

CONCLUSÃO

Em conclusão, apresentamos ao longo dessa tese resultados de estudos de propriedades óticas sistemáticos realizados em diferentes amostras de materiais TMDs, mais especificamente, amostras de monocamada de WS_2 crescidas por epitaxia de van der Waals, e monocamadas de $MoSe_2$ obtidas por esfoliação mecânica e transferidas sob um substrato de h-BN.

Nosso estudo sobre monocamada de WS_2 mostrou um efeito importante de fotodopagem por irradiação por laser nos picos de emissão excitônicos. A fotodopagem resultou em um aumento intensidade das emissões de picos de menor energia no espectro de fotoluminescência do material. Mostramos também, que sob certas condições de irradiação por laser, o processo de foto-dopagem é irreversível em baixa temperatura, apresentando um deslocamento para o vermelho no espetro de fotoluminescência. No entanto, o processo é reversível com o aquecimento da amostra. Esses resultados ajudam a obter uma maior compreensão das propriedades óticas de monocamadas de WS_2, bem como nos processos de foto-dopagem, o que é de grande interesse para futuros dispositivos baseados em dissulfeto de tungstênio. Além disso, os estudos realizados reforçam a necessidade de proteção da superfície e interface TMD/SiO_2 usando materiais isolantes como h-BN para evitar efeitos de foto-dopagem nesses sistemas.

Com relação ao estudo sobre monocamadas de disseleneto de molibdênio, investigamos os efeitos de tensão mecânica biaxial sob as propriedades óticas desse material. Observamos que a tensão modificar a energia de ligação dos complexos excitônicos e altera os valores do fator-g de éxcitons e tríons. O comportamento do fator-g observado em nossos experimentos pode ser explicado de maneira qualitativa através de cálculos por primeiros princípios, porém nossos resultados mostram que apenas considerar efeitos de tensão não é suficiente para explicar todos os efeitos observados, indicando assim que a estrutura fina tanto do tríon quanto do éxciton seria importante para explicar esses efeitos, podendo ser afetada por tensão, dopagem e confinamento dielétrico. Em resumo, nossos resultados evidenciam que a tensão mecânica biaxial pode ser usada para modificar tanto as energias quanto o fator-g de complexos excitônicos em monocamadas de TMDs.

Acreditamos que os resultados apresentados nessa tese contribuem para um maior entendimento sobre as propriedades óticas de dicalcogenetos de metais de transição, bem

como sugerem futuros caminhos de investigação desses materiais, como por exemplo a realização de estudo controlando-se a tensão aplicada em uma monocamada, podendo assim investigar os efeitos de tensão em TMDs de maneira mais controlada. Os estudos também motivam estudos similares em outros sistemas baseados em monocamadas de TMD e o desenvolvimento de modelos mais completos para explicar os resultados experimentais nesses sistemas.